Material Screening and Selection for the XENON100 Dark Matter Experiment

Dissertation

zur
Erlangung der naturwissenschaftlichen Doktorwürde
(Dr. sc. nat.)

vorgelegt der
Mathematisch-naturwissenschaftlichen Fakultät
der
Universität Zürich

von
Ali Askin
aus der
Türkei

Promotionskomitee
Prof. Dr. Laura Baudis (Vorsitz)
Dr. Marc Schumann
Dr. Alfredo Ferella

Zürich 2012

Abstract

Since cosmological observations revealed that the non-baryonic content of the universe is beyond its baryonic content, a world-wide increasing experimental effort was pioneered for the experimental detection of this unknown mysterious matter. The goal of XENON is to directly detect dark matter in the form of Weakly Interacting Massive Particles (WIMPs) via their elastic scattering off Xe nuclei. Dark matter searches, like XENON, are rare event searches and need massive detectors with low energy thresholds and background in a extraordinarily low level in order to allow rare nuclear recoils to be observed.
A detector can be isolated against cosmic and environmental radiation by placing it in an underground laboratory and in a passive shield. Materials used in the detector and shield construction are in close vicinity of the detector medium. Thus special attention has to be paid for the selection of materials with low intrinsic radioactive contaminations. Otherwise there will not be so much gain by going to deep underground sides and by placing the detector in a passive shield.
The XENON experiment is located at the Laboratori Nazionalli del Gran Sasso (LNGS) in Italy. In the second phase of the XENON experiment (XENON100), the aim was to increase the detector sensitivity for the WIMP-nucleon interactions by increasing the detector mass and at the same time decrease the background emitted from the detector and the shield materials. Since γ-ray spectroscopy is the most effective method to screen the materials and select the radio pure ones for the detector construction, a 2.2 kg p-type high purity germanium (HPGe) detector, named Gator, in its ultra low background shield was installed at LNGS in 2007. The shield of Gator consists of 5 cm thick ultra-low background copper surrounded by 20 cm thick lead layer. Monte Carlo simulations are essential to obtain the activities of the screened samples and to study the background of Gator facility. Hence, entire detector and shield geometry were coded into Geant4 and decays of the various known radionuclides are simulated within screened samples for the activity determination. In addition to the standard data analysis method, an alternative method was developed and used to cross-check the results obtained from the standard one. Gator facility was operated to screen all the candidate materials for XENON100 and select the radio pure ones. The results obtained in the screening measurements are used to predict the electromagnetic background of the XENON100 detector.
This thesis focuses on the details of the Gator facility, Monte Carlo simulations of the facility along with the analysis methods used determine the activities of the samples screened with Gator. The details of Gator's background study and the results obtained from the screening measurements are given.

Zusammenfassung

Kosmologische Beobachtungen der letzten zehn Jahre haben gezeigt, dass der nicht-baryonische Inhalt des Universums grösser als seine baryonischen Bestandteile ist. Dies löste weltweit erhöhte experimentelle Bemühungen aus, um diese unbekannte, mysteriöse Materie experimentell nachzuweisen. Das Ziel des XENON Experiments ist der direkte Nachweis der Dunklen Materie in Form von schwach wechselwirkenden massiven Teilchen (Weakly Interacting Massive Particles, WIMPs) über ihre elastische Streuung an Xe Kernen. Experimente, die nach Dunkler Materie suchen, brauchen massive Detektoren mit niedriger Energie-Schwelle und einen radioaktiven Untergrund auf einem ausserordentlich niedrigen Niveau, damit das Spektrum der seltenen Kernrückstösse beobachtet werden kann.
Ein Detektor kann gegen kosmische Strahlung und Umgebungsstrahlung isoliert werden, indem er in einem Untergrundlabor und in einer passive Abschirmung installiert wird. Materialen, die im Detektor- und im Abschirmungs-Aufbau verwendet werden, sind in der Nähe des Detektors Mediums. Deswegen ist eine umsichtige Auswahl von Materialien mit niedriger Eigen-Radioaktivität sehr wichtig. Ansonsten ist es nicht ausreichend, den Detektor in einem Untergrundlabor und in einer passive Abschirmung zu platzieren.
Das XENON Experiment ist am Laboratori Nazionali del Gran Sasso (LNGS) in Italien aufgebaut. Das Ziel der zweiten Phase des XENON Projekts (XENON100) ist die Empfindlichkeit des Detektors für WIMP-Nukleon-Wechselwirkungen durch eine Erhöhung der Detektormasse, bei gleichzeitiger Reduzierung des Untergrunds von Detektor- und dem Abschirmungs-Materialien, zu erhöhen. Gamma-Spektroskopie ist die effektivste Methode, um Materialien zu untersuchen (Screening) und für die Detektor-Konstruktion auszuwählen. Aus diesem Grund wurde am LNGS im Jahr 2007 ein hochreiner Germanium Detektor (HPGe) namens Gator in einer effizienten Abschirmung aufgebaut. Gator wurde verwendet, um Materialien für XENON100 zu untersuchen und auszuwählen. Die Ergebnisse in dieser Messungen wurden auch verwendet, um den elektromagnetischen Untergrund des XENON100 Detektors vorhersagen.
Diese Arbeit konzentriert sich auf die Details der Gator-Anlage, Geant4 Simulationen des Detektors, und die Analyse-Methoden, die für die Aktivitätsbestimmung der Materialproben verwendet werden. Zudem werden Details zu Gators Untergrund und die Ergebnisse aus dem Screening-Messungen vorgestellt.

Acknowledgements

While writing this work I was yearning to write this page and now that it is done. I realize that few more lines are needed to express my gratitude to those helped me to reach this end.
I think my first gratitude should go to Prof. Dr. Laura Baudis for giving me the opportunity to put myself to the test performing this work within the XENON group beginning at the RWTH Aachen and then continuing at the Physics Institute University of Zürich. Her constant and patient supervision and support guided me through these years and made this work feasible.
Actually there are too many names and too high risk to forget some. First of all, I would like to thank my friends and colleagues Dr. Marc Schumann, Dr. Aaron Manalaysay, Dr. Teresa Marrodan and Dr. Alfredo Ferella for their patience for correcting my thesis and always showing me the way how a scientific work should be done and presented. Alfredo! you are for me always like a brother and the time that we spent in italy during the installation of Gator was great. I would say that it was one of my best summer ever. It was very hot outside but being in the cold underground was a very nice feeling. The only thing that made me sad is that i did not have muscles, as i expected, after working almost five tonnes of lead and copper :)
It was a great pleasure working in Zürich group. I thank Dr. Alexander Kish Dr. Roberto Santorelli, Dr. Eirini Tziaferi and Annika Behrens for the nice times in Italy and in Switzerland. Watching together European Football Championship in 2008 was very funny, especially because of Roberto. I express my gratitude to the other members of the group: Dr. Tobias Bruch, Sebastian Arrenberg, Michal Tarka and Francis Froborg.
Great thanks to all people from the Physics Institut workshop that had a patience for all ideas. Special thank to Mr. Kurt Bösiger.

Contents

1 Introduction **1**

1.1 Cosmological Motivation for Dark Matter 1

1.2 Direct Detection of Dark Matter 3

1.3 Experimental Requirements 5

1.3.1 Low Background Techniques 5

1.4 Liquid Xenon Detectors for Dark Matter Search 8

1.4.1 XENON100 8

1.4.2 XENON1T 12

1.4.3 DARWIN 13

2 The Gator Facility **15**

2.1 High Purity Germanium Detectors 15

2.1.1 Signal Development 18

2.2 The Gator Facility 20

2.3 Shield Structure 22

2.4 Sample Handling and Cleaning Procedures 24

2.5 The Gator Slow Control 25

3 Simulation and Calibration of Gator **31**

3.1 Geant4 Model of the Detector and the Shield 31

3.2 Energy Calibration and Linearity 33

3.3 Energy Resolution 35

3.4 Efficiency Determination with Certified Sources 36

3.4.1 Energy Threshold 39

4 Data Analysis Methods **41**
4.1 Analysis of the Most Prominent Gamma-Lines 41
4.2 Fit of the data to a simulated spectrum 43

5 The Gator Background **49**
5.1 Background sources 49
5.1.1 Primordial background sources 50
5.1.2 Cosmogenic contribution to background 50
5.2 Background analysis 55
5.2.1 Background at LNGS 55
5.2.2 Comparison of Gator background in Soudan and to GeMPI 63

6 Screening Results **67**
6.1 Photomultipliers 67
6.1.1 Photomultiplier Hamamatsu R8520 67
6.1.2 R11410-MOD 70
6.1.3 QUPIDs 71
6.2 R8520-06-AL PMT Parts 74
6.3 Metal Samples 80
6.3.1 Stainless Steel 81
6.3.2 Screws 82
6.3.3 Copper 83
6.3.4 Titanium 84
6.4 Plastic Samples 85
6.4.1 Polyethylene from the shield of XENON100 85
6.4.2 PTFE sample 86
6.5 Environmental Samples 87

7 Summary and Outlook **91**

Bibliography **93**

List of Figures

1.1 Normalized recoil spectra for WIMP elastic scattering for different WIMP masses 4
1.2 Reached exclusion limit and expected sensitivity for the last XENON100 run to the spin-independent elastic WIMP-nucleon cross-section as function of WIMP mass 8
1.3 XENON100 detector drawing and a picture of the detector 9
1.4 Illustration of working principle of a 2-phase TPC 10
1.5 A typical single nulear recoil a typical single scatter of γ in xenon 11
1.6 Observed event distribution of XENON100 11
1.7 Schematic of XENON1T detector design 12
1.8 The DARWIN sensitivity to the spin-independent WIMP-nucleon cross section 13

2.1 Sketch of a semiconductor detector 17
2.2 Cross-sectional view of large volume coaxial detectors 18
2.3 Schematic of indirect band structure in germanium 19
2.4 Picture of the Gator detector and its shield 21
2.5 Cross-section of Gator detector and its cryostat 21
2.6 Samples in the sample cavity of Gator 23
2.7 Schematic view of the Gator facility at LNGS 23
2.8 Ge-γ spectra of ^{222}Rn progenies on a plastic foil at different time intervals after plate-out 24
2.9 Block diagram of the Gator data acquisition and slow control system . . 26
2.10 Stability plot of the detector high voltage 27
2.11 Plot of the liquid nitrogen level in the cryostat dewar 27
2.12 Plot of the detector's trigger rate 28

2.13 Plot of the nitrogen gas flowing into shield 29
2.14 Stability plot of the leakage current of the germanium diode 29

3.1 Geant4 model of the detector and the shield geometry 32
3.2 Monte Carlo geometry of Gator out of its shield 32
3.3 Comparison of the calibration spectra acquired with ^{60}Co and ^{228}Th calibration sources with the one from a Monte Carlo simulation 34
3.4 Linearity of Gator at different energies 35
3.5 Energy resolution of Gator 36
3.6 Best fit of the simulations to the CANMET-STSD2 data 37
3.7 Best fit of the simulations to the IAEA-Soil6 data 38
3.8 Energy threshold of Gator in 2007, 2008 and 2010 40

4.1 Illustration of a double sided confidence interval for 95% confidence level 44
4.2 Illustration of a single sided confidence interval for 95% confidence level . 45
4.3 Best-fit of Monte Carlo generated spectra to Gator data from a stainless steel sample 46

5.1 Decay chain of ^{238}U 51
5.2 Decay chain of ^{232}Th 52
5.3 Decay scheme of ^{40}K 53
5.4 Decay scheme of ^{65}Zn and ^{58}Co 54
5.5 Decay scheme of ^{60}Co and ^{54}Mn 54
5.6 Acquired background spectrum in September 2007 55
5.7 Fit of simulations to the background in 2007 57
5.8 The individual, best-fit contributions to the observed spectrum in 2007 . 57
5.9 Comparison ofthe background spectra from 2007 and 2008 58
5.10 Fit of simulations to the background data in 2008 60
5.11 The individual, best-fit contributions to the observed spectrum in 2008 . 60
5.12 Comparison of the background spectra from 2007, 2008 and 2010 61
5.13 Fit of the simulations to the background data in 2010 63
5.14 The individual, best-fit contributions to the observed spectrum in 2010 . 63
5.15 Background spectra of Gator at Soudan, at LNGS and the spectrum of the GeMPI detector 64

6.1 Picture of the Hamamatsu R8520 PMT 68
6.2 Fit of the simulations to the R8520 data 69
6.3 Picture of the Hamamatsu R11410 PMT 70
6.4 Fit of the simulations to the R11410-MOD data 71
6.5 Picture of a QUPID 72
6.6 Fit of the simulations to the QUPIDs data 73
6.7 Fit of the simulations to the data from the quartz screening 73
6.8 schematic structure of the R8520-06-AL PMTs 75
6.9 Fit spectra obtained for the sample A to sample F 77
6.10 Fit spectra obtained for the sample H to sample M 78
6.11 Contribution of each PMT part to the overall ^{238}U , ^{232}Th ,^{40}K and ^{60}Co activity 80
6.12 Fit of the simulations to the data from the stainless steel screening . . . 81
6.13 Fit of the simulations to the screw data 82
6.14 Fit of the simulations to the copper data 83
6.15 Fit of the simulations to the titanium data 84
6.16 Fit of the simulations to the polyethylene data 86
6.17 Fit of the simulations to PTFE data 87
6.18 Fit of the simulations to the concrete data from the wall 88
6.19 Fit of the simulations to the concrete data from the floor 88

7.1 Energy spectra of the background from measured data and Monte Carlo simulations in the 30 kg fiducial volume 92

List of Tables

3.1 Mass model of Gator from the Monte Carlo simulations 33

3.2 Activity results obtained for the CANMET-STSD2 certified source 38

3.3 Results obtained for the IAEA-Soil6 certified source 39

3.4 Activity results obtained by using the analysis of the most prominent lines method from screening the CANMET-STSD2 and IAEA Soil6 . . . 39

4.1 Examples of upper limit or specific activities calculation 42

5.1 Properties of the cosmogenic radioisotopes 53

5.2 Background counting rates (in events/day) in 2007) 56

5.3 Activities of the radionuclides calculated for the background run taken in 2007 56

5.4 Background counting rates (in events/day in 2008) 59

5.5 Activities of the radionuclides calculated for the background run taken in 2008 59

5.6 Background counting rates (in events/day) in 2010 62

5.7 Activities of the radionuclides calculated for the background run taken in 2010 62

5.9 Integral background counting rates for Gator as measured at Soudan and at LNGS in three different runs 65

5.10 Comparison of the background counting rates of Gator taken at LNGS to the background counting rates of Gator in Soudan and to the GeMPI detector. 66

6.1 Activity values calculated for different PMT batches 69

6.2 Activities obtained for the R11410-MOD 70

6.3 Comparison of Gator screening results for Hamamatsu R11410-MOD to R8520 . . . 71
6.4 Activities obtained for the QUPID sample . . . 72
6.6 Activities obtained for quartz sample . . . 73
6.7 Comparison of Gator screening results for QUPID, Hamamatsu R11410-MOD and R8520 . . . 74
6.8 List of the screened PMT parts . . . 75
6.10 Mass model for R8520-06-AL from Hamamatsu . . . 76
6.11 Activities calculated for the single R8520 PMT parts . . . 79
6.12 Comparison of the expected activity to the measured one for R8520 PMT 79
6.14 Activity results for stainless steel . . . 81
6.16 Activity results for screws . . . 82
6.18 Activity results for copper . . . 83
6.20 Results from tianium screening . . . 85
6.21 Results from the polyethylene screening . . . 86
6.22 Results from the PTFE screening . . . 87
6.23 Results from the concrete screening . . . 89

Chapter 1

Introduction

The existence of dark matter which does not absorb or emit electromagnetic radiation was first suggested by Zwicky in 1933 [1] based on the estimates of the total mass of galaxy clusters via their velocity dispersions. Nowadays, there are convincing indirect evidences for the existence of dark matter and a world-wide increasing effort is ongoing for the experimental detection of this mysterious matter. Only about 4% of the total universe density consists of baryonic matter [2] while the nature of more than 96% (73% in the form of dark energy and 23% in the form of dark matter) of the matter and energy in the universe are unknown. A possible solution for the dark matter riddle is Weakly Interacting Massive Particles (WIMPs) which are are hypothetical particles and interact through the weak force and gravity. This chapter summarizes the evidences for the existence of the dark matter and direct detection of the dark matter is reviewed. Methods for the low background techniques are then introduced followed by liquid XENON detectors for the dark matter searches.

1.1 Cosmological Motivation for Dark Matter

The evolution of the universe is described using the Big Bang theory which is supported by Hubble's law of an expanding universe [3], the first measurements of the cosmic microwave background (CMB) [4] and the helium to hydrogen ratio as an indicator of primordial synthesis of the elements. The theoretical framework relies on general relativity and on the idea that the geometry of space-time is determined by the energy content of the universe. If we consider the universum isotropic and homogeneous at large scales, a specific form of the metric, the so called Friedman-Robertson-Walker (FRW) metric [5] is applicable.

$$ds^2 = -dt^2 + a^2(t)[\frac{dr^2}{(1-kr^2)} + r^2(d\Theta^2 + \sin^2\Theta d\phi)] \tag{1.1}$$

The scale factor $a(t)$ determines the physical size of the universe and a constant k determines the spatial curvature of the universe ($k = 0$, $k = +1$, $k =$ -1 for a spatially flat, closed or open universe.). As a consequence of expanding universe, the light spectra of distant galaxies is shifted towards the red band. In the context of the FRW metric the expansion of the universe is described by the Hubble rate of expansion,

$$H = \frac{\dot{a}(t)}{a(t)}. \tag{1.2}$$

Friedmans equation can be written in terms of Hubble parameter H and the critical density [6] ρ_c (such that in the absence of a cosmological constant $\rho = \rho_c$ corresponds to a flat universe) and cosmological density parameter Ω_{tot} as,

$$\rho_c = \frac{3H^2}{8\pi G_N} \quad and \quad \Omega_{tot} = \frac{\rho}{\rho_c}, \tag{1.3}$$

where G_N is Newton's gravitational constant, ρ is the density of the universe. Finally, combining the above described equations yields

$$\Omega_{tot} - 1 = \frac{k}{H^2 a^2}. \tag{1.4}$$

Such that $k = 0$, $k = +1$, $k =$ -1 corresponds to $\Omega_{tot} = 1$, $\Omega_{tot} > 1$, and $\Omega_{tot} < 1$ respectively.

Defining normalized densities of matter, Ω_m, curvature, Ω_k, and cosmological constant terms, Ω_Λ, as

$$\Omega_m = \frac{8\pi G_N \rho_0}{3H_0^2}, \;\; \Omega_k = \frac{-k}{H_0^2 a^2}, \;\; \Omega_\Lambda = \frac{\Lambda}{3H_0^2}, \tag{1.5}$$

where Λ is the cosmological constant and ρ is the density of the universe (subscript 0 denotes present day values) and finally

$$\Omega_m + \Omega_k + \Omega_\Lambda = 1. \tag{1.6}$$

Predictive power of the Big Bang theory successfully estimates the observed relative abundances of light elements, the isotropic and homogeneous expansion of the universe and the existence of CMB. On the other hand this theory poses the problems concerning the initial conditions. It does not explain finite baryon density, extraordinary flatness and smoothness of the universe on very large scales and the origin of primordial density

perturbation. Cosmological inflation, which is an exponential expansion period in the early universe where the total energy density of the universe is dominated by vacuum energy offers a solution to the above mentioned problems. It explains the isotropy and homogeneity on very large scales [10] and it predicts a universe very close to flat (i.e. k=0). The observed Cosmic Microwave Background fluctuations provide now strong evidences that Ω_{tot} is very close to unity ($\Omega_{tot} = 1.02 \pm 0.02$) [7]. The Wilkinson Microwave Anisotropy Probe (WMAP) and high red-shift SuperNova (SN) observations also indicates a non-zero value for the cosmological constant (therefore existence of Dark Energy) and give consistent results for the value of Ω_m [7] [8]. The contribution of the luminous matter to the total density is however very small (Ω_{lum} = 0.002 - 0.006 [9]) and indicating the presence of Dark Matter in the universe.

1.2 Direct Detection of Dark Matter

Weakly Interacting Massive Particles (WIMPs) are hypothetical particles proposed to solve the Dark Matter problem. These particles interact through weak forces and gravity. This reduce the probability of their detection. Since WIMPs do not interact via electromagnetism they cannot be seen directly. These properties makes WIMPs one of the most compelling dark matter candidate.

Direct detection of these heavy particles (m_w =100 GeV$\cdot$ c^{-2}) is possible by the observation of nuclear recoils of the target nuclei. In the calculation of the WIMP direct detection rate, the local dark matter density ρ_0, velocity dispersion, the WIMP mass and the cross section on the target nuclei are crucial parameters. ρ_0 can be inferred from the measurement of rotation curve of our own galaxy. Using an isothermal sphere model which is the simplest parameterization of the spatial distribution of matter in an astronomical system, for the dark matter halo at the position of the sun the mean density of particles trapped in the gravitational potential well of the galaxy is expected to be ρ_0 $\sim$0.39 GeV$\cdot$cm^{-3} [11]. According to this model the local velocity distribution in the galactic rest frame is Maxwellian:

$$f(v)d^3v = (\frac{1}{v_0^3\pi^{3/2}}) \exp(\frac{-v^2}{v_0^2})d^3v, \tag{1.7}$$

where v_0 is the velocity at the local (Sun) position.

The measured rotation curve of our galaxy rises until a value of v_0=254$\pm$16 km$\cdot$s^{-1} [12] and then stays constant. Direct detection of dark matter relies on the interaction of WIMP dark matter particles with the target nucleus. Considering the WIMP mass and nucleus mass are identical ($m_w = m_N = 100\, GeV \cdot c^{-2}$), interaction between WIMPs and nucleus cause the nucleus to recoil. Since WIMP particles move at non-relativistic velocities, the deposited energy due to WIMP interaction can be calculated as

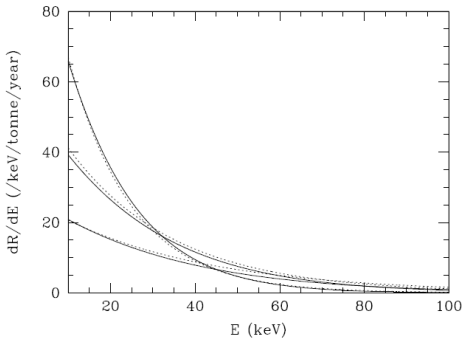

Figure 1.1: Solid lines represents normalized recoil spectra for WIMP elastic scattering for WIMP masses (from top to bottom at E = 0 keV) of 50, 100 and 200 GeV. The dotted lines represents exponential background spectra due to neutron interactions. The WIMP recoil spectra are close to exponential and thus can be mimicked by an exponential background [15]

$$E_r = \frac{m_w^2 \cdot m_N}{(m_w + m_N)^2} \cdot v^2(1 - \cos\Theta), \tag{1.8}$$

where m_w and v are WIMP mass and velocity, respectively, and Θ is the scattering angle in the center of the mass frame. The recoil energy spectrum is given by [13]

$$\frac{dR}{dE_r} = \frac{\rho_0 \sigma_0}{2 m_w \mu^2} F^2(E_r) \int_{v_{min}}^{v_{esc}} \frac{f_1(v)}{v} dv \quad , v_{min} = \sqrt{\frac{E_r m_N}{2\mu^2}}, \tag{1.9}$$

where $f_1(v)$ is the velocity distribution with respect to the detector, m_N is the target nucleus mass, $\mu = (m_w \cdot m_N)/\ (m_w + m_N)$ the reduced mass, E_r is the recoil energy transferred to the nucleus and $F(E_r)$ is the form factor and σ_0 is the WIMP-nucleus interaction cross section in the limit of zero momentum transfer. The WIMP interaction cross section depends on spin dependent (SD) (axial) component which is proportional to $J(J+1)$ and spin independent (SI) (scalar) component which is proportional to the number of nucleons. Form factor reflects the spatial distribution of nucleons inside the nucleus and parametrizes the loss of coherence as the WIMP energy increases. The term v_{min} is the minimum WIMP velocity able to generate a recoil energy E_r, and v_{esc} is the maximum WIMP velocity set by the escape velocity in the halo model. Figure 1.1 illustrates the quasi-exponential dependence of the signal rate on the recoil energy for three hypothetical WIMP masses.

1.3 Experimental Requirements

Despite the rare interaction of WIMP dark matter particles, their detection is still potentially possible. The flux of WIMPs is quite large and can be calculated from the density of WIMPs ($\rho_w = 3000\, WIMPs \cdot m^{-3}$) and from its velocity ($v_w = 220\, km \cdot s^{-1}$). The flux of WIMPs is calculated to be, $\Phi_{WIMP} = \rho_w \cdot v_w = \sim 10^5 cm^{-2} \cdot s^{-1}$. The problem lies, because of small WIMP interaction cross section $\sigma = 10^{-8} pb$, in the interaction with ordinary matter. The challenge for dark matter searches is to design an experiment that should have an energy threshold as low as possible due to the few keV energy deposition, it should have large mass (tons) of detector material due to the small cross section of WIMP-nucleus elastic scattering and highly suppressed background in order to allow a spectrum of rare nuclear recoils to be observed.

1.3.1 Low Background Techniques

The challenging point of dark matter search is to distinguish the rare expected WIMP signals out of background. In order to lower background, the first step is to understand the sources of background.

The background sources can be divided into the following components:

- Cosmic rays,
- Environmental radioactivity,
- Radioimpurities in detector and shield materials,
- Radon and its progenies.

Cosmic rays are extremely energetic particles, primarily protons and alpha particles, which originate in the sun, other stars, supernovae [20]. The cosmic ray particles interact with the upper atmosphere of the Earth and produce showers of lower energy particles. Most of these lower energy particles are absorbed by the Earths atmosphere as they travel down to the surface. Cosmic radiation at sea level consists of 70 % muons, 30 % electrons and less than 1 % protons and neutrons. Because of their high penetration ability, muons play an effective role in the production of the background directly by depositing energy in traversing the detector itself. This situation results in the creation of primary and then secondary electrons and finally photons. Direct energy deposition in the detector leads to an enormous energy deposition, or indirectly by interacting with materials surrounding the detectors results in X-ray, γ-ray, and neutron emission. Detector can be shielded against cosmic radiation by placing it in an underground laboratory. Installation of a muon veto system which can consist of anti-coincidence

detectors or a veto counter device which should encapsulate the detector will be effective for the background rejection of penetrating muons.

Primordial radionuclides are one reason for the environmental radioactivity. They are long lived, with half-lives often on the order of billions of years. The most common primordial radionuclides are ^{40}K, a β emitter element with an isotopic abundance of 0.012 % and ^{87}Rb, which is a pure electron emitter and has 27.8 % isotopic abundance. It readily substitutes for potassium in minerals, and is therefore fairly widespread. Natural radioactive decay chains of uranium, thorium and actinium also belong to the primordial radionuclides and they are the dominant environmental background sources.

Materials which used to shield a detector against environmental γ-rays should have high atomic number and low intrinsic contamination. Hg has a high radiopurity that can be even further enhanced by repeated distillation. The longer living isotope of Hg (^{194}Hg $T_{1/2}$=520 years) can only be produced by exposure to high energy neutrons. However, container required for Hg with high radiopurity is difficult to produce and Hg is rather expensive material. Oxygen-free high conductivity copper is one of the radiopure material and thus widely used innermost shield layers of the low background detectors. However, it has a rather high cross section for capture of thermal neutrons and for the cosmogenic production of radioactive nuclei. High atomic number of lead makes this material very suitable to shield the detector against the γ rays which come from the decay of primordial radionuclides. Its low neutron cross section significantly minimize production of radionuclides by the capture of thermal neutrons. Its low interaction probability with the cosmic rays also further prevent formation of radionuclides by the cosmic activation. On the other hand, intrinsic contamination of ^{210}Pb which is a β emitter with half-life 22.3 years is rather high. Lead with very low ^{210}Pb contamination is available but rather expensive compared to normal lead. Hence, a shield with shell-like structure with decreasing ^{210}Pb contamination would be more economic and 10 or 20 cm thick lead shield will be enough to block the incoming γ s.

The presence of primordial radionuclides in materials used in the detector and shield construction have a wide range of contamination. Therefore, the degree of radiopurity is of crucial importance for the further lowering of background of rare event searches. The main radioimpurities in the materials used for the detector construction are K, Th, and U. These impurities may arise from leftover chemical impurities present in the ore or mineral source of the material, or from contamination with substances used in the manufacture of components.

Because of its exceptional sensitivity, γ-ray spectrometry has an increasing trend for the purposes of material screening and selection of materials with low intrinsic contaminations for the experiments which are looking for rare events and thus need an extraordinarily low background. Studies on muon interactions [17] revealed that background of ionizing detectors are limited by cosmic ray muons, ^{222}Rn in the air, neutrons and the radioactive contaminations within the materials used in the detector and the

shield construction. After that, γ-ray spectroscopy was pioneered and currently different underground laboratories are equipped with High Purity Germanium (HPGe) detectors operated in a low background shield. Superior energy resolution of Ge detectors provides a diagnostic power to determine the energy peaks which are very close to each other. The sensitivity and very low intrinsic contamination which is feasible with germanium, enable to determine the activities of materials at mBq·kg^{-1} level. Sample chamber where material samples are placed for screening allows to measure the samples with different weight and sizes. Special attention has to be paid to remove the surface related contaminations of the materials which are going to be screened. This will be explained in the next chapter. A drawback of ultra low-level γ-ray spectrometry is that the measurements are time consuming (often days and weeks) and massive samples are needed in order to obtain enough statistics for the activities less than 1 mBq.

Laboratori Nazionali del Gran Sasso (LNGS) underground laboratory in Italy has 2 screening facilities, Gator (the details are given in the next section) and the LNGS low level counting facility, which consists of several High Purity Germanium (HPGe) detectors. This facility also includes the GeMPI-I and GeMPI-II detectors which are the most sensitive low-radioactivity HPGe detectors in the world and operated in connection with the Borexino and Gerda experiments [18] [19]. IAEA-MELs underground counting laboratory in CAVE (Monaco) has 4 HPGe detectors used to measure environmental radioactivity [21]. Another counting facility was installed at the Austrian Research Centers Seibersdorf (ATL03) as a part of the international monitoring system for verification of the Comprehensive Nuclear-Test-Ban Treaty (CTBT) [22]. The underground laboratory Felsenkeller (Germany) has a low level γ-ray spectrometer in an ultra low background shield to measure the environmental radioactivity in this laboratory [23]. SOudan LOw Background Gamma Counting Facility (SOLO) in Soudan underground mine includes a 0.6 kg HPGe detector (Diode-M) which have been used to screen the materials for the Majorana, CDMS, XENON10 and LUX experiments [24] [25] [26] [27] [28].

For samples with a total mass too small to obtain a reasonable sensitivity with the Ge detectors, Inductively Coupled Plasma Mass Spectrometry (ICP-MS) which is widely used both in research and industry can be an alternative. ICP-MS, that relies on to measure the mass to charge ratios can be used to determine the radioactivity of these samples. The system consists of two parts. Inductively coupled plasma ionize argon gas ($Ar \rightarrow Ar^+ + e^-$) by using an electrical current in wires surround the gas. Then, sample is introduced and extreme temperature of the plasma causes the sample first to separate into atoms and finally these atoms are ionized as well. The ions are then accelerated in an electric field and they are separated according to their energy in this field and in a magnetic field they are separated according to their momentum. Finally, the ion beam is directed onto a detector. This method has advantages of high speed, precision and sensitivity.

^{222}Rn with half-life 3.82 days is an important source of radioactivity in air and is

present in laboratories at a concentration of about 40 $Bq \cdot m^{-3}$ [59]. Since ^{222}Rn can diffuse into the shield, it must be enclosed in a gas tight box, which is flushed with nitrogen gas and maintained at a slight overpressure in order to prevent radon from penetrating the shield.

1.4 Liquid Xenon Detectors for Dark Matter Search

1.4.1 XENON100

The goal of the XENON dark matter experiment is to detect WIMP dark matter particles via their elastic scattering on Xe nuclei. As a proof of principle, the XENON10 detector [27] [29] was constructed and operated successfully at Laboratori Nazionali del Gran Sasso (LNGS) between 2006 and 2007. In the second phase of the experiment (XENON100) [30], the aim was to increase the sensitivity of the experiment by increasing the detector mass and at the same time decreasing the background by the careful selection of the construction materials. Figure 1.2 shows the reached and expected sensitivity for the last XENON100 science run to the spin-independent elastic WIMP-nucleon cross-section as function of WIMP mass m_χ. [31].

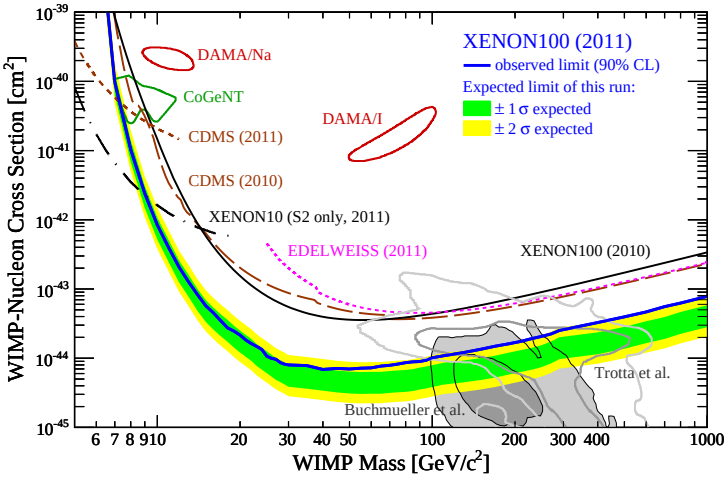

Figure 1.2: Reached exclusion limit at 90 % CL, (thick blue line) and expected sensitivity for the last XENON100 run (yellow / green band) to the spin-independent elastic WIMP-nucleon cross-section as function of WIMP mass m_χ [31]. The limits from XENON100 (2010) [30], EDELWEISS (2011) [32], CDMS (2009) [33], CDMS (2011) [34] and XENON10 (2011) [35] are also shown. Expectations from CMSSM are indicated at 68% and 95% CL (shaded gray [36], gray contour [37], as well as the 90% CL areas favored by CoGeNT [38] and DAMA (no channeling) [39].

The XENON100 detector [40] is a dual-phase (liquid-gas), three dimensional position sensitive time projection chamber (TPC) filled with 161 kg of ultra pure liquid xenon. The active target of the XENON100 is 62 kg of liquid xenon surrounded by 99 kg of liquid xenon acting as a veto. The TPC is enclosed in a PTFE (Teflon) can of 30 cm height and 30 cm diameter. Teflon is a very suitable plastic with very good UV light reflective features [41]. The entire detector includes 242 square (1"×1") low radioactivity photo-multiplier tubes (PMTs)(Hamamatsu R8520-06-Al). These PMTs work at liquid xenon temperatures (-100 ^{o}C) and are sensitive to the xenon scintillation wavelength (λ=178 nm). 98 PMTs are located above the target in the gas phase, arrayed in concentric circles. Bottom side of the TPC is surrounded by 80 PMTs placed very close to each other. The remaining 64 PMTs were used to surround veto looking at side, top and bottom around the TPC. Figure 1.3 shows a detailed CAD drawing of the XENON100 detector (left). 3-dimensional drawing of XENON100 (middle) and picture of the detector (right).

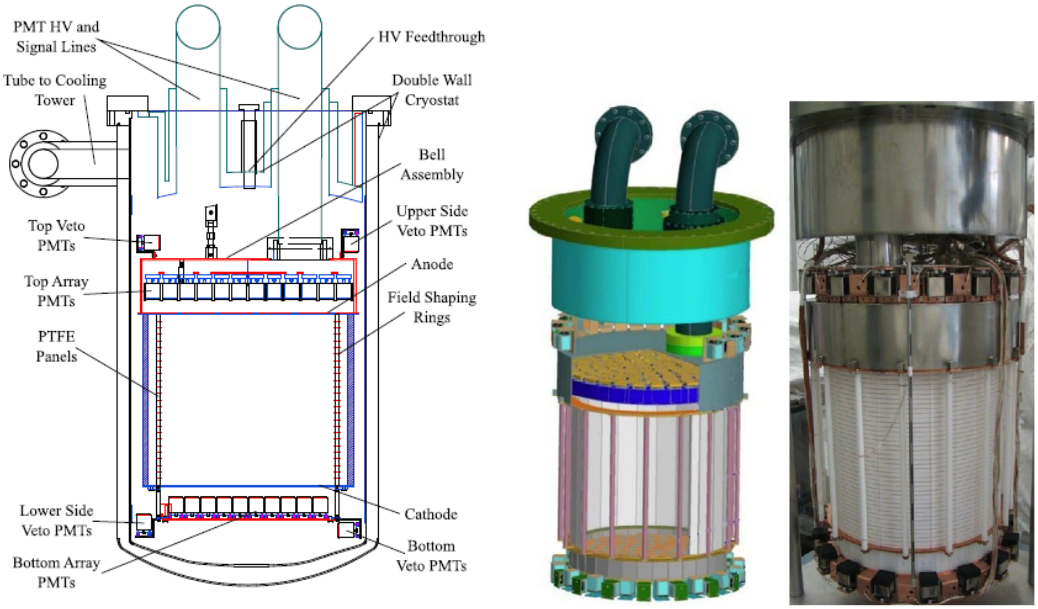

Figure 1.3: Detailed CAD drawing of the XENON100 detector (left) [40]. 3-dimensional drawing of XENON100 (middle) and picture of the detector (right) [42].

Figure 1.4 illustrates the working principle of XENON100. Particle interactions in liquid xenon creates prompt primary scintillation (S1) which are recorded by the PMTs placed on top and the bottom of the detector. Particle interactions also create ionization electrons. In a drift field ($E_d \sim 0.5$ kV/cm) applied across the TPC electrons drifted and extracted into gas phase by the application of extraction field across the

liquid-gas interface ($\sim$ 12 kV/cm). In gaseous xenon, electrons are accelerated and subsequent collisions with Xe atoms produce a large burst of secondary scintillation (S2) proportional to the ionization charge. The signal is again detected by the two arrays of PMTs. Different ionization density of nuclear recoils and electron recoils results in a different S2/S1 ratio which can be used to discriminate electron recoils from nuclear recoils. Figure 1.5 shows a typical single nuclear recoil in xenon (left) and a typical single scatter of γ (right). It can be interpreted that $(S2/S1)_{WIMP} \ll (S2/S1)_{gamma}$.

100.9 live days of data taken with the XENON100 detector between January and June 2010 were analyzed. Figure 1.6 [31] shows the results from this analysis. As it can be seen from this plot, only three candidate events (red circles) fall into the WIMP search region defined by the energy window 8.4 - 44.6 keV_{nr} (nuclear recoil equivalent energy) with an expected background 1.8 $\pm$ 0.6 events. Therefore, XENON100 has set the most stringent limit on dark matter interactions today, excluding spin-independent elastic WIMP-nucleon scattering cross-sections above 7.0×10^{-45} cm^2 for a WIMP mass of 50 GeV/c^2 at 90% confidence level [31].

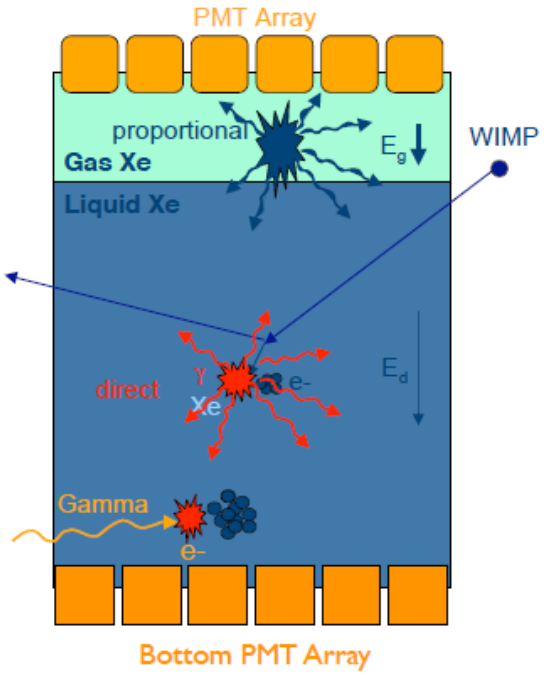

Figure 1.4: Illustration of working principle of a 2-phase TPC [43].

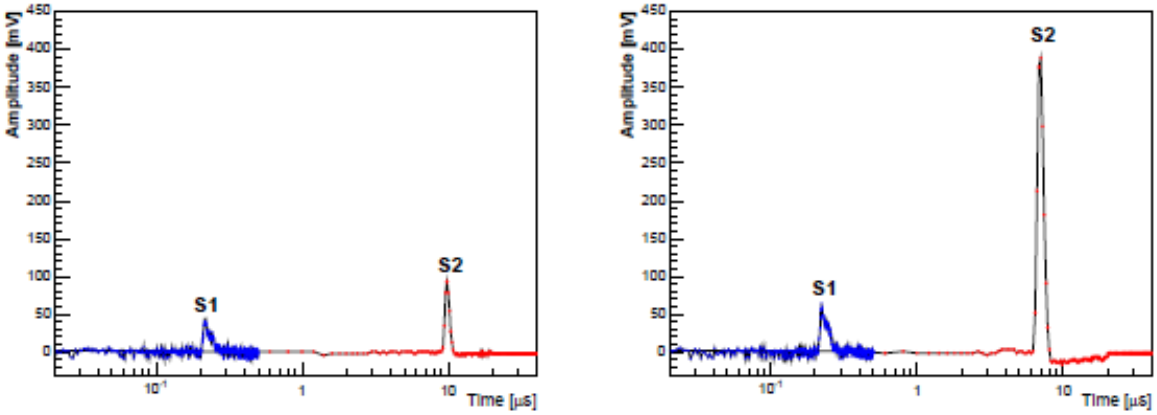

Figure 1.5: A typical single nulear recoil in Xenon (left) and a typical single scatter of γ (right) [44]. It can be interpreted that $(\mathrm{S2/S1})_{WIMP} \ll (\mathrm{S2/S1})_{gamma}$

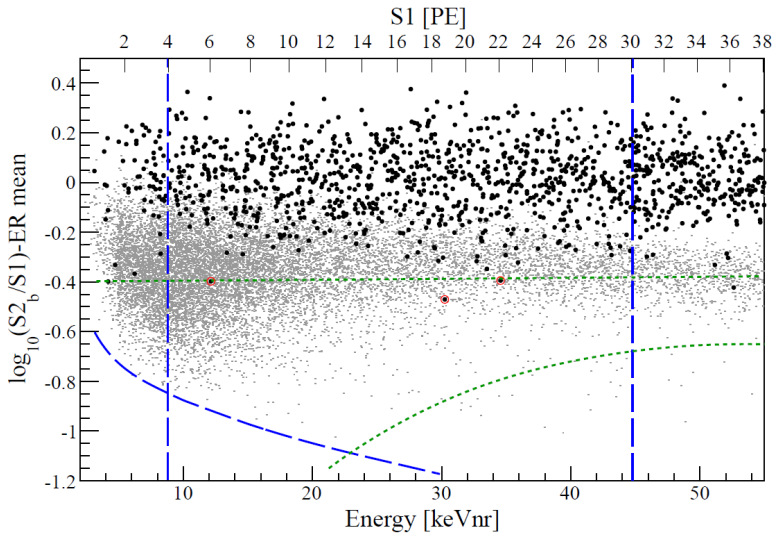

Figure 1.6: Observed event distribution using the discrimination parameter $\log_{10}(\mathrm{S2}_b/\mathrm{S1})$. Only three candidate events (red circles) fall into the WIMP search region defined by the energy window 8.4 - 44.6 keV_{nr} (nuclear recoil equivalent energy) with an expected background 1.8 $\pm$ 0.6 events [31].

1.4.2 XENON1T

The next step of the XENON dark matter project is to construct a ton scale detector, to increase the sensitivity for the spin independent WIMP-nucleon interactions to $\sigma \sim 5 \times 10^{-47}$ cm^2 by further increasing the detector mass and at the same time reducing the background. Time Projection Chamber (TPC) of XENON1T will contain $\sim$ 1 ton of ultra pure liquid xenon acting as a fiducial volume while 1.4 tones of liquid xenon surround the TPC and will provide a self shielding against the environmental radioactivity. The double walled cryostat of XENON1T will be made of titanium and it will be suspended inside a 10 m-diameter water tank together with PMTs. These PMTs read the Cherenkov light in the water and thus the water shield serves as a muon veto system. As it was done in the XENON100 phase, all supporting equipments including Pulse Tube Refrigerator (PTR) will be placed outside of the shield. For the light read out of XENON1T, R11410 PMTs from Hamamatsu will be used. Figure 1.7 illustrates the schematic of XENON1T.

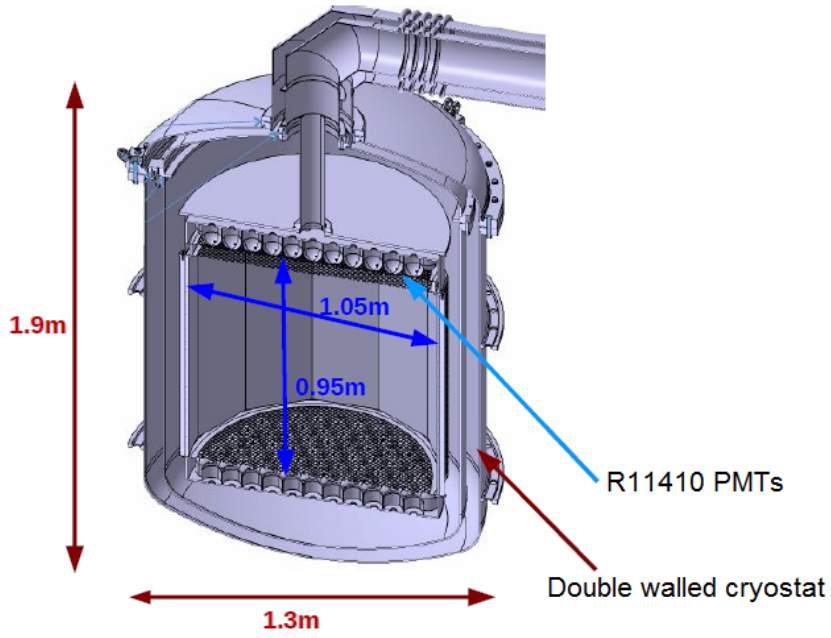

Figure 1.7: Schematic of XENON1T detector design [45]

As it was realized in the previous phases of the XENON program, all the materials which are going to be used for the construction of the XENON1T will be screened by using the low background counting facility (Gator, details are given in the next chapter) to obtain the radioactivities of the candidate construction materials and to select the radiopure ones for the XENON1T construction.

1.4.3 DARWIN

DARWIN (DARk matter WImp search with Noble liquids) [46] [47] is an R&D and design study which brings several European and U.S. working groups, ArDM [48], XENON and WARP [49], together to share their expertise in the dark matter search with the noble liquid scintillators.

DARWIN aims to test the cross section region below 10^{-47}cm^2 and measure the dependence of the rate on the target material by operating the LXe and LAr under same experimental conditions and therefore to better constrain the WIMP mass below 500 GeV/c^2. Since ^{40}Ar has no spin and ^{129}Xe and ^{131}Xe have nuclear spins of the ground states $1/2^+$ and $3/2^+$ and abundances of 26.4 % 21.2% respectively, it will provide information about spin-independent and spin-dependent [50] couplings. Figure 1.8 shows the sensitivity to the spin-independent cross section as a function of exposure for liquid argon (LAr) and liquid xenon (LXe).

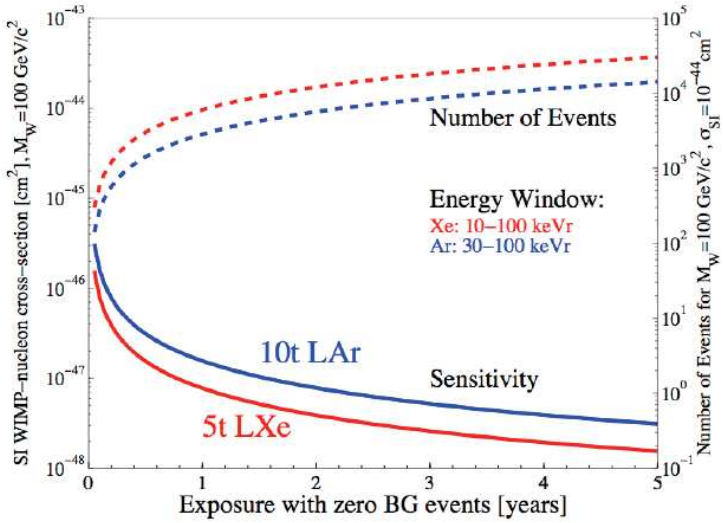

Figure 1.8: The sensitivity to the spin-independent WIMP-nucleon cross section as a function of exposure for 10 t LAr (blue) and 5 t LXe (red), for a WIMP mass of 100 GeV/c^2, an energy window of 30-100 keVr and 10-100 keVr in LAr and LXe, respectively and zero background events for a given exposure (left y-axis). The dashed lines show the number of events that would be detected for a WIMP-nucleon cross section of 10^{-47}cm^2 (10^{-8}pb) in LAr (blue) and LXe (red) (right y-axis).Figure taken from [46]

Chapter 2

The Gator Facility

Rare event searches, such as dark matter experiments or searches for neutrinoless double beta decays are limited by the background induced either by cosmic radiation or by the residual radiation emitted from the detector and the surrounding shield materials. Isolation of the detector against most of the cosmic radiation is possible by locating the experiment in a deep underground facility. Unless specially selected materials, so-called radiopure materials are used for the detector and the shield construction, there is not so much gain from installing the detector in an underground location. The exceptional high sensitivity of gamma-ray spectroscopy in underground laboratories has increasing applications and offers a standard method for material screening and selection for the rare event searches. An ultra- low level germanium spectrometer, named Gator, in an ultra-low background shield has been designed and installed at the Laboratori Nazionali del Gran Sasso (LNGS) to screen the materials and select the radio-pure ones for the XENON100, XENON1T, DARWIN and Gerda experiments. In this chapter, first the principles of the semi-conductor detectors are introduced. Details of the Gator detector and its low background shield are given. Finally, a slow monitoring system developed for the real time monitoring of the detector parameters is described.

2.1 High Purity Germanium Detectors

In the measurement of gamma ray energies above several hundred keV, two detector categories can be considered. Depending on the needs of application, inorganic scintillators, e.g NaI(Tl) can be used to measure the intensity of the gamma rays rather than a precise energy determination. Because of their excellent energy resolution, germanium semiconductor detectors have a great superiority for the analysis of complex gamma spectra involving many peaks. One drawback of germanium detectors compared to NaI(Tl) is the lower atomic number of the germanium which results in a photoelectric

cross section that is smaller by a factor of 10-20 [52]. The most important characteristic of semiconductor detectors is that the amount of ionization energy needed to transfer an electron to the conduction band is significantly lower and results in a better energy resolution. Whereas, the amount of the light produced in a scintillator is proportional to the energy deposition within the crystal. Thus, scintillation efficiency is very important factor. Scintillators are read out by PMTs and there are some light loss at the scintillator-PMT interface. Quantum efficiency of the PMT affects the produced photoelectrons and therefore on the signal amplitude as well. All these factors for scintillators subsequently results in statistical fluctuations in the number of photoelectrons finally leading a broadening in a peak in the energy spectrum.

The working principle of a semiconductor detector based on the formation of a p-n junction at the boundary between p-type and and n-type semiconductor created in a single crystal of semiconductor. P-type semiconductor is produced by implementation of acceptor atoms (such as boron, aluminum or gallium) to a semiconductor to increase the number of positive charge carriers (holes). N-type semiconductor is produced by doping the semiconductor with donor atoms (such as lithium,arsenic or phosphorous) to increase the number of negative charge carriers (electrons). At the boundary point, some holes diffuse from p-type to n-type region and there combine with electrons. In the same way, electrons diffuses from n-type to p-type region and combines with holes. This creates at the boundary surface a charge-free region (depletion region or sensitive volume). In the detection of the radiation with semiconductor detectors, the key factor which has to be taken into account is the thickness of the depletion region of the detector. Entering upon the sensitive volume, ionizing radiation produce electron-hole pairs along its path. The number of created free electrons and holes is proportional to the energy of incident radiation. Thus having a thicker sensitive volume will increase the probability of detection of radiation with high penetration capability. Depletion region of a semiconductor detector can be increased by applying a reverse bias voltage between the p-n junction. A p-n junction is reverse biased when positive polarity of a voltage source is connected to n-type and negative polarity is connected to p-type region. Reverse bias voltage cause an increase of potential difference across the p-n junction and therefore increase the sensitive volume. This voltage is important for the functionality of the detector as well. It creates an electric field which drifts electrons and holes resulting from interactions within the sensitive volume to the electrodes. Figure 2.1 shows a sketch and working principle of a semiconductor detector.

The depletion thickness can be calculated with [52]

$$d = \left(\frac{2 \cdot \epsilon \cdot V}{e \cdot N} \right)^2 , \tag{2.1}$$

where V is the reverse bias voltage and N is the net impurity concentration in the bulk semiconductor material. ϵ is the dielectric constant and e is the electronic charge.

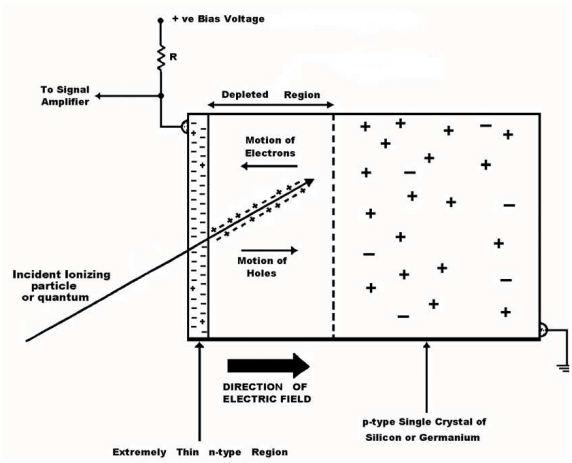

Figure 2.1: Sketch of a semiconductor detector. [53]. Entering upon the sensitive volume of the detector, ionizing radiation produce electron-hole pairs along its path. Number of created free electrons and holes are proportional to the energy of incident radiation. Electric field created across the diode drifts electrons and holes to the electrodes and finally an electric pulse is generated in the external circuit of the detector.

According to formula (2.1) the thickness of the depletion region can be increased either by increasing the reverse bias voltage, which is then limited by the breakdown voltage, or lowering the value of N through further reductions in the net impurity concentration.

One drawback of germanium detectors is that they must be cooled to liquid nitrogen temperatures to produce spectroscopic data. At higher temperatures, the electrons can easily cross the band gap in the crystal and reach the conduction band, where they are free to respond to the electric field created to drift electrons and holes. Detector system therefore produces too much electrical noise. Cooling to liquid nitrogen temperature (77 K) reduces thermal excitations of valence electrons so that interactions of ionizing radiation can give an electron the energy necessary to cross the band gap and reach the conduction band.

High purity germanium detectors can be produced in different configurations: planar or coaxial [52]. Planar germanium detectors are equipped with contacts provided on the flat surfaces of a germanium disk which has a typical thickness of a few centimeters. Thus the maximum depletion depth is limited to less than 1 or 2 cm. To produce a detector with larger depletion region, a different configuration, namely coaxial configuration can be used. Figure 2.2 illustrates the structure of the coaxial geometry. Here, one electrode is formed by the outer surface of the long cylindrical crystal. A second contact is formed at the center of the crystal by removing the core. In case of a closed-ended coaxial configuration, only part of the central core is removed and outer electrode is extended

over one flat end of the cylindrical crystal.

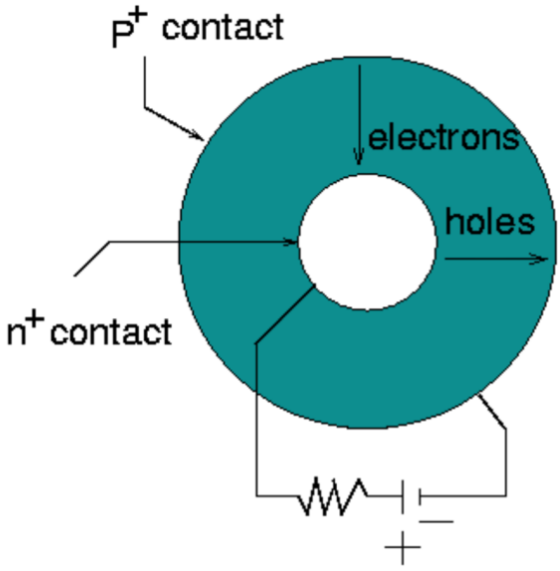

Figure 2.2: Cross-sectional view of large volume coaxial detectors.

2.1.1 Signal Development

Electron and Hole creation: After an energy deposition inside a germanium detector, electrons are lifted from the valence to the conduction band and electron-hole pairs are created. The band gap E_{gap} of germanium is only 0.73eV at 80K. However, to create an electron−hole pair the energy $E_{e^-h^+}$= 2.95 eV (at 80K) is needed. The difference is caused by the need to excite phonons in the lattice; germanium has an indirect band gap. Figure 2.3 shows a sketch of indirect band structure in germanium. The minimum of the conduction band does not occur at the same momentum as the maximum of the valence band.

The energy $E_{e^-h^+}$ to create an electron-hole pair depends on the energy of the incident particle, the deposited energy E_{dep} and the energy deposition mechanism. The mean number of electron-hole pairs $\langle N \rangle$ is

$$\langle N \rangle = \frac{E_{dep}}{E_{e^-h^+}} \tag{2.2}$$

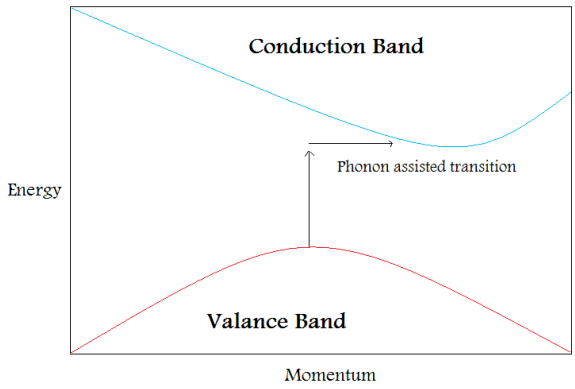

Figure 2.3: Schematic of indirect band structure in germanium. The conduction band is not vertically aligned to the valence band. Therefore, interaction of incident photons with electrons in the valence band will not provide the correct energy and momentum to shift an electron from the valance band to the conduction band without a change in momentum which comes from a phonon.

Electric Field: The electric field inside a true coaxial detector is determined by the electrically active bulk impurity density ρ(r) and the boundary conditions, i.e. the applied potential on the electrodes. It can be calculated by solving the Poisson equation in cylindrical coordinates.

Mobility: The drift velocity vector of the charge carriers $v_{e/h}$ and the electric field $E(r)$ are related by

$$V_{e/h} = \mu_{e/h} E(r), \tag{2.3}$$

where $\mu_{e/h}$ is the mobility of electrons and holes, respectively. The mobilities are determined by bulk impurities, lattice defects and lattice excitations. At such low bulk impurities as in almost perfect high purity germanium crystals, the mobility is dominated by the scattering of charge carriers off phonons, i.e. lattice vibrations. As these are temperature dependent, so are the mobilities $\mu_{e/h}$:

$$\mu_{e/h} \propto T^{-a}, \tag{2.4}$$

where a is found to vary between 1.6 and 2.8 [54]

Diffusion: A large number of electron-hole pairs are created at each energy deposition. During the drift towards the electrodes diffusion takes place. The diffusion can

be described by the Einstein relation:

$$\kappa_{e/h} = \frac{kT\mu_{e/h}}{e}, \tag{2.5}$$

where $\kappa_{e/h}$ is the transverse diffusion constant for electrons or holes, kT is the thermal energy and e is the electron charge. The transverse diffusion constant was calculated as κ_e= 210 cm^2/s and κ_h = 230 cm^2/s for holes and electrons [55]. Measurements show an upper limit on the lateral diffusion of $\sim$ 130 cm^2/s [55]

2.2 The Gator Facility

The design of the facility has been inspired by the layout of the world's most sensitive germanium spectrometers (GeMPI), operated at LNGS in connection with the Borexino and Gerda experiments [18] [19]. The core of the Gator facility consists of an 2.2 kg high purity germanium (HPGe) crystal installed as an ionization detector. The crystal is a p-type Germanium semiconductor crystal that was grown in a closed ended coaxial orientation. It is 82 mm in diameter and 81.5 mm in height. The electrode is made of germanium doped with lithium along the outer radial surface. Lithium behaves as a donor atom within germanium and provides extra conduction electrons for Germanium. This gives germanium n-type semiconductor characteristics. The inner electrode made of germanium doped with boron along the surface of a 10.5 mm diameter, 67 mm deep hole in the center of the crystal. Boron will be an acceptor atom within germanium. It will take away the weakly bound outer electrons from germanium and leave behind a hole. Thus germanium will get p-type semicondoctor characteristic. High voltage ($\sim$ 5 kV) applied between p^+ and n^+ contacts provides a strong electric field ($\sim$ 1.65 kV/cm) along the crystal's radial axis.

Figure 2.4 shows a picture of the detector taken during its installation at LNGS in 2007. The Ge crystal is enclosed in an ultra low background copper housing. The detector construction has been performed in close cooperation with Canberra semiconductors [56]. In particular, special attention has been paid to the selection of materials with ultra-low intrinsic radioactive contaminations. Figure 2.5 shows a cross-section of the Gator detector and its cryostat.

The relative efficiency, which is defined relative to a 7.62 cm$\times$7.62 cm NaI(Tl) crystal for the 1.33 MeV photopeak of ^{60}Co, at a source detector distance of 25 cm, is 100.5%. The excellent energy resolution of this detector allows the decays of ^{238}U, ^{232}Th, ^{60}Co, ^{40}K to be identified. Mainly these four decays are searched by the Gator in the various samples provided.

The cryostat is made out of ultra-low activity, oxygen-free high conductivity (OFHC) copper with the cooling provided by a copper dipstick in thermal contact with a liquid

Figure 2.4: Picture of the Gator detector and its shield. The HPGe crystal is enclosed in an ultra-low background copper housing [62].

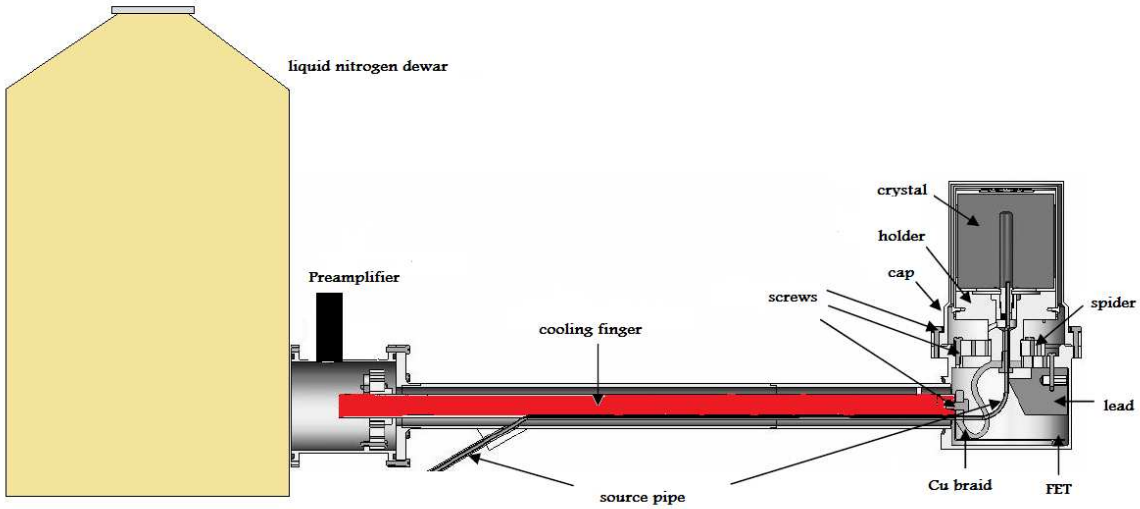

Figure 2.5: Cross-section of Gator detector and its cryostat.

nitrogen bath. Oxygen-free high conductivity copper is widely used in cryogenic systems because of its good thermal conductivity and refining processes used to produce this copper copper significantly reduces the amount of primordial and man made ra-

dioimpurities. The cryostat is U type, with the cooling rod shaped in a right angle below the cryostat to avoid a direct line of sight to the outside. The gate of the field effect transistor (FET) used for the charge readout is connected to the inner detector contact to provide an electrical signal to the preamplifier. It is also cooled and placed close to the detector. A very low activity lead piece is placed in front of the FET to block the gammas coming from FET and the preamplifier is placed outside the low background shield.

2.3 Shield Structure

The shield of the detector has been designed to provide capacity for large samples, an ultra-low background and easy access to the germanium spectrometer itself. It consists of 5 cm Cu and 20 cm of Pb: The innermost shield layer is made from ultra-low background oxygen free copper (from Nord Deutsche Affinerie [57]) to block the gammas coming from the surrounding outer lead layers. These copper plates also form the sample chamber with dimensions $25\times25\times33$ cm^3. The total volume of the sample chamber is about 19 liters. Residual surface contaminations of the Cu plates were removed by treating them with diluted sulfuric and citric acid solutions, followed by cleaning with deionized water. All steps have been performed under clean room conditions. Four lead layers of 5 cm thickness each (purchased from Plombum [58], Poland) surround the copper plates. The inner lead layer has a reduced ^{210}Pb activity of 3 Bq/kg while the outer 3 layers were constructed from lead with a ^{210}Pb activity of 75 Bq/kg. All lead bricks were carefully cleaned with ethanol before placing them in their place in the shield. Their arrangement is such that no direct line-of-sight to the HPGe detector is possible. Depending on the size and weight of the materials, they can be placed either on top of the crystal endcap or they can be placed around the detector within the sample cavity. Figure 2.6 (left) shows samples placed on top of the detector endcap for screening. (Right) shows large samples placed around the detector.

The large copper plates used to close the sample cavity which carry the upper lead layers were placed on sliding rails so that shield can be opened and closed in one action without handling individual pieces. The outermost lead layer is surrounded by additional 5 cm thick polyethylene plates against the ambient neutrons. The entire shield is enclosed in an airtight aluminum box and a glove box made of plexiglas was placed on top of it. The entire system is continuously purged by boil-off nitrogen gas ($\sim$ 8 liter/min) coming from a 100 l liquid nitrogen dewar to suppress the radon diffusion into the shield.

Figure 2.7 (left) shows a schematic view of the Gator facility at LNGS. The detector with its cold finger, the glove box and the open sample chamber can be seen . Figure 2.7 (right) shows a photograph of the finished set up of the facility. A glove box made

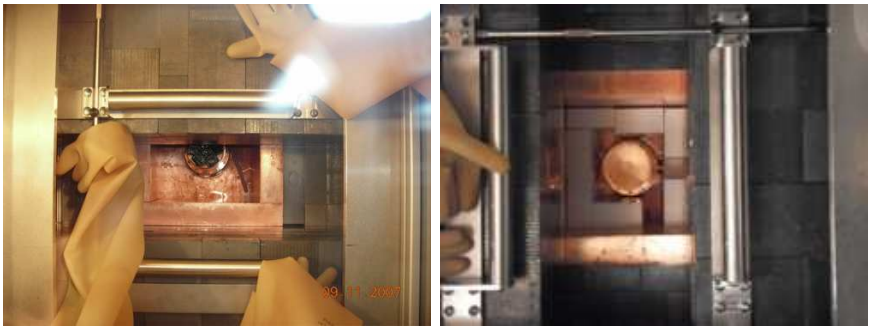

Figure 2.6: Samples placed on top of the detectors endcap (left) and samples distributed around the detector (right) [62].

of plexiglas including an airlock system is placed on top of the aluminum housing.

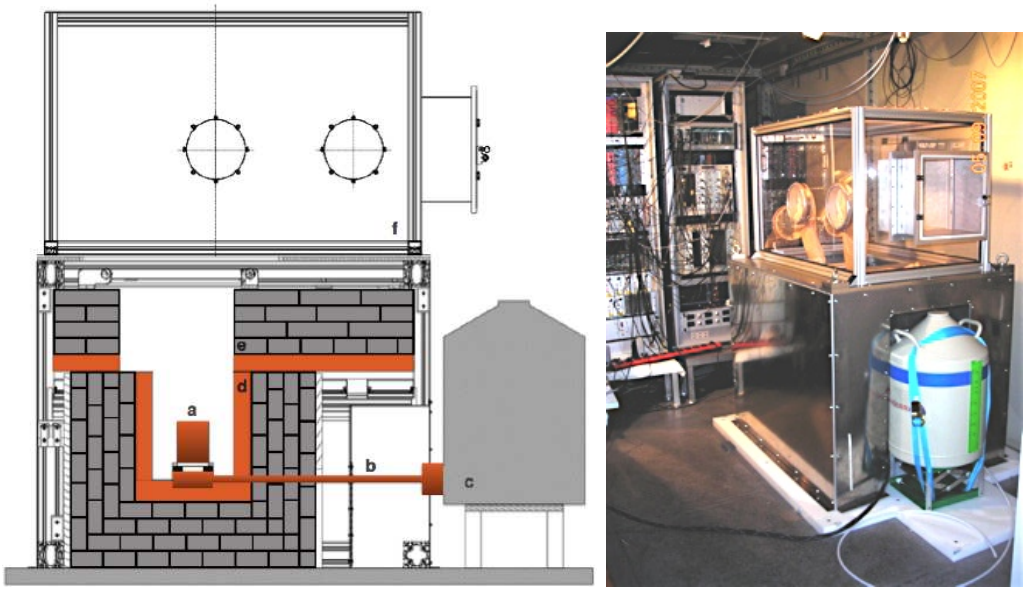

Figure 2.7: Schematic view of the Gator facility at LNGS. The detector (a) with its cold finger (b) and dewar (c), and the open sample chamber and the copper (d), lead (e) and the glove box (f) can be seen (left) [61]. Picture of the completed facility (right).

2.4 Sample Handling and Cleaning Procedures

The strongest source of radioactivity in the air arises from ^{222}Rn and its progenies which plays a role in the so-called plate-out effect, i.e. the deposition of Rn progenies sticking on statically charged surfaces, such as plastics or glass. Figure 2.8 shows an example of the plate-out effect measured in a Ge spectrometer [59].

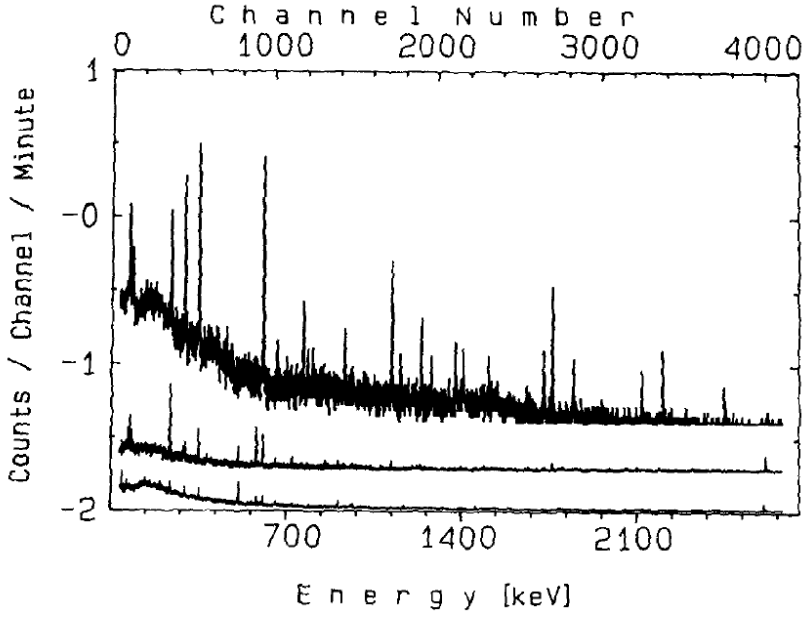

Figure 2.8: Ge-γ spectra of ^{222}Rn progenies on a plastic foil at different time intervals after plate-out: the first 130 min (top); 200-1500 min (middle); 2-22 days (bottom). The spectra are shifted by constant values in order to avoid overlap from statistical fluctuations [59].

Surface contaminations of all samples measured with Gator have been carefully removed in order to eliminate all external sources of radioactivity that might be present in the form of dust or dirt. Using an ultrasonic bath with ethanol for $\sim$ 30 minutes to mechanically remove surface contamination was the most used method for sample surface cleaning. Right after the cleaning, samples were enclosed in a sealed bag (if possible) and transported to the screening facility. Here they were placed for a few days inside the glove box in the pure N_2 atmosphere but outside the detector cavity in order to let the ^{222}Rn and its progenies decay.

2.5 The Gator Slow Control

In order to remotely monitor the crucial detector parameters, which are needed for a long term stable detector operation and the data acquisition, a slow control has been developed and implemented in the Gator Facility.

The liquid nitrogen level in the dewar used to cool the detector is of crucial importance. If the detector is operated at room temperature, high voltage applied to the detector will result in the production of an enormous leakage current ($\sim$ 0.5 A) which will destroy the FET.

The flow of nitrogen gas to purge the shield is important because, in case, the amount of nitrogen gas flow is low, data from sample measurement will be contaminated by radon diffused into shield and results in loosing of data and therefore counting time.

Leakage current across the germanium diode: Since germanium has low band gap compared to silicon, these detectors must be operated at liquid nitrogen temperature in order to reduce thermal generation of charge carriers thus leakage current. Otherwise, the noise produced by leakage current makes the resolution of the detector poorer. A plot of the leakage current will also serve as a temperature indicator of the detector. The leakage current of Gator at 77 ^oK is around 110 pA. If the temperature increases to 143 ^oK, the leakage current will be around 50 nA.

Detector high voltage must be stable at the adjusted value. Big fluctuations in the voltage will effect the thickness of the sensitive volume and the electric field used to drift charge carriers to the electrodes. This makes acquired data useless for the analysis.

The overall trigger rate is another indicator about stability of detector in terms of either hardware or environmental conditions. Since trigger rate depends on the activity of the measured samples, it will change by changing the sample. However, during the measurement of a sample, it is expected that the trigger rate must be stable. Big fluctuations in the trigger rate might arise from unstable operation conditions.

A capacitive method was used to measure the liquid nitrogen level in the cryostat dewar. The system consists of a 2 concentric metal tubes which were separated from each other with a thin insulator at the both ends which is acting as a capacitive sensor and a Universal Transducer Interface (UTI) chip developed by Smartec to read the capacity. The system measures the capacitance changes if the amount of dielectric material (in our case liquid nitrogen) between the metal plates changes. To measure the flow of nitrogen gas into the shield, an electronic flow controller (red-y series from Vögtlin instruments) was connected in serial to an analog flow controller in the purging line. The reading of the high voltage of the diode and the leakage current and was done with an analog to digital converter (LabJack U3). Since the high voltage of the detector is around 5000 volts, a high voltage probe to reduce the voltage by 1/1000 is used.

To calculate the trigger rate of the detector, the data acquisition system and software

(Genie 2000) were used. The data acquisition is provided by a Digital Signal Analyzer (DSA-1000) from Canberra semiconductors. It is a self triggering 14-bit channel integrated Multichannel Analyzer (MCA) based on digital signal processing technique (DSP). The same unit provides the high voltage to the crystal and the low voltage to the preamplifier. The DSA-1000 is controlled via a Universal Serial Bus (USB) interface. Acquisition sequences were established in Genie 2000 to take data in 6 hours intervals, save the acquired spectrum and give a report of the acquired spectrum. The report consists of channel numbers, counts, and the live time of the data acquisition in seconds. The trigger rate is then calculated by taking the total numbers of counts between a 100 keV and 2700 keV interval and dividing them by the live time of the acquisition. Therefore, noise, for example caused by leakage current, is excluded in the calculation of trigger rate. The code always checks if a new report is available and log the data for plotting. Figure 2.9 shows a block diagram of the Gator data acquisition and slow control system.

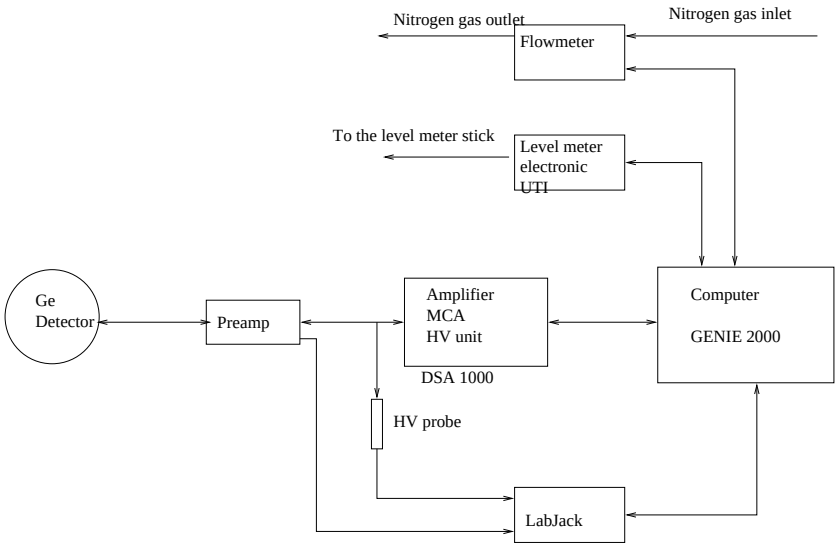

Figure 2.9: Block diagram of the Gator data acquisition and slow control system.

Figure 2.10, figure 2.12, figure 2.13 , figure 2.11 , figure 2.14 shows the stability plots taken between September 2010 and November 2010. If one of above mentioned detector parameter suddenly increases or decreases, the slow control will send an alarm by sms and an e-mail to the persons in charge of detector maintenance.

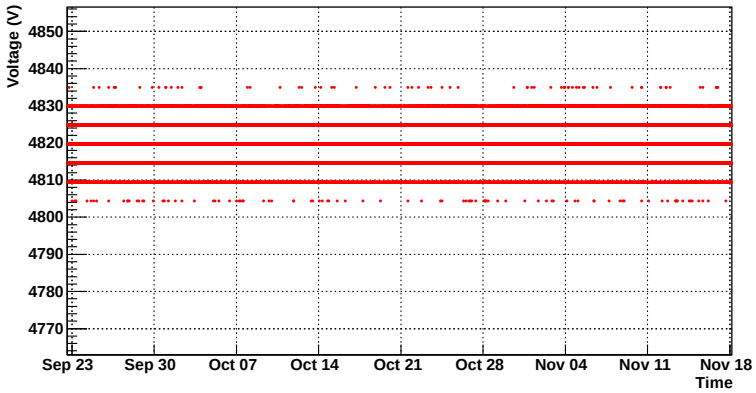

Figure 2.10: Stability plot of the detector high voltage between September 2010 and November 2010. Band structure occurring in this plot is due to the sensitivity of the ADC (LabJack).

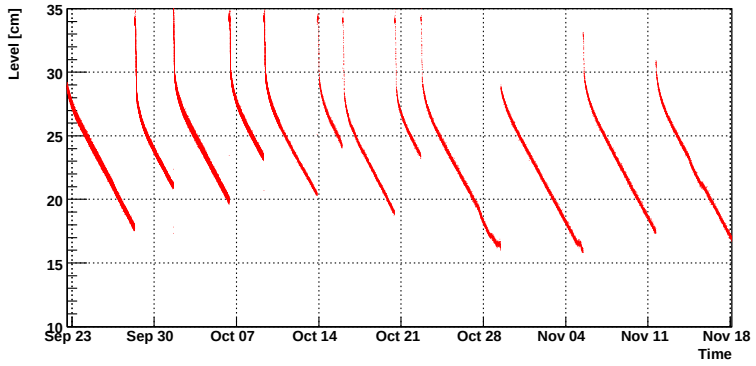

Figure 2.11: Plot of the liquid nitrogen level in the cryostat dewar between September 2010 and November 2010. When the dewar is completely full, the level which was calibrated according to the capacitance of the level meter stick is 35 cm. The sharp drops from 35 cm to 30 cm is due to the boiling and overflow of nitrogen after the insertion of dewar lid where the stick of the level meter is attached. The dewar is refilled periodically before the level of liquid nitrogen is below the minimum of the level meter.

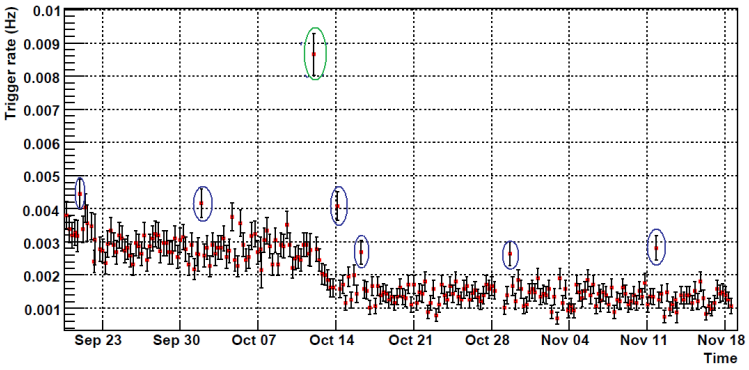

Figure 2.12: Plot of the detector's trigger rate taken September 2010 and November 2010. The reduction in the trigger rate around October 14 is due to the sample changing. The data point within the green circle results from data taking with a ^{60}Co source. Data points within the blue circles are due to periodic dewar refilling. For the refilling, the aluminum lid of the shield which closes the dewar cavity is removed. This causes diffusion of radon through the hole where copper dipstick of the cryostat placed. If the acquisition is started shortly after refilling, radon was not completely swept away and causes an increase in the trigger rate. The dewar refilling procedure was improved by filling it through the connectors which were mounted on the aluminum lid. Thus, it is not needed to remove the lid and radon can not diffuse into the sample cavity during the refilling period.

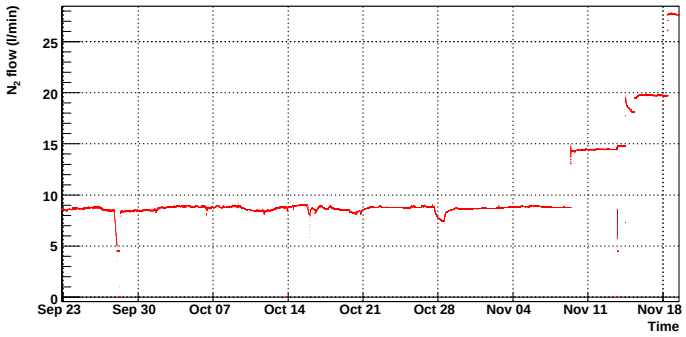

Figure 2.13: Plot of the nitrogen gas flowing into shield between September 2010 and November 2010. The increase in the flow rate starting at around November 8 is due to the manual increase of the flow rate to see the effect of the amount of nitrogen flow for the Rn protection. Starting from November 8 till November 19, the amount of gas flow was gradually increased from $\sim$ 9 l/min to 28 l/min. This test showed that the amount of nitrogen flow was already optimal at $\sim$ 9 l/min and the amount of the gas flow was reduced back from $\sim$ 28 l/min to 9 l/min.

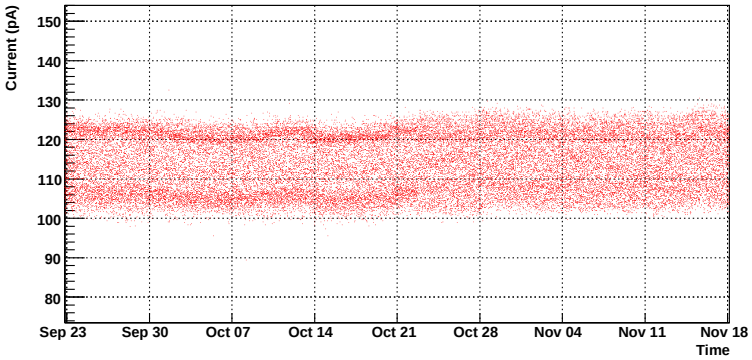

Figure 2.14: Stability plot of the leakage current which results from the thermal excitation of charge carriers within the germanium diode. Leakage current between September and November 2010 is stable within the sensitivity of the ADC (LabJack). Noise caused by leakage current is excluded in the calculation of trigger rate by taking the integral of counts between 100 keV and 2700 keV interval.

Chapter 3

Simulation and Calibration of Gator

Monte Carlo simulations play an increasingly important role in the design and operation of the particle detectors. The Geant4 geometry package provide tools to describe the detailed geometrical structure of a detector. The Geant4 kernel manages runs, events and tracking of the passage of particles through matter [60]. In case of Gator, simulations have played a key role to study the background and determine the efficiencies and finally to obtain the activities of the screened sample. For this reason, most of the significant components used to construct Gator detector were simulated with a Geant4 geometry. In this chapter the Geant4 model of Gator is described. Calibration measurements for the energy response of Gator and efficiency determination are then presented.

3.1 Geant4 Model of the Detector and the Shield

Monte Carlo simulations are essential to study the background of the facility and to obtain the activities of the screened materials. Most significant parts of the detector, such as, Germanium crystal including a dead layer from the electrodes, all of the Copper structures, such as cryostat, crystal holder, several teflon pieces and the shield of the detector, copper and lead parts, were coded using Geant4 particle tracking toolkit according to their original design. Figure 3.1 shows the Monte Carlo model of the Gator geometry. In case of material screening, the geometry of the screened materials and their chemical compositions can be coded into the existing Geant4 code according to their real geometry within the sample cavity . Precise geometry of the screened samples is important to determine the detection efficiency, which is needed for the activity calculation of the samples.

Figure 3.2 shows the Monte Carlo geometry of Gator out of its shield. Visible parts of this geometry are labelled. A few very thin and small parts, like crystal dead layer, IR windows made of mylar and kapton, signal contacts are not distinguishable in this picture.

Mass model of Gator was calculated by using the Monte Carlo model described above.

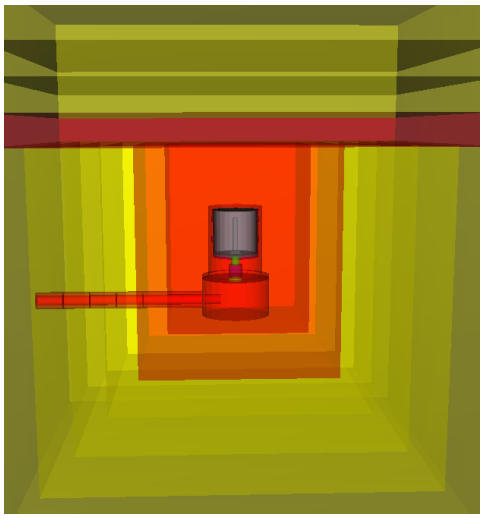

Figure 3.1: Geant4 model of the detector and the shield geometry. Lead layers (dark yellow), copper parts of the shield and cryostat (red) and germanium crystal (grey).

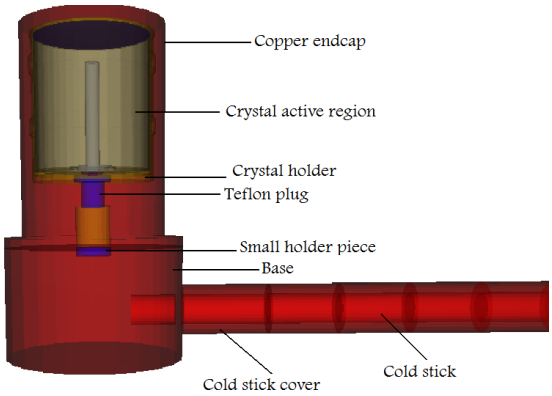

Figure 3.2: Monte Carlo geometry of Gator out of its shield. Visible parts of this geometry are labelled. A few very thin and small parts, like crystal dead layer, IR windows made of mylar and kapton, signal contacts are not distinguishable in this picture.

Table 3.1 represents the obtained results for each part of Gator coded into Geant4.

Material	Density	Material	Mass
Lead Shield	11.34 g/cm^3	Lead	4545.5 kg
Copper shield	8.92 g/cm^3	Copper	503.5 kg
Cold stick	8.92 g/cm^3	Copper	0.86 kg
Cold stick cover	8.92 g/cm^3	Copper	0.52 kg
Base	8.92g/cm^3	Copper	2.46 kg
Small holder piece in base	8.92 g/cm^3	Copper	23.4 g
Crystal holder	8.92 g/cm^3	Copper	1.1 kg
Endcap	8.92 g/cm^3	Copper	0.92 kg
Signal contact 1	8.92 g/cm^3	Copper	772.4 mg
Signal contact 2	8.92 g/cm^3	Copper	2.1 g
Crystal active volume	5.32 g/cm^3	Germanium	2.1 kg
Crystal dead layer	5.32 g/cm^3	Germanium	134.9 g
Teflon plug	2.2 g/cm^3	Teflon	10.2 g
Crystal cover	2.2 g/cm^3	Teflon	35.8 g
IR window	1.3925 g/cm^3	Mylar	61.8 mg
IR window	1.42 g/cm^3	Kapton	756.3 mg

Table 3.1: Mass model of Gator from the Monte Carlo simulations. The massive parts of the geometry are the lead and copper used to construct the shield of the detector. Cold stick transfers the cooling power of the cryostat to the Ge crystal. Cold stick is isolated with vacuum placed between cold stick cover and the cold stick itself. Crystal holder is a frame to keep the crystal stable and it is placed together with Ge crystal on the base. Endcap of the crystal encloses the crystal and the crystal holder. Crystal active volume is the sensitive part of the Ge crystal to the particle interactions. Crystal dead layer is on the surface of the crystal. It is not sensitive to particle interactions because of having the electrical contacts for the high voltage.

3.2 Energy Calibration and Linearity

The pulse height scale of Gator must be calibrated in terms of absolute gamma ray energy in order to identify various peaks in the sample spectra. Since a reliable calibration must include standard calibration sources with energies which covers the energy range of interest and since even the best spectrometers shows non-linearities over a full range of several thousand channels, it is always useful to have multiple calibration peaks at various energies in order to minimize such possible non-linearities. Thus Gator is cali-

brated with various calibration sources, such as ^{228}Th (238 keV, 583 keV, 785 keV, 2614 keV lines), ^{60}Co (1173 keV and 1332 keV lines), ^{109}Cd (88 keV), ^{133}Ba (356 keV), ^{137}Cs (662 keV), ^{57}Co (122 keV), ^{22}Na (1274 keV) and ^{54}Mn (835 keV) sources.

The conversion factor between channel numbers and energy was 0.71 keV/channel during 2007. Gator was shipped to Canberra for repair in 2008 because of a break down which was due to a liquid nitrogen shortage in the cryostat dewar. The FET assembly of Gator was completely changed. After the repair, it was seen that the conversion factor between channel numbers and energy increased to 0.86 keV/channel. This was possibly due to the slight increase in the feedback capacitor (C_{fb}). Figure 3.3 shows comparison of the calibration spectra acquired with ^{60}Co (left) and ^{228}Th (right) calibration sources with the one from a Monte Carlo simulations of the source detector geometry. For both decays, 10^6 decays were simulated and scaling factors obtained from the fit are: 9.040±0.0178 for ^{228}Th and 4.901±0.0808 for ^{60}Co. In both cases the data and the simulations are in a good agreement. Figure 3.4 shows the linearity of Gator with above mentioned calibration sources. Left plot shows the linearity in terms of channel numbers versus energy and right plot shows in terms of channel numbers/energy versus energy.

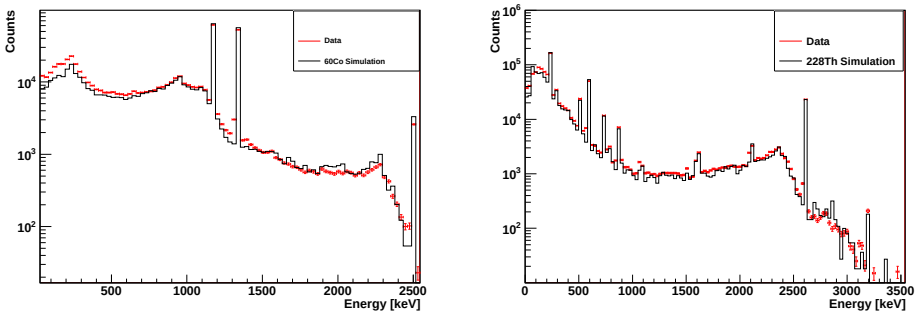

Figure 3.3: Left plot shows a comparison of the calibration spectrum acquired with ^{60}Co with the one from a Monte Carlo simulation. The lines at 1173 keV and 1332 keV are the characteristic ^{60}Co lines. Discrepancy between data and simulation below 300 keV is due to the thickness of the copper endcap which was thicker in the Monte Carlo geometry. This situation was corrected in the new geometry. Right plot shows a comparison of the calibration spectrum acquired with ^{228}Th calibration source with the one from a Monte Carlo simulation. The lines at 238 keV, 583 keV, 785 keV and 2614 keV do not only arise from ^{228}Th but also from its progenies.

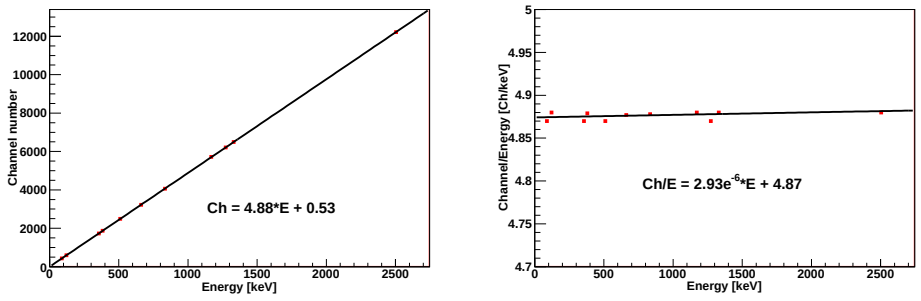

Figure 3.4: Linearity of Gator at different energies. Left plot was obtained by plotting channel numbers versus energy and right plot was obtained by plotting channel/energy versus energy.

3.3 Energy Resolution

Gamma rays which interact within the germanium detector produce peaks in the spectrum. The width of the peaks is determined by the resolution of the detector which is a very important characteristic for gamma spectrometers. High resolution enables separation of two lines that are very close to each other. In most applications the energy resolution is defined as FWHM/H_0 where FWHM = 2.35×σ and H_0 is the mean energy of a gamma line [52]. The energy resolution of a germanium detector is influenced by three effects. The full width at half maximum W_T expected from a fixed energy deposit is written as

$$W_T^2 = W_D^2 + W_X^2 + W_E^2 \tag{3.1}$$

where W_D^2 represents the broadening due to inherent statistical fluctuations of the number of charge carriers and is given by

$$W_D^2 = (2.35)^2 F E_{e^-h^+} E_{dep} \tag{3.2}$$

where F is the Fano factor which is of the order of 0.1 [52] and $E_{e^-h^+}$ is the energy needed to create an electron-hole pair. The W_X^2 is due to incomplete charge collection and also scales linearly with E_{dep}. The third term, W_E^2 , represents the contribution from electronic noise. This contribution is independent of E_{dep}. The energy resolution of Gator was obtained by fitting a Gaussian to the different energy peaks in the calibration spectra taken with the above mentioned calibration sources. Energy resolution of Gator is here defined as the ratio of σ to the mean energy of the gamma line. Figure 3.5 shows energy resolution of the detector. The data points were fitted with the function $\sigma^2(E)$=$E^2(2.35 \times 10^{-7}) + E(7.70 \times 10^{-4}) + (4.43 \times 10^{-1})$ [61].

FWHM values for large coaxial detectors vary between 1.7 and 2.3 keV for the 1332 keV ^{60}Co line [52]. The FWHM of the 1332 keV ^{60}Co line was measured to be 3.2 keV

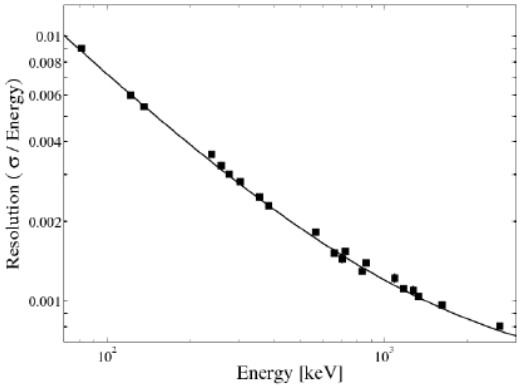

Figure 3.5: Energy resolution (defined here as the ratio of (σ/energy)) as a function of energy [61].

with Gator.

3.4 Efficiency Determination with Certified Sources

Interactions of gamma rays within the detector volume will usually result in an output signal. In case of alpha or beta, interactions in the form of ionization or excitation will take place right after the entrance of particle in the detection medium. Interaction range of these particles are small and they can produce enough ion pairs along their paths. In these conditions, detector will have 100% detection efficiency. Since uncharged radiations, like gamma rays, can travel large distances between interactions and before detection is possible, detector is always less than 100% efficient [52].

Efficiencies of the various gamma lines has an important role in the calculation of the activities for the screened samples and its determination relies on the Monte Carlo simulations. The detailed geometry of each screened sample is coded into the existing Geant4 model of Gator. In order to simulate each decay chain, the G4 Radioactive Decay library developed for Geant4 , which takes into account the branching ratios for the different gamma lines in one decay, is used. The detection efficiency (ϵ) of a specific gamma line can be determined by dividing the number of events detected under the line in question by the total numbers of the events simulated.

$$\epsilon = \frac{Counts\ in\ full\ absorption\ peak}{Number\ of\ events\ simulated} \tag{3.3}$$

The efficiency determination was cross-checked by using two extended sources and comparing their certified activity values with results from the measurement. Analysis

was performed by using the 2 different analysis methods, analysis of the most prominent lines and a χ^2 fit method. Details of these methods will be introduced in the next chapter. The sources used for this measurement, which had similar dimensions and weights, are CANMET-STSD2 (from the Canada Centre for Mineral and Energy Technology) and IAEA-Soil6 (from International Atomic Energy Agency). Both sources are soils taken from different places on the Earth, thermally treated and sieved several times in order to destroy any remaining organic matter. The homogeneity of the material had also been certified by the provider. Figure 3.6 shows the best fit of the simulations made for the decays in CANMET-STSD2 to the data taken with Gator and the table 3.2 shows the results obtained for this source by using χ^2 comparison method and the comparison to the certified values. Figure 3.7 shows the best fit of the simulations to the experimental data taken with Gator for IAEA-Soil6 and table 3.3 shows the same comparison as in table 3.2. Activity results obtained by using the analysis of most prominent gamma lines method from the screening of these two sources and comparison with certified values provided by two agencies are given in table 3.4 [61].

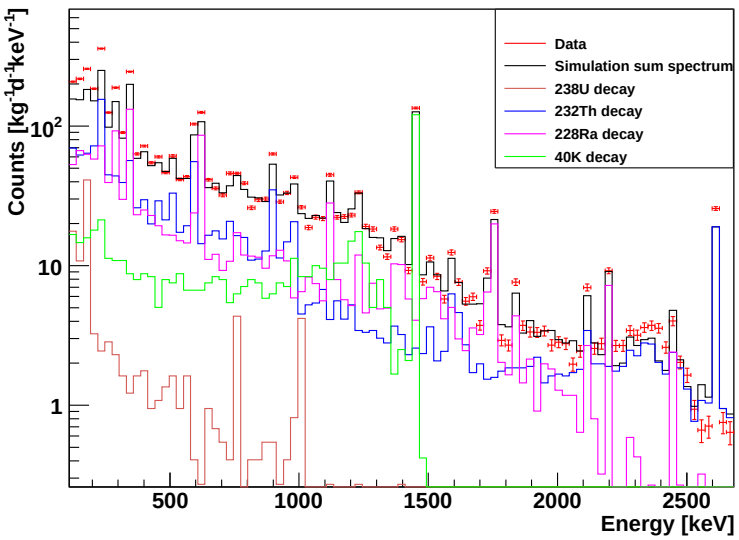

Figure 3.6: Best fit of the simulations made for the decays in the CANMET-STSD2 to the experimental data taken with Gator.

Isotope/chain	^{238}**U** (Bq/kg)	^{228}**Ra** (Bq/kg)	^{232}**Th** (Bq/kg)	^{40}**K** (Bq/kg)
Gator results	194.2±26.7	76.4±1.2	64.6±1.1	597±7.0
Certified Values	229.0±12.0	70.0± 5.0	69.9±5.3	540±20.0

Table 3.2: Activity results obtained for the CANMET-STSD2 certified source by using χ^2 comparison method and comparison to the certified values.

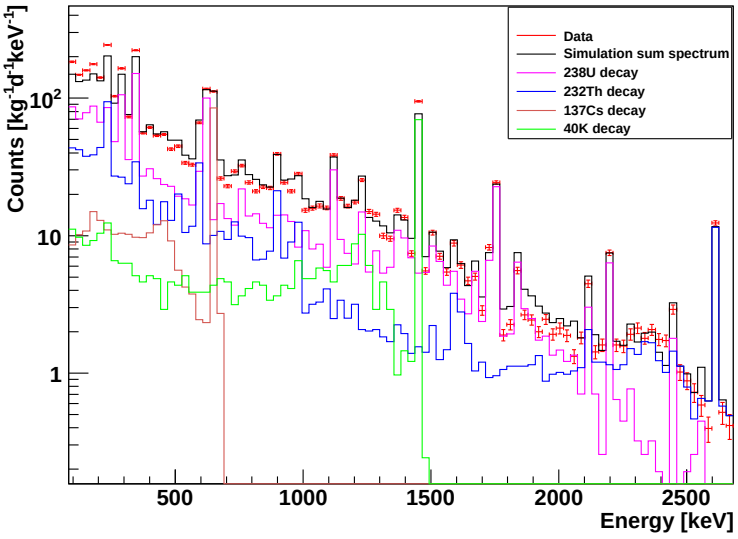

Figure 3.7: Best fit of the simulations made for the decays in the IAEA-Soil6 to the experimental data taken with Gator

Within the uncertainties, there is agreement between the results and the certified values for the decays of ^{238}U, ^{228}Ra and ^{232}Th for the CANMET-STSD2 and ^{238}U for the IAEA-Soil6. Activity results obtained with Gator for the ^{40}K decay within CANMET-STSD2 and for the ^{137}Cs decay within IAEA-Soil6 are higher than the certified values. These results indicate that the measurements performed with our spectrometer provide a reliable value for the activity of a given sample.

Isotope/chain	**^{238}U (Bq/kg)**	**^{137}Cs (Bq/kg)**
Gator results	85±0.6	63±1
Certified Values	80.0±7.0	54.0±2.0

Table 3.3: Activity results obtained for the IAEA-Soil6 certified source by using χ^2 comparison method and comparison to the certified value.

Nuclide	STSD2 Activity [Bq/kg]	
	Gator results	Certificated values
^{228}Ra	75±4	70±5
^{238}U	230±30	230±10
^{40}K	590±10	540±20
Nuclide	Soil6 Activity [Bq/kg]	
	Gator results	Certificated values
^{238}U	88±5	80±7
^{137}Cs	57±2	54±2

Table 3.4: Results obtained by using the analysis of the most prominent lines method from screening the CANMET-STSD2 and IAEA Soil6 sources and comparison with certified values provided by two agencies [61].

3.4.1 Energy Threshold

The energy threshold of Gator was investigated by looking at the low energy part of the 3 background spectra (the details of Gator background is given in chapter 5) as shown in figure 3.8. Energy threshold of Gator was around 40 keV in 2007 and the 2 Pb X-rays at around $\sim$ 72 keV and $\sim$ 84 kev are distinguishable in this spectrum. The energy threshold of Gator increased to 90 keV in 2008 and 75 keV in 2010.

The energy threshold is limited by the electronic noise which is superimposed on the signal source. In most cases, noise start near the beginning of signal chain where signal level is minimum and comparable to noise. At the further stages of the signal chain, the noise is smaller than the signal. Therefore noise created at the beginning stage of the signal formation is amplified by the same factor as the signal. The input stage of the preamplifier especially critical in the production of the noise. The electronic noise depends on the capacity and thus increases with the increasing capacity. The FET assembly of Gator was changed in 2008 and the new assembly has a new feedback

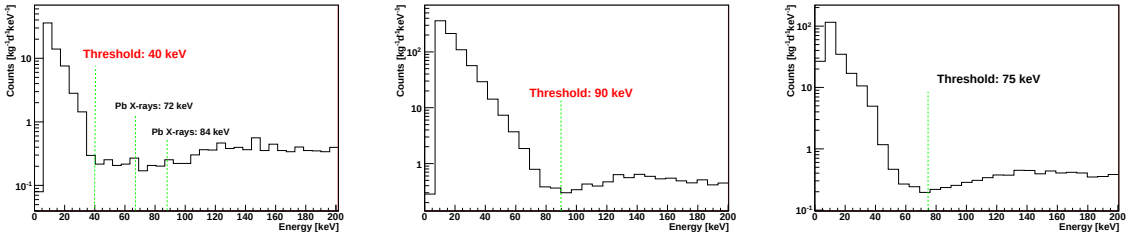

Figure 3.8: Energy threshold of Gator in 2007 (left), in 2008 (middle) and in 2010 (right). X-rays from Pb are distinguishable in the background in 2007 and the threshold is almost twice higher in 2008 and in 2010.

capacitor with slightly bigger capacity. Fluctuations in the leakage current and the fluctuations in the gate source current of the FET in the input stage of the Gator preamplifier could strongly effect the noise contribution and increase the threshold of Gator. A possible improvement of the threshold can be achieved by increasing the shaping time of the amplifier which is fed by the preamplifier. Since the amplifier shapes the pulses from the preamplifier to match the input range of the multichannel analyzer, an increase of the shaping time will not allow the noise to be amplified with the same amplification as the signal.

Chapter 4

Data Analysis Methods

Two different analysis methods were used in the analysis of the data from the screening measurements. The first method is based on the determination of the efficiencies from the Monte Carlo simulations for the most prominent γ-lines of the respective decay. For example, in the case of ^{238}U the γ-lines from the daughters of ^{226}Ra (^{214}Pb (352 keV)) and ^{214}Bi (609 keV 1120 keV and 1638 keV)) and in the case of ^{232}Th the γ -lines from ^{228}Ac (911 keV, 969 keV) and from ^{212}Pb (238 keV), ^{212}Bi (727 keV), ^{208}Tl (583 keV, 2614 keV) are used. The second analysis method relies on the chi-square minimization of the simulated spectra to the data. Each spectrum from simulations is scaled to the data to achieve the best fit and scaling factors resulting from the fit are used for the activity calculation.This section gives the details of the methods used in the background analysis of Gator and to obtain the activities of the screened samples.

4.1 Analysis of the Most Prominent Gamma-Lines

The first method used to determine the specific activities for the ^{238}U, ^{232}Th, ^{60}Co, ^{40}K is based on counting of events in the most prominent lines, after subtracting the background spectrum. The Compton background, estimated from the regions left and right of a peak, is subtracted as well. In order to decide whether the number of events detected are significantly above the background and an activity can be provided, the net signal counts (S_{net}) needs to be compared to the detection limit (L_d) which is the level of a net signal:

$$S_{net} = S - B \cdot \frac{t_S}{t_B} - B_C, \tag{4.1}$$

S is the number of counts in the $\pm 3\sigma$-region around a peak, B and B_C are the number of background and Compton-background counts in the same region, and t_S, t_B are the

measuring times for signal and background, respectively. The detection limit L_d for 95% C.L. is given by [63]

$$L_d = 2.86 + 4.78\sqrt{B_C + B \cdot \frac{t_S}{t_B} + 1.36} \tag{4.2}$$

For each peak, three cases can be considered [63]:

1. S_{net}<0: only an upper limit can be given and it is set to L_d (no net contribution from a signal)

2. 0<S_{net}<L_d: S_{net} exceeds zero, thus there is an indication that there is a contribution from the sample count but it can not be confirmed for the existing background level and and sample exposure. Therefore, an upper limit can be set to S_{net}+L_d

3. S_{net}>L_d: the detection limit is exceeded and activity is given.

For the third case, the specific activity and its 2 σ error is calculated as

$$A[Bq/kg] = \frac{S_{net}}{r \cdot \epsilon \cdot m \cdot t} \quad \text{with} \quad \frac{\Delta A}{A} = \frac{\Delta S_{net}}{S_{net}} \tag{4.3}$$

where r is the branching ratio for the specific line, m is the mass of the sample , t is the live time of the measurement and ϵ is the peak detection efficiency calculated by using the equation (3.3).

For the case in which an upper limit is given, S_{net} is replaced by L_d or by $(S_{net} + L_d)$ in equation (4.3). Table 4.1 shows the quantities used to determine the specific activities or upper limits using this method for a copper and stainless steel samples [61].

Sample	Used line [keV]	S_{net}	$B \cdot t_S/t_B$	B_c	L_d	Condition	Activity [mBq/kg]
Copper	239	0	0	93	49	$S_{net} < L_d$	<0.33
	352	-5	19	71	48	$S_{net} < L_d$	< 0.36
	1173	42	6	19	27	$S_{net} > L_d$	0.24±0.06
Stainless steel	352	66	7	58	42	$S_{net} > L_d$	4.3±0.9
	1773	236	2	19	25	$S_{net} > L_d$	7.2±0.9
	1461	-3	3	10	21	$S_{net} < L_d$	<5.7

Table 4.1: Examples of upper limit or specific activities calculation [61].

4.2 Fit of the data to a simulated spectrum

The activities or the upper limits for the screened samples are also calculated by using the χ^2 minimization method. This method was developed and tested as an alternative analysis method within the context of this thesis to cross-check the results obtained by the first analysis method. In general, prior to start the analysis, the background spectrum is subtracted from the sample spectrum and Monte Carlo simulations are performed for the decays of ^{238}U, ^{232}Th, ^{60}Co, ^{40}K within the detailed sample geometry. In case of an indication about any cosmogenic activation within the sample (like ^{54}Mn, ^{58}Co as it was shown in figure 4.3), the cosmogenic radionuclides are simulated as well. All the simulations are smeared with the energy resolution of Gator which is given in the previous chapter. The aim of this method is to model $\vec{y}$, the measured number of counts in each energy bin, as a function of $\vec{x}$, the energy bin value from the Monte Carlo simulation, with a functional dependence of the form

$$\vec{y} = \sum_{k=1}^{M} a_k \cdot f_k(\vec{x}), \tag{4.4}$$

where M is the number of simulated radioactive isotopes. $a_k \geq 0$ are the scaling factors for each isotope, and $f_k(\vec{x})$ are M Monte Carlo spectra.

Simulations are then fit to the measured sample data by keeping the scaling factors as free parameters and by minimizing χ^2 value for different fits determined bin by bin,

$$\chi^2 = \sum_{i=1}^{N} \frac{[y_i - \sum_{k=1}^{M} a_k \cdot f_k(x_i)]^2}{\sigma_i^2} \tag{4.5}$$

where $\sigma_i = \sqrt{y_i}$ is the variance in the observed number of counts in each bin and N is the number of bins over which the fit is performed. The statistical uncertainty in the Monte Carlo component is negligible. The minuit minimization package which offers different minimization algorithms [64] is used to perform the χ^2 minimization and to obtain the scaling factors and their errors, $a_k \pm \Delta a_k$, for every decay chain or isotope.

Activities of each isotope, for each measured sample can then be calculated by using the scale factors from the best fit and by using the formula

$$A_k[Bq/kg] = \frac{n_{sim} \cdot a_k}{m \cdot t} \quad with \quad \frac{\Delta A_k}{A_k} = \frac{\Delta a_k}{a_k} \tag{4.6}$$

where n_{sim} is the number of simulated events, m is the mass of measured sample and t is the live time of the measurement. The scaling factors from χ^2 minimization are assumed to describe a normalized Gaussian probability distribution function (PDF), $g^0(a) \equiv g^0(a, a_0, \sigma)$, with mean $a_0 = a_k$ and $\sigma = \Delta a_k$.

The method applied to decide between a real detection and an upper limit is based on [65]. A peak detection can be claimed when the lower limit a_l is positive. It is arranged symmetrically with the upper limit a_u around the central value a_k, enclosing an area (1 - γ) = 0.95 for 95% confidence level as shown in figure 4.1. The upper limit a_u fulfilling this requirement can be determined by calculating the p-quantile a_p of the p-value, which is defined as the cumulative probability of a normalized Gaussian PDF, $g^0(a) \equiv g^0(a, a_0 = 0, \sigma = 1)$ and $p = \int_{-\infty}^{a_p} g^0(a)da$ satisfying the equation:

$$0.95 = 1 - \gamma = 1 - p. \tag{4.7}$$

p is the area up to a_u and $(1 - p)$ is the area left for a_l. This equation reveals that $p = 0.975$ for 95% C.L. The corresponding quantile, a_p can be obtained from the statistical tables. For $p = 0.975$ it is $a_{p=0.975} = 1.96$. A peak detection can be claimed when the lower limit a_l is positive verifying that the confidence interval is double sided and more than 95% of $g(a)$ is in the positive range. This means, the condition given in equation (4.8) is fulfilled and specific activities and their errors can be provided via equation (4.6).

$$a_l = a_k - a_p \cdot \Delta a_k > 0 \tag{4.8}$$

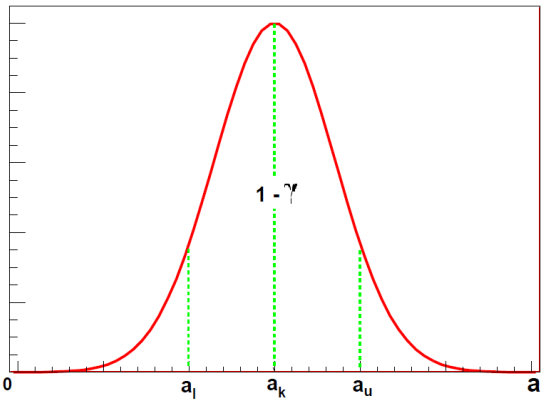

Figure 4.1: Illustration of a double sided confidence interval for 95% confidence level.

If $a_l \leq 0$, a peak detection can not be claimed at 95% C.L and the confidence interval will be single sided. Thus upper limit a_u must be given. In order to maintain the 95% C.L. for the limit, the truncated PDF must be enclosed between 0 and a_u as it is shown in figure 4.2. The area, s, of the truncated Gaussian can be calculated via $s = \int_{-\infty}^{a_k/\Delta a_k} g^0(a)da$. The q -value corresponding a 95% coverage of the truncated

Gaussian is calculated using the condition:

$$q = 1 - 0.05 \cdot s, \tag{4.9}$$

and the corresponding q -quantile a_q can again be obtained from the statistical tables. The 95% C.L. is then given by

$$a_u = a_k + a_q \cdot \Delta a_k \tag{4.10}$$

The upper limit for the activity is calculated by replacing a_k in formula (4.6) with a_u.

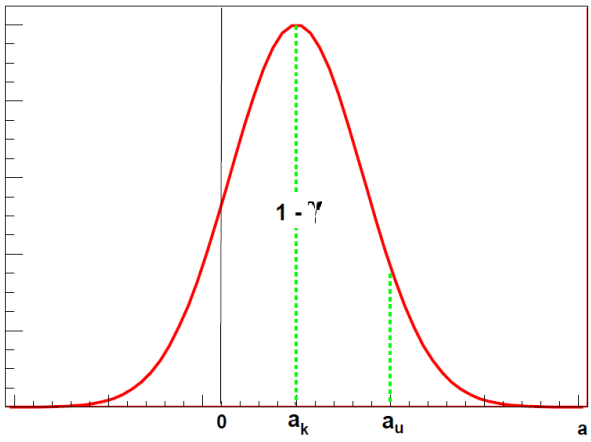

Figure 4.2: Illustration of a single sided confidence interval for 95% confidence level.

Figure 4.3 shows an example of stainless steel sample: The data shown in red is compared with the Monte Carlo sum spectrum (black solid). The individual radioactive contributions given by the best-fit are also shown. The measured background spectrum of Gator is shown as well.

The weight of sample is 6.6 kg and it was measured in Gator for 584150 seconds. The number of simulated events for ^{238}U decay is $1{\times}10^6$. The scaling factor obtained for this decay from the χ^2 minimization method is $a_k \pm \Delta a_k = 0.0159 \pm 0.0022$. The first step is to check if the condition given in equation (4.8) is fulfilled:

$$a_l = a_k - a_p \cdot \Delta a_k = 0.0159 - 1.96 \times 0.0022 > 0. \tag{4.11}$$

Thus, the confidence interval is double sided and a peak detection at 95% C.L. can be claimed. The activity and its error can be calculated by using the formula (4.6):

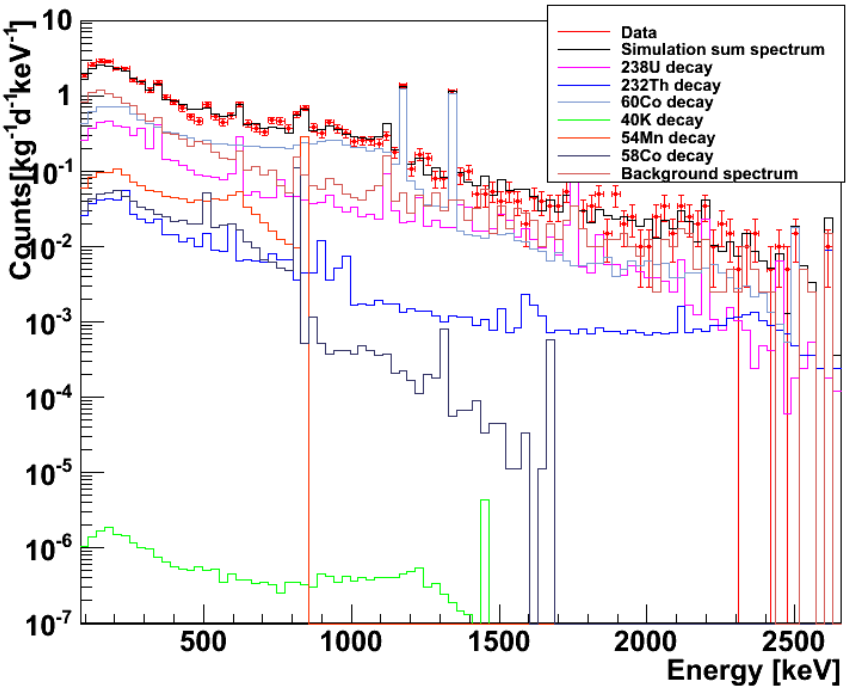

Figure 4.3: Best-fit of the Monte Carlo simulations to the Gator data for stainless steel sample. The data shown in red is compared with the Monte Carlo sum spectrum (black solid) and the individual contributions given by the best-fit (^{238}U (magenta), ^{232}Th (blue), ^{58}Co (grey), ^{60}Co (light blue), ^{54}Mn (orange), ^{40}K (green), background spectrum (brown)). The fit was performed between 100 and 2700 keV in order not to include the noise in the data.

$$\begin{aligned} A_k[Bq/kg] &= \frac{n_{sim} \cdot a_k}{m \cdot t} \pm \frac{n_{sim} \cdot \Delta_{a_k}}{m \cdot t} \\ &= \frac{1 \times 10^6 \cdot 0.0159}{6.6 \cdot 584158} \pm \frac{1 \times 10^6 \cdot 0.0022}{6.6 \cdot 584158} \\ &= 4.12 \times 10^{-3} \pm 5.7 \times 10^{-4} Bq/kg \end{aligned} \tag{4.12}$$

1×10^6 events were simulated for the decay of ^{40}K within the stainless steel sample. The simulation was first fitted to the data without applying any boundary for the range of scaling. Since, there is no clear indication about ^{40}K contamination in the data, a negative scaling factor was obtained in the first attempt. The fit was repeated by

applying a boundary to keep the scaling factor and minimum of χ^2 for ^{40}K in a positive range. The scaling factor results from the fit by the use of a boundary for this isotope is $a_k \pm \Delta a_k = 1.022 \times 10^{-5} \pm 9.14 \times 10^{-3}$. Since $a_k = 1.022 \times 10^{-5} \sim 0$,

$$a_l = a_k - a_p \cdot \Delta a_k = 0 - 1.96 \times 9.14 \times 10^{-3} < 0. \tag{4.13}$$

In this case the confidence interval will be single sided and only an upper limit can be provided for the activity of ^{40}K. The central value of the PDF is then $a_k \sim 0$ and the area under the truncated Gaussian will be:

$$s = \int_{-\infty}^{0} g(a)da = 0.5, \tag{4.14}$$

resulting the q value

$$q = 1 - 0.05 \cdot s = 1 - 0.05 \cdot 0.5 = 0.975. \tag{4.15}$$

The case $q = 0.975$ is only valid if $a_k = 0$. The quantile a_q corresponding to q=0.975 can be obtained from the statistical tables as $a_{q=0.975} = 1.96$. An upper limit for the 95 % C.L. is then calculated by:

$$a_u = a_k + a_q \cdot \Delta a_k = 0 + 1.96 \cdot 9.14 \times 10^{-3} = 0.0179. \tag{4.16}$$

The resulting upper limit for the activity of ^{40}K is therefore:

$$A_k[Bq/kg] < \frac{n_{sim} \cdot a_k}{m \cdot t} = \frac{1 \times 10^6 \cdot 0.0179}{6.6 \cdot 584158} = 4.64 \times 10^{-3} Bq/kg \tag{4.17}$$

Chapter 5

The Gator Background

According to the equation (4.2), the detection limit, L_D, strongly depends on the background. Hence, the knowledge of background is important to improve L_D and make it feasible the detection of low activities with higher precision within a given sample. Prior to its installation at LNGS, Gator had been operated in the Soudan underground laboratory in northern Minnesota, within the Solo facility [66]. At the Soudan lab, the detector has been used for the screening of XENON10 materials and several background runs were acquired [67]. The integral counting rate of the detector has decreased from (0.842 ± 0.005) counts/min at Soudan to (0.157 ± 0.001) counts/min at LNGS, in the 100-2700 keV energy region. This considerable decrease is mainly because of the improved shield and radon protection system. The background of Gator is investigated periodically in order to see the contribution of primordial (^{238}U, ^{232}Th, ^{40}K) and cosmogenic (^{65}Zn, ^{54}Mn, ^{60}Co, ^{58}Co) radionuclides. Furthermore, the contribution of ^{210}Pb within the innermost lead layer and ^{222}Rn within the sample cavity was studied.

Decays of primordial radionuclides were simulated within the innermost copper layer and within the cryostat of Gator. Decays of cosmogenics were simulated within the copper layer, cryostat and the Ge crystal. These simulations were then fitted to the measured background data using the χ^2 minimization method and the activitiy of each radionuclide was calculated by using the scale factors from the fit.

In this section we first give the details on the background sources of Gator. After that, the results of three dedicated background runs taken between 2007 and 2010 at LNGS facility are presented and a compared to the background taken in Soudan.

5.1 Background sources

According to their origin, Gator's background can be divided into two main groups: primordial and cosmogenic. This section summarizes the details of these sources.

5.1.1 Primordial background sources

The Big Bang Nucleosynthesis (BBN) produced mainly hydrogen and helium with a very little amount of lighter elements [68] [5]. Thus the first stars were made of hydrogen and helium. At the end of their life, most of the heavy stars became a Supernova which consists of an iron core surrounded by various layers of materials. Supernovae are a source of neutrons [69] which makes the production of heavier nuclides feasible. These primordial radionuclides are typically long lived, with half-lives on the order of hundreds of millions of years. The most common primordial radionuclides are ^{40}K , ^{238}U and ^{232}Th.

^{238}U: is the most common isotope of uranium with an isotopic abundance of 99.28%. ^{238}U is a α emitter with a half life of 4.46×10^{9} years. Figure 5.1 shows the decay chain of ^{238}U [70].

^{232}Th: ^{232}Th has an isotopic abundance of >99% in nature. It decays by α emission to ^{228}Ra with half life 1.39×10^{10} years. ^{232}Th is present in soils and materials and in secular equilibrium with ^{228}Ra because the half-life of ^{232}Th is much longer than any other radionuclide in the decay chain. Figure 5.2 shows the decay chain of ^{232}Th [70].

^{40}K: is a β unstable element with an isotopic abundance of 0.012%. It decays by β^{-} emission to ^{40}Ca with 89.23% probability, by electron capture to the 1460 keV level of ^{40}Ar with 10.55% probability. Half life of ^{40}K is 1.27×10^{9} years. Figure 5.3 shows the decay scheme of ^{40}K.

Refining processes used to produce oxygen-free high conductivity copper significantly reduces the amount of primordial radioimpurities. The massive parts of Gator shield and the cryostat made of copper. Thus, in order to investigate the contribution of these radionuclides to the Gator background, simulations were done within the copper shield and the cryostat of Gator and simulations were fitted to the background data.

5.1.2 Cosmogenic contribution to background

Spallation reactions are the main reason for the cosmogenic production of the isotopes. Interaction with high energy cosmic rays results in the disintegration of the involved nuclei into their constituents. Light nuclei and elementary particles or nucleons are emitted due to the interaction and results in a potentially radioactive nucleus with smaller atomic number. At the Earth's surface, neutrons have a significant contribution in the nuclide production compared to the higher altitudes where protons can also have a contribution in the nuclide production. The production rate R of an isotope with decay constant λ by the exposure to a flux ϕ of cosmic rays can be evaluated as [71]:

$$R \propto \int \sigma(E)\phi(E)dE, \tag{5.1}$$

where σ is the production cross-section and E is the particle energy.

Uranium^{238} Decay Chain (Radium Series)

The 4n+2 chain of U-238 is commonly called the "Radium Series" (sometimes "Uranium Series").

Nuclide	Element Name	Historic Name	Decay Mode	Half Life	MeV	Product of Decay
$_{92}U^{238}$	Uranium - 238	*Uranium*	α	4.471 x 10^9 yrs	4.26975	$_{90}Th^{234}$
$_{90}Th^{234}$	Thorium - 234	*Uranium X1*	β^-	24.07 d	0.27309	$_{91}Pa^{234}$
$_{91}Pa^{234}$	Protactinium - 234	*Uranium Z*	β^-	6.67 h	2.194577	$_{92}U^{234}$
$_{92}U^{234}$	Uranium - 234	*Uranium two*	α	245,660 yrs	4.85773	$_{90}Th^{230}$
$_{90}Th^{230}$	Thorium - 230	*Ionium*	α	75,438 yrs	4.76996	$_{88}Ra^{226}$
$_{88}Ra^{226}$	Radium - 226	*Radium*	α	1,590 yrs	4.87062	$_{86}Rn^{222}$
$_{86}Rn^{222}$	Radon - 222	*Radon*	α	3.823495 d	5.59031	$_{84}Po^{218}$
$_{84}Po^{218}$	Polonium - 218	*Radium A*	α 99.98 % β^- 0.02 %	3.167 min	6.11468 0.2596	$_{82}Pb^{214}$ $_{85}At^{218}$
$_{85}At^{218}$	Astatine - 218	*Eka-Iodine, Dakin*	α 99.90 % β^- 0.10 %	1.5 s	6.874 2.8812	$_{83}Bi^{214}$ $_{86}Rn^{218}$
$_{86}Rn^{218}$	Radon - 218	*Actinon*	α	35 msec	7.26253	$_{84}Po^{214}$
$_{82}Pb^{214}$	Lead - 214	*Radium B*	β^-	26.833 min	1.0189	$_{83}Bi^{214}$
$_{83}Bi^{214}$	Bismuth - 214	*Radium C*	β^- 99.976 % α 0.021 % $\beta^-\alpha$ 0.003 %	19.833 min	3.2697 5.62119 11.1032	$_{84}Po^{214}$ $_{81}Tl^{210}$ $_{82}Pb^{210}$
$_{84}Po^{214}$	Polonium - 214	*Radium C'*	α	164.3 µsec	7.83346	$_{82}Pb^{210}$
$_{81}Tl^{210}$	Thallium - 210	*Radium C"*	β^- ~ 100%	1.30 min	5.482	$_{82}Pb^{210}$
$_{82}Pb^{210}$	Lead - 210	*Radium D*	β^- ~ 100% α 1.9×10^{-6} %	22.23 yrs	0.06486 3.7923	$_{83}Bi^{210}$ $_{80}Hg^{206}$
$_{83}Bi^{210}$	Bismuth - 210	*Radium E*	β^- 99.999878% α 0.000132%	5.012 d	1.161292 5.0364	$_{84}Po^{210}$ $_{81}Tl^{206}$
$_{84}Po^{210}$	Polonium - 210	*Radium F*	α	138.3762 d	5.40745	$_{82}Pb^{206}$
$_{80}Hg^{206}$	Mercury - 206		β^-	8.15 min	1.3076	$_{81}Tl^{206}$
$_{81}Tl^{206}$	Thallium - 206		β^-	4.167 min	1.532346	$_{82}Pb^{206}$
$_{82}Pb^{206}$	Lead - 206		-	stable	-	-

Figure 5.1: Decay chain of ^{238}U [70]

Thorium^{232} Decay Chain (Thorium Series)

The 4n+2 chain of Th^{235} is commonly called the "Thorium Series". This table shows the naturally occurring elements in this series.

Nuclide	Element Name	Historic Name	Decay Mode	Half Life	MeV	Product of Decay
$_{90}Th^{232}$	Thorium - 232	*Thorium*	α	1.406 x 10^{10} yrs	4.0816	$_{88}Ra^{228}$
$_{88}Ra^{228}$	Radium - 228	*Mesothorium 1*	β^-	5.739 yrs	0.045811	$_{89}Ac^{228}$
$_{89}Ac^{228}$	Actinium - 228	*Mesothorium 2*	β^-	6.139 hrs	2.12379	$_{90}Th^{228}$
$_{90}Th^{228}$	Thorium - 228	*Radiothorium*	α	1.91286 yrs	5.52008	$_{88}Ra^{224}$
$_{88}Ra^{224}$	Radium - 224	*Thorium X*	α	3.657 yrs	5.78885	$_{86}Rn^{220}$
$_{86}Rn^{220}$	Radon - 220	*Thoron*	α	0.9267 min	7.52626 0.71484	$_{84}Po^{216}$
$_{84}Po^{216}$	Polonium - 216	*Thoium A*	α	145 msec	6.90632	$_{82}Pb^{212}$
$_{82}Pb^{212}$	Lead - 212	*Thorium B*	β^-	10.64 hrs	0.56991	$_{83}Bi^{212}$
$_{83}Bi^{212}$	Bismuth - 212	*Thorium C*	β^- 64.06% α 35.94% β^- α 0.014%	61 min	2.25213 6.20726 11.20624	$_{84}Po^{212}$ $_{81}Tl^{208}$ $_{82}Pb^{208}$
$_{84}Po^{212}$	Polonium - 212	*Thorium C'*	α	299 nsec	8.95412	$_{82}Pb^{208}$
$_{81}Tl^{208}$	Thallium - 208	*Thorium C''*	β^-	3.0533 min	4.99898	$_{82}Pb^{208}$
$_{82}Pb^{208}$	Lead - 208		—	Stable	—	—

Figure 5.2: Decay chain of ^{232}Th [70].

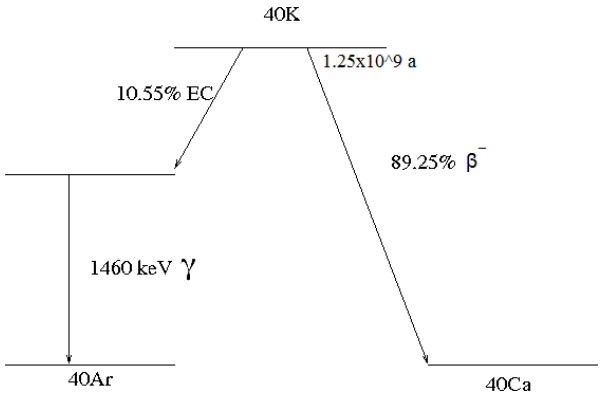

Figure 5.3: Decay scheme of ^{40}K.

During its water and ground based transportation from Soudan to LNGS, Gator and its cryostat has been exposed to the cosmic rays for several months at the Earth's surface. The copper plates used to construct the innermost layer of the shield have been exposed to the cosmic rays during the production as well. Copper is the most massive part which directly surrounds the Ge crystal and as a consequence of the spallation reaction, 4 nucleons up to the 18 nucleons are emitted after the interaction of neutrons or protons with ^{63}Cu or ^{65}Cu [73]. Activities of cosmogenic radionuclides ^{65}Zn, ^{54}Mn, ^{60}Co, ^{58}Co were thus investigated within the context of the background study. Table 5.1 summarizes some characteristics of the above mentioned cosmogenic isotopes. The cosmogenic activation increases the background counting rate of Gator. Half life of most of these cosmogenics are less than a year. Only ^{60}Co has a half life more than 5 years. Figure 5.4 and figure 5.5 shows the decay scheme of ^{65}Zn, ^{58}Co, ^{60}Co, ^{54}Mn respectively.

Isotope	**Reaction channel**	**Half life**
^{65}**Zn**	^{64}Zn(n,γ)^{65}Zn or ^{65}Cu(p,n)^{65}Zn	224.26 days
^{54}**Mn**	^{54}Fe(n,p)^{54}Mn or ^{53}Cr(d,n)^{54}Mn	312.3 days
^{60}**Co**	^{59}Co(n,γ)^{60}Co	5.27 years
^{58}**Co**	^{58}Ni(n,p)^{58}Co or ^{55}Mn(α,n)^{58}Co ^{59}Co(n,2n)^{58}Co	70.8 days

Table 5.1: Properties of the cosmogenic radioisotopes analyzed as a background source for Gator.

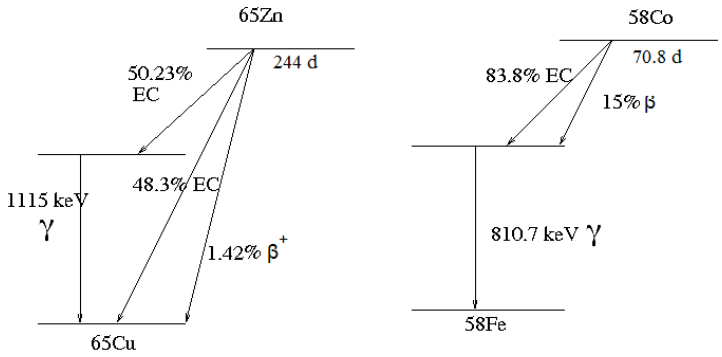

Figure 5.4: Decay scheme of ^{65}Zn (left) and ^{58}Co (right) . ^{65}Zn decays by electron capture to the 1115 keV excited level and by electron capture and and β^+ emission to the ground state level of ^{65}Cu. ^{58}Co decays to the excited states of ^{58}Fe by electron capture or by β^+ emission

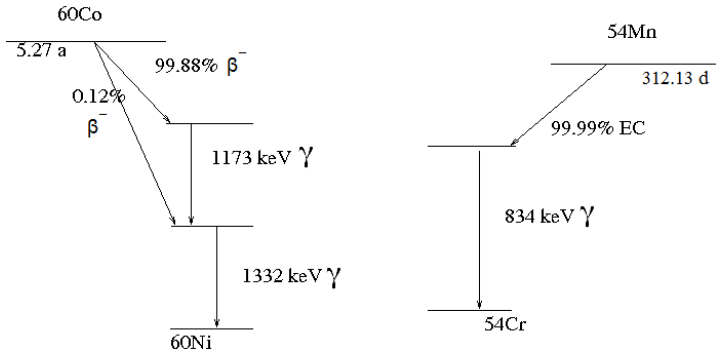

Figure 5.5: Decay scheme of ^{60}Co (left) and ^{54}Mn (right). ^{60}Co decays by β emission to the excited leveles of ^{60}Ni. ^{54}Mn decays by electron capture to the 835 keV level of ^{54}Cr

5.2 Background analysis

This section gives the details about the three different background runs taken between 2007 and 2010 at LNGS underground laboratory.

5.2.1 Background at LNGS

Background taken in 2007: The first background of Gator at LNGS was taken right after its installation in September 2007. The measurement took 14.9 days. Figure 5.2 shows the spectrum for this run. The integral background counting rate between 100 keV and 2700 keV for this run is (0.258 ± 0.003) events/min. Table 5.2 gives the count rates under the significant peaks in the data spectrum. The count rates under each peak were calculated by fitting a gaussian to each peak and integrating the number of bins between mean ± 3σ region. The Compton background was subtracted from each peak by taking the integral of 6 bins before and after the peak in question and by taking the average of the two integrals.

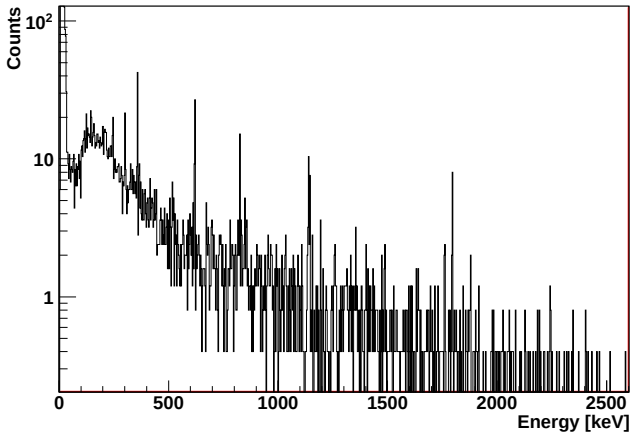

Figure 5.6: Acquired background spectrum in September 2007.

In order to find the specific activities of each radionuclide, as previously mentioned, decays of ^{238}U, ^{232}Th, ^{40}K, ^{65}Zn, ^{54}Mn, ^{60}Co, ^{58}Co were simulated within the copper shields and the cryostat of the detector. Decays of cosmogenics were simulated within the Ge crystal, and decays of ^{210}Pb and ^{222}Rn were simulated within the innermost lead layer and the sample cavity, respectively. The simulations were fit to the data spectrum by using the χ^2 minimization method and activities for each radionuclide were calculated. Table 5.3 shows the results obtained for the activities of each radionuclides. Figure 5.7 shows a comparison of the sum of the simulated spectra from natural and cosmogenic

Energy [keV]	**Chain/nuclide**	**Peak integral background rate [counts/day]**
239	^{232}Th/^{212}Pb	0.7 ± 0.1
911	^{232}Th/^{228}Ac	0.4 ± 0.2
352	^{238}U/^{214}Pb	4.3 ± 0.7
609	^{238}U/^{214}Bi	4.0 ± 0.5
1120	^{238}U/^{214}Bi	2.7 ± 0.4
1765	^{238}U/^{214}Bi	1.5 ± 0.3
662	^{137}Cs	0.5 ± 0.3
1173	^{60}Co	0.5 ± 0.2
1332	^{60}Co	0.6 ± 0.2
1461	^{40}K	0.5 ± 0.2

Table 5.2: Background counting rates (in events/day) in the $\pm 3\sigma$-regions for the main primordial and the gamma lines of ^{137}Cs, ^{60}Co and ^{40}K.

radionuclides in the detector and shield materials (black) with the observed background spectrum (red data points). Figure 5.8 shows the individual, best-fit contributions to the observed spectrum: natural radioactivity in Cu (blue), cosmogenic radio-nuclides in Ge and Cu (green), ^{222}Rn decays inside the shield (magenta) and ^{210}Pb decays in the Pb shield (yellow).

Isotope/chain	**Copper shield**	**Cryostat**	**Ge-crystal**	**Sample chamber**
^{238}U (μBq/kg)	63±12	5.5±2		
^{232}Th (μBq/kg)	27±8	5±2		
^{60}Co (μBq/kg)	4±2	1.5±0.5	< 1.4	-
^{40}K (μBq/kg)	37±5	15±3.5	< 1.5	
^{65}Zn (μBq/kg)	< 1.2	2±0.6	<0.8	
^{54}Mn (μBq/kg)	3.7±1.5	8±3	4.8±1.3	
^{58}Co (μBq/kg)	14±4	15±3.5	8±3	
^{222}Rn (mBq/m^3)				3±1

Table 5.3: Activities of the radionuclides calculated for the background run taken in semptember 2007

The activity results obtained in this study indicates that the background of Gator is comparable to the one of the world's most sensitive germanium detector (GeMPI) [18] [72]. A detailed background comparison to this detector is given in the last section. The half life of the cosmogenic radionuclides investigated in this study is less than a year

except for ^{60}Co and thus a significant reduction in the background counting rates and in the activities of these cosmogenics can be expected in one year.

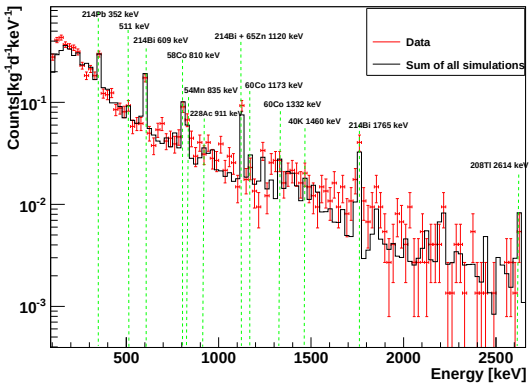

Figure 5.7: Comparison of the sum of the simulated spectra from natural and cosmogenic radionuclides in the detector and shield materials (black) with the observed background spectrum (red data points). The spectrum shows the energy range over which the fit was performed.

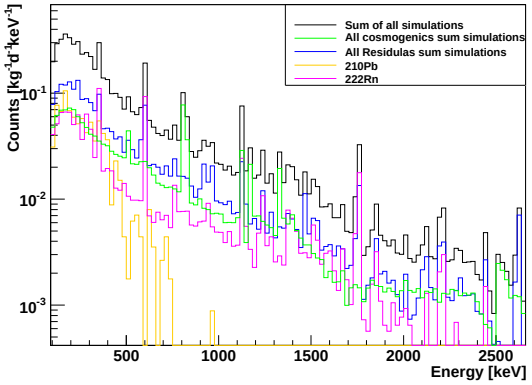

Figure 5.8: The individual, best-fit contributions to the observed spectrum are shown: natural radioactivity in Cu (blue), cosmogenic radionuclides in Ge and Cu (green), ^{222}Rn decays inside the shield (magenta) and ^{210}Pb decays in the Pb shield (yellow).

Background taken in 2008:

A second background run was acquired for 22.5 days in October 2008. The integral background counting rate between 100 and 2700 keV is found to be (0.186 ± 0.003) events/min. This significant reduction in the integral background counting rate compared to the background taken in 2007 (0.258 ± 0.003 events/min) is due to the improvement in the radon suppression system and due to the decay of most cosmogenic radionuclides. Figure 5.9 compares the background spectrum taken in 2008 (red) to the background spectrum from 2007 (black). Table 5.4 shows the count rates under some significant peaks in the data spectrum.

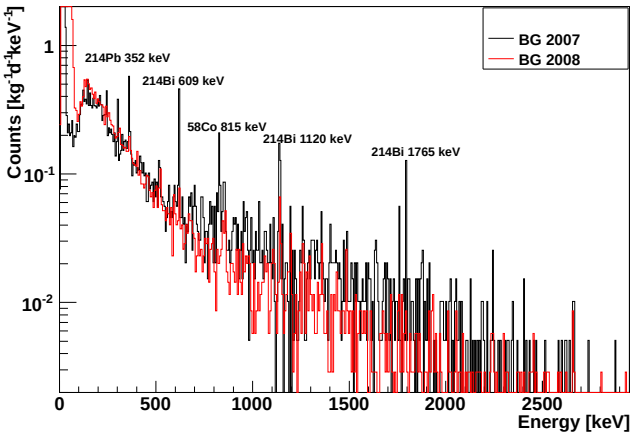

Figure 5.9: Comparison of background spectra from 2007 (black) and 2008 (red). A significant reduction in the background due to the improved radon suppression system is clearly visible.

Monte Carlo simulations were fitted again to the background data in the same way as in 2007 by attempting to minimize the χ^2 value. Figure 5.10 shows comparison of the sum of the simulated spectra from natural and cosmogenic radionuclides in the detector and shield materials (black) with the observed background spectrum (red data points). Figure 5.11 shows the individual, best-fit contributions to the observed spectrum are shown: natural radioactivity in Cu (blue), cosmogenic radio-nuclides in Ge and Cu (green), ^{222}Rn decays inside the shield (magenta) and ^{210}Pb decays in the Pb shield (yellow). Activities obtained in this background study are represented in Table 5.5

Energy [keV]	**Chain/nuclide**	**Peak integral background rate [counts/day]**
239	^{232}Th/^{212}Pb	0.13± 0.08
911	^{232}Th/^{228}Ac	0.4± 0.1
352	^{238}U/^{214}Pb	1.1 ± 0.2
609	^{238}U/^{214}Bi	1.1± 0.2
1120	^{238}U/^{214}Bi	1.3 ± 0.2
1765	^{238}U/^{214}Bi	0.2 ± 0.1
662	^{137}Cs	< 0.5
1173	^{60}Co	0.5 ± 0.2
1332	^{60}Co	0.5 ± 0.1
1461	^{40}K	0.4 ± 0.1

Table 5.4: Background counting rates (in events/day) in the $\pm 3\sigma$-regions for the main primordial and the gamma lines of ^{137}Cs, ^{60}Co and ^{40}K for the background taken in 2008.

Isotope/chain	**Copper shield**	**Cryostat**	**Ge-crystal**	**Sample chamber**
^{238}U (μBq/kg)	68±11	8±4		
^{232}Th (μBq/kg)	18±7	6±3		
^{60}Co (μBq/kg)	7±3	1.8±0.5	<1	-
^{40}K (μBq/kg)	26±8	14±6	<1.9	
^{65}Zn (μBq/kg)	<0.9	2.4±1	<0.8	
^{54}Mn (μBq/kg)	2.8±1.1	5.5±1.8	4±1	
^{58}Co (μBq/kg)	<1.0	1.5±0.6	2.2±0.8	
^{222}Rn (mBq/kg)				1 ±0.4

Table 5.5: Activities of the radionuclides calculated for the background run taken in october 2008

As it can be seen from Figure 5.9, the ^{214}Bi lines arising from ^{222}Rn decay were significantly reduced. This indicates the improvement in the radon suppression system. Activities of the cosmogenics radionuclides with short half life such as ^{58}Co and ^{54}Mn are also smaller than the previous background run.

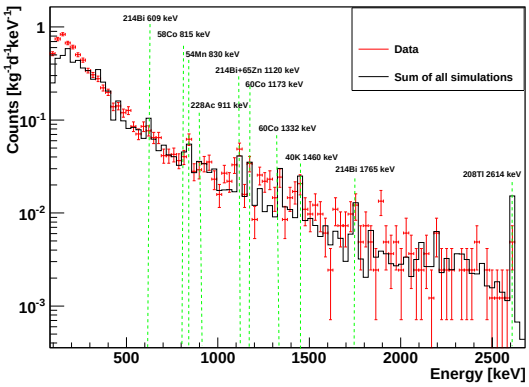

Figure 5.10: Comparison of the sum of the simulated spectra from natural and cosmogenic radionuclides in the detector and shield materials (black) with the observed background spectrum (red data points) for the background run taken in 2008.

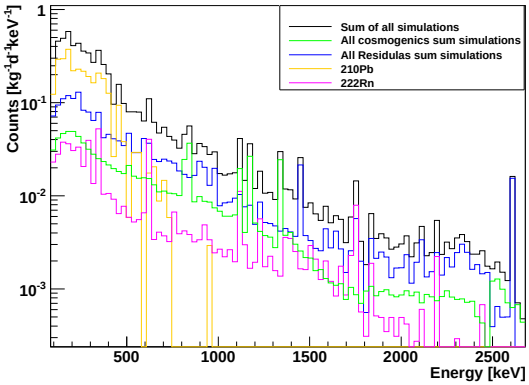

Figure 5.11: The individual, best-fit contributions to the observed spectrum are shown: natural radioactivity in Cu (blue), cosmogenic radio-nuclides in Ge and Cu (green), ^{222}Rn decays inside the shield (magenta) and ^{210}Pb decays in the Pb shield (yellow).

Background taken in 2010: A third background run of Gator was acquired between February and April 2010. Before this measurement, the Gator shield was improved. The glove box of the shield was removed from its place and the sample cavity were cleaned with ethanol to remove the dirt possibly left after long term operation. Sealing of the shield was also improved by using silicon. Thus diffusing of radon into the shield was significantly minimized. The background was acquired for 51.4 days to increase the statistic in the data. Simulations which were described previously were

then again fitted to the acquired data in order to obtain the activities after the shield improvement. Figure 5.12 compares the data spectrum obtained for this background run to the previous two background runs. Integral background counting rates between 100 and 2700 keV for this run found as 0.157 ± 0.001 events/min which is again significantly less than the counting rates in 2007 (0.258 ± 0.003 events/min) and 2008 (0.186 ± 0.003) events/min. The background counting rate in 2010 and the values represented in Table 5.6 indicates the effect of shield improvement on the background counting rates.

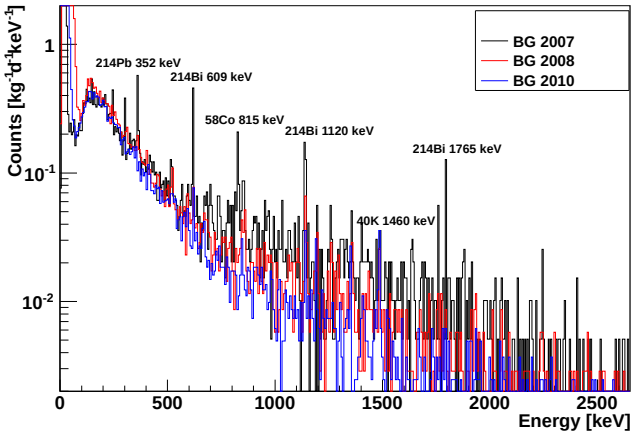

Figure 5.12: Comparison of the background spectra from 2007 (black), 2008 (red) and 2010 (blue).

Table 5.7 shows the results obtained for the activities of each radionuclides. Figure 5.13 shows a comparison of the sum of the simulated spectra to the observed background spectrum (red data points). Figure 5.14 shows the individual, best-fit contributions to the observed spectrum.

Energy [keV]	**Chain/nuclide**	**Peak integral background rate [counts/day]**
239	^{232}Th/^{212}Pb	< 0.5
911	^{232}Th/^{228}Ac	< 0.5
352	^{238}U/^{214}Pb	0.7 ± 0.3
609	^{238}U/^{214}Bi	0.6 ± 0.2
1120	^{238}U/^{214}Bi	0.3 ± 0.1
1765	^{238}U/^{214}Bi	0.08 ± 0.06
662	^{137}Cs	0.3 ± 0.1
1173	^{60}Co	0.5 ± 0.1
1332	^{60}Co	0.5 ± 0.1
1461	^{40}K	0.5 ± 0.1

Table 5.6: Background counting rates (in events/day) in the $\pm 3\sigma$-regions for the main primordial and the gamma lines of ^{137}Cs, ^{60}Co and ^{40}K.

Isotope/chain	**Copper shield**	**Cryostat**	**Ge-crystal**	**Sample chamber**
^{238}U (μBq/kg)	56±11	8±5		
^{232}Th (μBq/kg)	27±7	4±2		
^{60}Co (μBq/kg)	8±4	1.3±0.4	<0.80	-
^{40}K (μBq/kg)	32±13	11±6	<1.30	
^{65}Zn (μBq/kg)	<0.16	<0.50	<0.15	
^{54}Mn (μBq/kg)	<1.3	<2.15	<1.60	
^{58}Co (μBq/kg)	<27	<0.22	<0.11	
^{222}Rn (μBq/kg)				<55

Table 5.7: Activities of the radionuclides calculated for the background run taken in 2010

The background runs of Gator reveals that the most significant contribution to the background comes from the natural radioactive decay chains of ^{238}U, ^{232}Th,^{40}K within the innermost copper layer and cryostat of Gator. Innermost lead layer has a contribution of ^{210}Pb around 4 ± 1 Bq/kg and this value is consistent with the value given by the company. In the last background run it was also seen that most of the cosmogenics are decayed and the improvements made in the shield of Gator was successful.

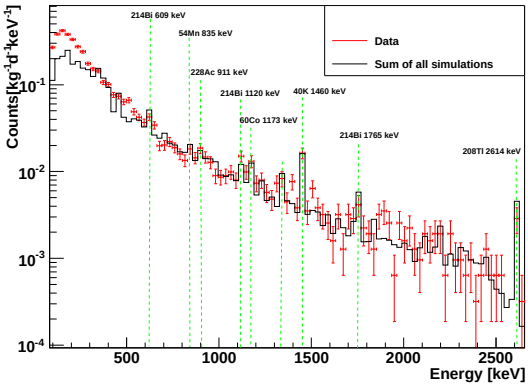

Figure 5.13: Comparison of the sum of the simulated spectra from natural and cosmogenic radionuclides in the detector and shield materials (black) with the observed background spectrum (red data points). The difference between data and Monte Carlo simulations below 300 keV is due to the thickness of the copper endcap which was slightly thicker in the Monte Carlo geometry.

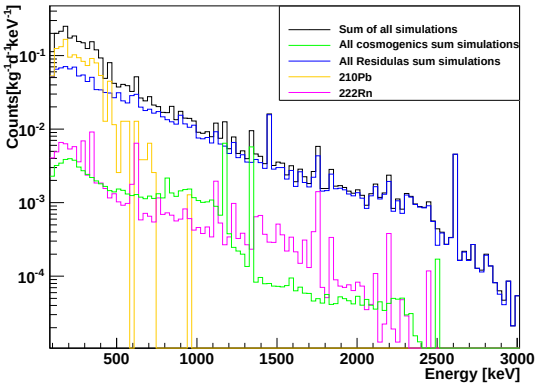

Figure 5.14: The individual, best-fit contributions to the observed spectrum are shown: natural radioactivity in Cu (blue), cosmogenic radionuclides in Ge and Cu (green), ^{222}Rn decays inside the shield (magenta) and ^{210}Pb decays in the Pb shield (yellow).

5.2.2 Comparison of Gator background in Soudan and to GeMPI

As it was previously mentioned, Gator was first operated in the Soudan underground laboratory within the XENON10 project. Several background runs were acquired in this location [67]. Another high purity germanium detector installed at LNGS under-

ground counting facilitiy, named as GeMPI [18], and operated mainly in the context of solar neutrino experiment, BOREXINO [74], which requires an extreme low background detector and shield materials, as in case of XENON100. The shield set up of Gator was insipired from GeMPI detector. GeMPI is the one of the world's most sensitive detector with a large sample capacitiy ($25\times25\times33$ cm^3) [18] like Gator. The integral background counting rate of GeMPI in the energy range from 50 to 2750 keV is about 0.15 min^{-1} [18].

Figure 5.15 (top) shows the comparison between the latest background spectrum acquired at LNGS (2010), a spectrum taken in the SOLO facility at Soudan (2007) and the background of the GeMPI detector [18]. It also shows (bottom) the Gator spectrum underground at LNGS prior to its installation in the shield, inside the shield, and inside the shield with the radon protection system on. The background decrease is more than four orders of magnitude, and shows that a careful shielding is needed even when the detector is operated deep underground [61].

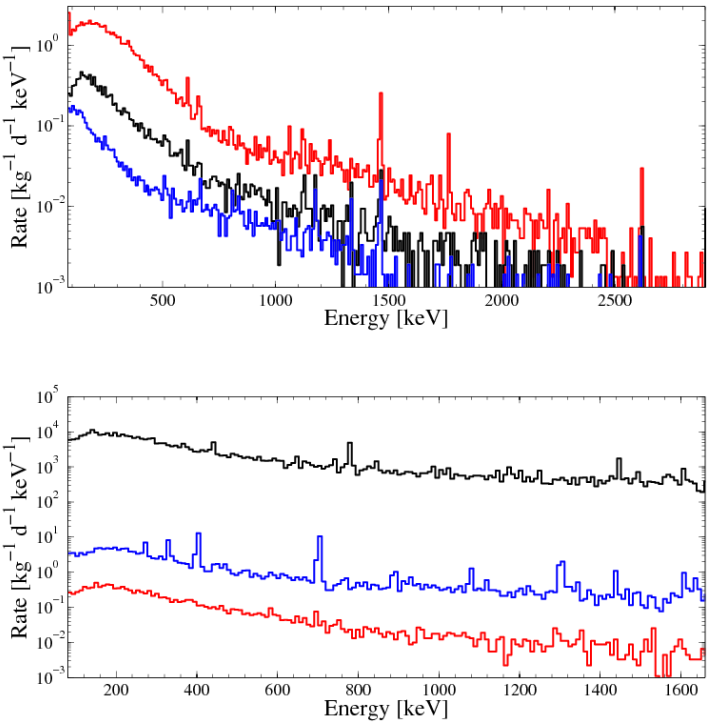

Figure 5.15: (Top) Background spectra of Gator at Soudan (red), at LNGS (black) and the spectrum of the GeMPI detector [18] (blue). (Bottom) Gator background spectrum at LNGS: outside the shield (black), inside the shield (blue) and inside the shield with the radon protection system on (red), clearly showing the suppression of the main gamma lines associated with radon decays [61].

Table 5.9 summarizes the integral background counting rates between 100 and 2700 keV for the three background runs taken at LNGS facility and compares the values to the counting rate in Solo facility.

Run	**Lifetime [days]**	**Rate [events/min]**
Gator at Soudan	22.96	0.842 ± 0.005
Gator at LNGS (09-2007)	14.90	0.258 ± 0.003
Gator at LNGS (10-2008)	22.59	0.186 ± 0.003
Gator at LNGS (04-2010)	51.43	0.157 ± 0.001

Table 5.9: Integral background counting rates for Gator as measured at Soudan and at LNGS in three different runs. The integral is evaluated in the energy range [100, 2700] keV.

Table 5.10 compares the background counting rates of Gator at LNGS facility to the background counting rates in Soudan to the counting rates of GeMPI. As it can be seen from figure 5.15 and the values given in table 5.9 and table 5.10, the background is comparable to the background of GeMPI.

Table 5.10: Comparison of the background counting rates of Gator taken at LNGS to the background counting rates of Gator in Soudan and to the GeMPI detector.

Energy [keV]	Chain/nuclide	Peak integral background rate [counts/day]				
		Gator (Soudan)	Gator (LNGS, 09-2007)	Gator (LNGS, 10-2008)	Gator (LNGS, 04-2010)	GeMPI [18]
239	^{232}Th/^{212}Pb	1.1 ± 0.7	0.7 ± 0.1	0.13 ± 0.08	<0.5	NA
911	^{232}Th/^{228}Ac	0.9 ± 0.3	0.4 ± 0.2	0.4 ± 0.1	<0.5	<0.2
352	^{238}U/^{214}Pb	4.9 ± 0.7	4.3 ± 0.7	1.1 ± 0.2	0.7±0.3	<0.5
609	^{238}U/^{214}Bi	4.5 ± 0.5	4.0 ± 0.5	1.1 ± 0.2	0.6±0.2	0.50±0.45
1120	^{238}U/^{214}Bi	1.6 ± 0.3	2.7 ± 0.4	1.3 ± 0.2	0.3 ±0.1	NA
1765	^{238}U/^{214}Bi	1.3 ± 0.2	1.5 ± 0.3	0.2 ± 0.1	0.08±0.06	NA
662	^{137}Cs	2.9 ± 0.4	0.5 ± 0.3	<0.5	0.3±0.1	NA
1173	^{60}Co	0.5 ± 0.1	0.5 ± 0.2	0.5 ± 0.2	0.5±0.1	0.6±0.4
1332	^{60}Co	0.6 ± 0.1	0.6 ± 0.2	0.5 ± 0.1	0.5 ±0.1	0.4±0.3
1461	^{40}K	5.8 ± 0.4	0.5 ± 0.2	0.4 ± 0.1	0.5 ±0.1	0.6±0.4

Chapter 6

Screening Results

The challenging task of the dark matter experiments is to design and construct a detector which has a background in a extraordinarly low level to observe the rare expected dark matter signals. Therefore, it is very important to screen all the candidate detector components to determine their contamination and select the radio-pure ones for the detector construction. Different detector materials and components used for the XENON100 detector construction were screened with the Gator facility and the results from the screening measurements were published [75].

For the data analysis 2 different methods were used. The details of the methods were given in chapter 4. This chapter gives the details of the screening results obtained by using the χ^2 method and compares the results from the analysis of most prominent peaks.

6.1 Photomultipliers

PMTs are the central part of the XENON100 and are placed very close to the target volume to read out and magnify the light signals arising from the particle interactions. Since PMTs also includes different kind of assembled materials and components, they are one of the dominant background sources and their activities are important.

6.1.1 Photomultiplier Hamamatsu R8520

In the XENON100 experiment conventional PMT, R8520, was used for the detection of photons. This PMT consists of a photocathode and dynodes set at different potential differences. The gain, which is the amount of output electrons for each single electron input of these PMT is approximately one million. Therefore it is a very suitable sensor to magnify a signal from a dark matter particle interaction. Figure 6.1 shows a picture

of this PMT.

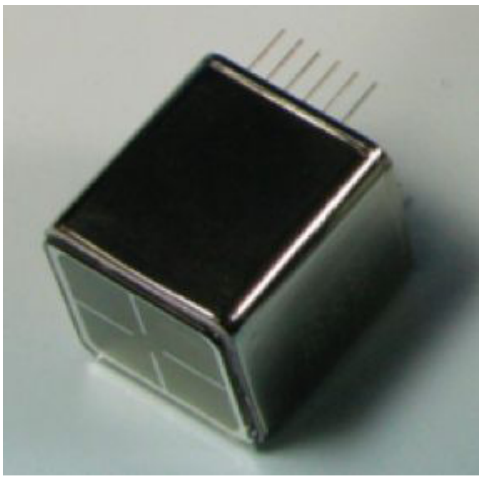

Figure 6.1: Picture of the Hamamatsu R8520 PMT used as photon sensor in the XENON100 experiment

Several R8520 photomultiplier batches were screened with Gator to check the systematics which arise from the slight difference in the production processes. The batches consisting of seven, eleven, twelve and twentytwo PMTs of the one inch square PMTs from Hamamatsu were screened for 9.5, 5.6, 9.3 and 5.5 days respectively. The PMTs in the first three batches were used in the bottom PMT array and the PMTs in the last batch were used in the veto PMT array of the XENON100 detector. For the screening, PMTs were placed on the detector's endcap.

Figure 6.2 shows the fit spectra for the above mentioned four batches. Top left plot shows the fit spectrum for the seven PMT screeing. Top right plot shows the fit spectrum for the eleven PMT, bottom left plot is the fit from the twelve PMT and bottom right is the fit spectrum from the twentytwo PMT screening. For all four batches, the data spectrum is mainly dominated by the ^{60}Co and ^{40}K contaminations.

Table 6.1 summarizes the calculated results from χ^2 minimization analysis and compares the results from γ-line analysis [62].

LNGS screening facility was also used for the screening of the other PMT batches and the results were published in [75]. Taking into account the possiblity of different production conditions might effect the intrinsic activity of the PMTs, they were grupped into the batches and screened seperately. PMTs shown in table 6.1 were used for the construction of XENON100. Some batches were eliminated because of their high intrinsic contamination and not fullfilling the requirements of XENON100. Details can be found in [75].

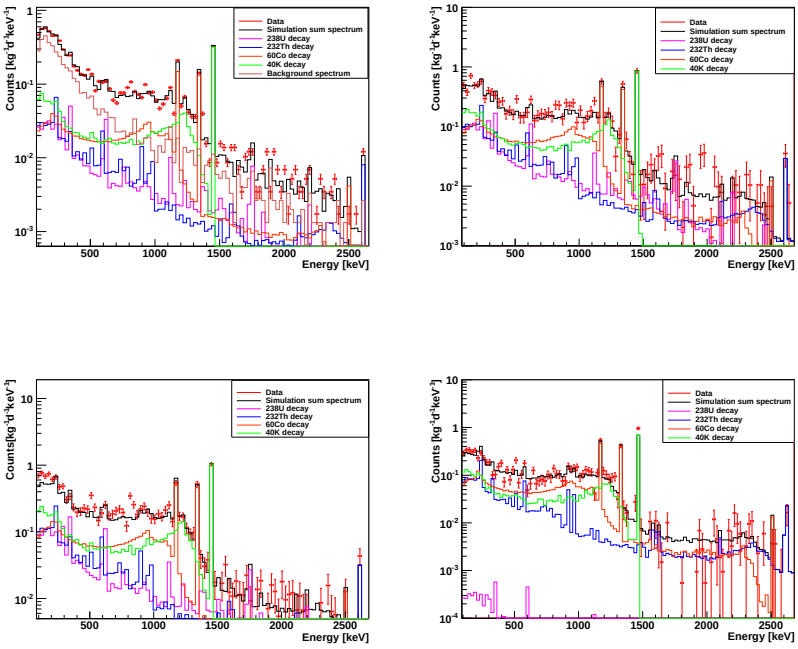

Figure 6.2: Fit of the simulations to the data from the seven PMT screening (top left), eleven PMT screenin (top right), twelve PMT screening (bottom left) and twentytwo PMT screening (bottom right). For the all four screening the data spectrum is dominated by the ^{60}Co and ^{40}K contaminations.

Material	**Method**	^{238}**U** (mBq/Pmt)	^{232}**Th** (mBq/Pmt)	^{60}**Co** (mBq/Pmt)	^{40}**K** (mBq/Pmt)
7 PMTs	χ^2 method	0.23±0.08	0.21±0.07	0.63±0.07	12.8±0.92
	γ-lines	0.2±0.12	<0.25	0.7±0.2	13.0±2.5
11 PMTs	χ^2 method	<0.88	0.27±0.08	0.7±0.16	12.8±2.2
	γ-lines	0.3±0.19	0.2± 0.13	0.8±0.19	12.0±2.5
12 PMTs	χ^2 method	0.29±0.06	0.27±0.1	0.71±0.09	14.5±1.2
	γ-lines	<0.13	0.13± 0.05	0.7±0.1	13±2.0
22 PMTs	χ^2 method	<0.1	0.20±0.09	0.57±0.04	8.4±0.9
	γ-lines	<0.2	0.18± 0.06	0.6±0.1	11.0±2

Table 6.1: Activities calculated for different PMT batches with the χ^2 analysis and comparison to the results from γ-line analysis [62]. ^{60}Co and ^{40}K contaminations are higher than ^{238}U, ^{232}Th for four PMT batches.

6.1.2 R11410-MOD

Hamamatsu R11410-MOD is a three inch large area PMT designed to work at very low temperatures $\sim$ 163 K. The quantum efficiency of this PMT is $\sim$ 26 % at 175 nm. Therefore it is a very suitable PMT for the experiments using liquid xenon to detect dark matter. The relatively high intrinsic radioactivity and therefore background from the PMTs with glass packages overcome by using metal package for Hamamatsu R11410-MOD. This PMT is going to be used as photosensors in the XENON1T to further lower the background contribution from the PMTs and increase the sensitivity of the experiment.

One R11410-MOD tube was screened for 20.4 days. Figure 6.4 shows the obtained fit spectrum. Table 6.2 represents the calculated results from χ^2 minimization analysis and comparison to the results from γ-line analysis.

Figure 6.3: Picture of the Hamamatsu R11410 PMT [76].

Method	^{238}**U** (**mBq/Pmt**)	^{226}**Ra** (**mBq/Pmt**)	^{232}**Th** (**mBq/Pmt**)	^{60}**Co** (**mBq/Pmt**)	^{40}**K** (**mBq/Pmt**)
χ^2 **method**	< 14.4	1.5±0.4	< 1.3	4.3±0.4	14.8±4.5
γ**-lines**	< 95	< 2.4	< 2.6	3.5±0.6	13.0±4.0

Table 6.2: Activities obtained for the R11410-MOD via the χ^2 analysis [62]

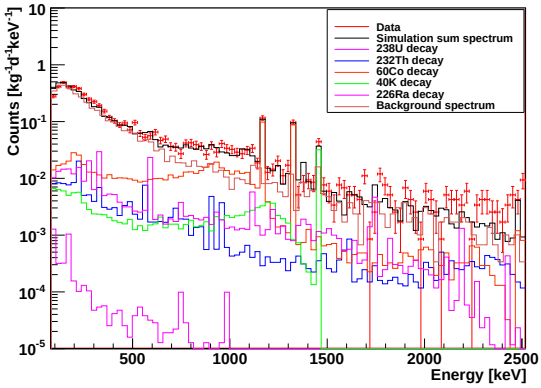

Figure 6.4: Fit of the simulations to the R11410-MOD data.

Isotope/chain	**R11410-MOD**	**R8520**
^{238}**U (mBq/cm^2)**	< 0.3	<0.2
^{232}**Th (mBq/cm^2)**	< 0.03	0.03 ± 0.01
^{60}**Co (mBq/cm^2)**	0.1 ± 0.009	0.1 ± 0.006
^{40}**K (mBq/cm^2)**	0.3 ± 0.1	1.3 ± 0.13

Table 6.3: Comparison of Gator screening results for Hamamatsu R11410-MOD to R8520. Activity values are normalized to photocathode area.

According to the results represented in table 6.3, R11410-MOD has already less total radioactivity (a drastic decrease in the activity of ^{40}K) compared to the total radioactivity of R8520. Therefore the use of this PMT in the XENON1T will significantly reduce the background arising from the PMTs.

6.1.3 QUPIDs

As it was previously mentioned, a majority of background comes from the PMTs because of facing the target volume directly. University of California Los Angeles collaborated with Hamamatsu to develop QUartz Photon Intensifying Detector (QUPID) [77] as a replacement for conventional PMTs which have relatively higher intrinsic contamination. The working principle of this PMT based on the Hybrid Avalanche Photo Diode (HAPD) [78]. Hit of the photons on the photocathode causes release of photoelectrons. Application of high voltage between photocathode and Avalanche Photo Diode (APD) accelerates them onto APD where electron and hole pairs are created thanks to high kinetic energy of photoelectrons. Finally, the elec- trons and holes are separated and

accelerated by the high bias voltage on the APD causing an avalanche effect. The quantum efficiency of the QUPID at room temperature is $> 30\%$ at 175 nm wavelength. Figure 6.5 shows a picture of QUPID.

Figure 6.5: Picture of a QUPID.

Five QUPIDs were screened for 49.5 days to obtain the activity values of this alternative PMT samples. They were placed on the Gator's end cap for the screening. Figure 6.6 shows the obtained fit spectrum and table 6.4 represents the calculated results from χ^2 minimization analysis and compares them to results from the γ-line analysis [62].

Method	^{238}**U** **(mBq/Pmt)**	^{232}**Th** **(mBq/Pmt)**	^{60}**Co** **(mBq/Pmt)**	^{40}**K** **(mBq/Pmt)**
χ^2 **method**	0.6±0.08	0.46±0.08	0.09±0.03	3.9±0.4
γ**-lines**	0.3±0.1	0.4±0.2	<0.18	5.5±0.6

Table 6.4: Activities obtained for the QUPID sample via the χ^2 analysis and comparison to the γ-line analysis [62]

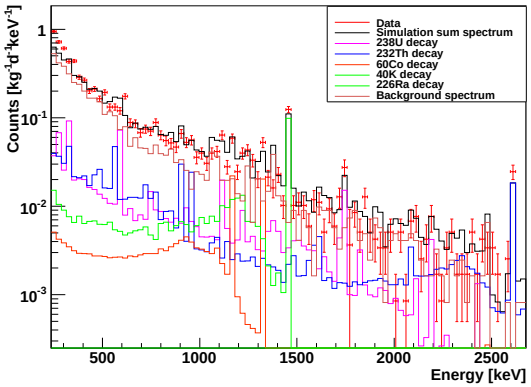

Figure 6.6: Fit of the simulations to the QUPIDs data.

The QUPID entirely made of ultraclean synthetic silica (quartz). Thus 1.19 kg of quartz sample was also screened separately for 12.3 days in Gator. Fit spectra of quartz can be seen in figure 6.7. Results from this screening represented in table 6.6. Activity of ^{40}K is significantly higher than the other isotopes within the this material. This proves the origin of the ^{40}K contamination within the QUPIDs. Therefore a decrease in the activity of ^{40}K in the quartz will significantly decrease the activity of this isotope in the QUPIDs

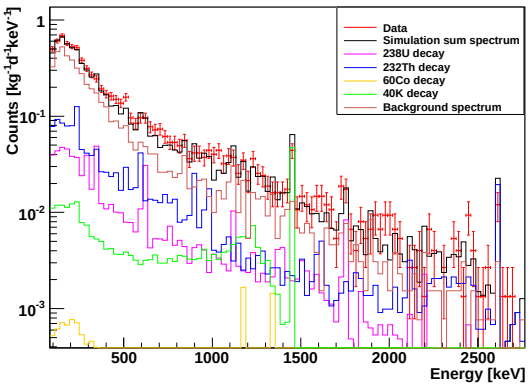

Figure 6.7: Fit of the simulations to the data from the quartz screening.

Method	^{238}**U** (**mBq/kg**)	^{232}**Th** (**mBq/kg**)	^{60}**Co** (**mBq/kg**)	^{40}**K** (**mBq/kg**)
χ^2 **method**	< 0.6	< 1.9	< 0.1	20 ± 7

Table 6.6: Activities obtained for quartz sample via the χ^2 analysis

Isotope/chain	**QUPID**	**R11410-MOD**	**R8520**
^{238}**U (mBq/cm^2)**	0.007± 0.001	< 0.3	<0.2
^{232}**Th (mBq/cm^2)**	0.005 ± 0.001	< 0.03	0.03 ± 0.01
^{60}**Co (mBq/cm^2)**	0.001± 0.0003	0.1 ± 0.009	0.1 ± 0.006
^{40}**K (mBq/cm^2)**	0.04± 0.004	0.3 ± 0.1	1.3 ± 0.13

Table 6.7: Comparison of Gator screening results for QUPID, Hamamatsu R11410-MOD and R8520. Activity values are normalized to photocathode area.

High quantum efficiency, high gain (>10^5), good timing performace with a pulse width <10 ns, good collection efficiency and large dynamic range are the advantages of this PMT. In addition to these advantages, as it was shown in table 6.7, QUPID has a very low intrinsic radioactivity compared to other PMTs. Therefore, QUPID could be a suitable alternative for the next generation experiments.

6.2 R8520-06-AL PMT Parts

PMTs are made from different types of materials and some of them have a composite structure, thus it is very important to know the activities of each individual PMT parts and give a report to Hamamatsu. Therefore PMT parts which are dominant on the total PMT activity can be determined. Either a different material can be used or the processes in the material production can be changed. All pmt components used in the construction of R8520-06-AL were provided by Hamamatsu. These samples were screened in Gator. Figure 6.8 shows a schematic structure of the R8520-06-AL PMTs along with the label of the parts. First column of table 6.8 shows the name of each part. Second column shows the type of the material. Third column gives the mass of screened part and the last column gives the time of screening. Table 6.10 was provided by Hamamatsu and shows mechanical sample and mass model for this PMT.

All these samples listed in table 6.8 are placed on top of detectors endcap for screening and the simulations were fitted to the data to obtain the scaling factors for the activity determination. Figure 6.9 shows the fit spectra obtained for the sample A (top left), sample B (top right), sample C (middle left), sample D (middle right), sample E (bottom left) and sample F (bottom right). Figure 6.10 shows the fit spectra obtained for the sample H (top left), sample I (top right), sample J (middle left), sample K (middle right), sample L (bottom left) and sample M (bottom right).

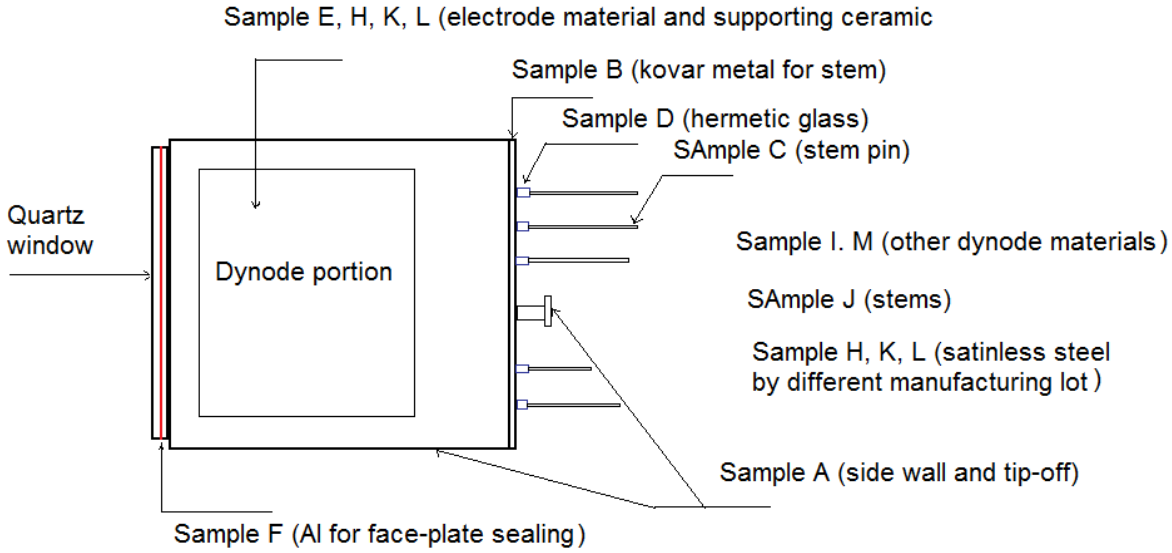

Figure 6.8: schematic structure of the R8520-06-AL PMTs along with the label of the parts.

PMT part	Material	Mass (g)	Time of screening (days)
Sample A	Kovar Metal, main metal package, not used in stem	216	4.8
Sample B	Kovar Metal, used in the stem	234.9	10.4
Sample C	Kovar Metal, used in the stem pin	211	11.5
Sample D	Kovar Glass, used in the stem	195	5
Sample E	Ceramic, spacer between electrodes	218.9	5.5
Sample F	Aluminum, sealing between quartz window and metal package	209	10.1
Sample H	Stainless Steel, electrodes for R8520-06-AL	121.1	11.9
Sample I	Alloy, electrodes for Flat Panel PMT's	128.8	10
Sample J	Kovar Metal and Glass, stem	167	8.6
Sample K	Stainless Steel, electrodes used for ZA2628 to LV0030	303.4	8.55
Sample L	Stainless Steel, electrodes used for LV0069 to current	296.7	10.5
Sample M	Stainless Steel, Electrodes	318.2	9

Table 6.8: List of the screened PMT parts along with the mass of the sample and live time of screening.

These specta reveals that the sample A and sample B are mainly dominated by ^{60}Co. In sample C dominating contamination arise from the decays of ^{238}U and ^{60}Co. Among the other samples the highly contamined are the Sample D and sample E. For both

Parts Name	**Material**	**Weight [g]**	**Component**
Glass for window	Synthetic silica	2	SiO_2 (100%)
Glass in stem	Kovar glass	1	SiO_2 (67.0%) Al_2O_3 (4.3%) B_2O_3 (18.0%) Li_2O (1.0%) Na_2O (6.0%) BaO (2.0%)
Metal package and stem pins	Kovar metal	13	Fe (55%) Ni (29%) Co (16%)
Electrodes	Stainless steel	7	Fe (70%) C (0.1%) Si (0.5%) Mn (0.7%) Ni (8.6%) Cr (18.3%)
Getter	ZrAl	0.02	Zr (84%) Al (16%)
Insulator	Ceramic	0.04	Al_2O_3 (96%)
Aluminum ring	Aluminum	0.1	Al (99.5%)

Table 6.10: Mass model for R8520-06-AL from Hamamatsu

of these samples, ^{238}U, ^{232}Th and ^{40}K are significantly higher than all other samples. This is most probably due to the composite structures of these samples. A very high contamination of ^{232}Th is clearly visible in the Sample F.

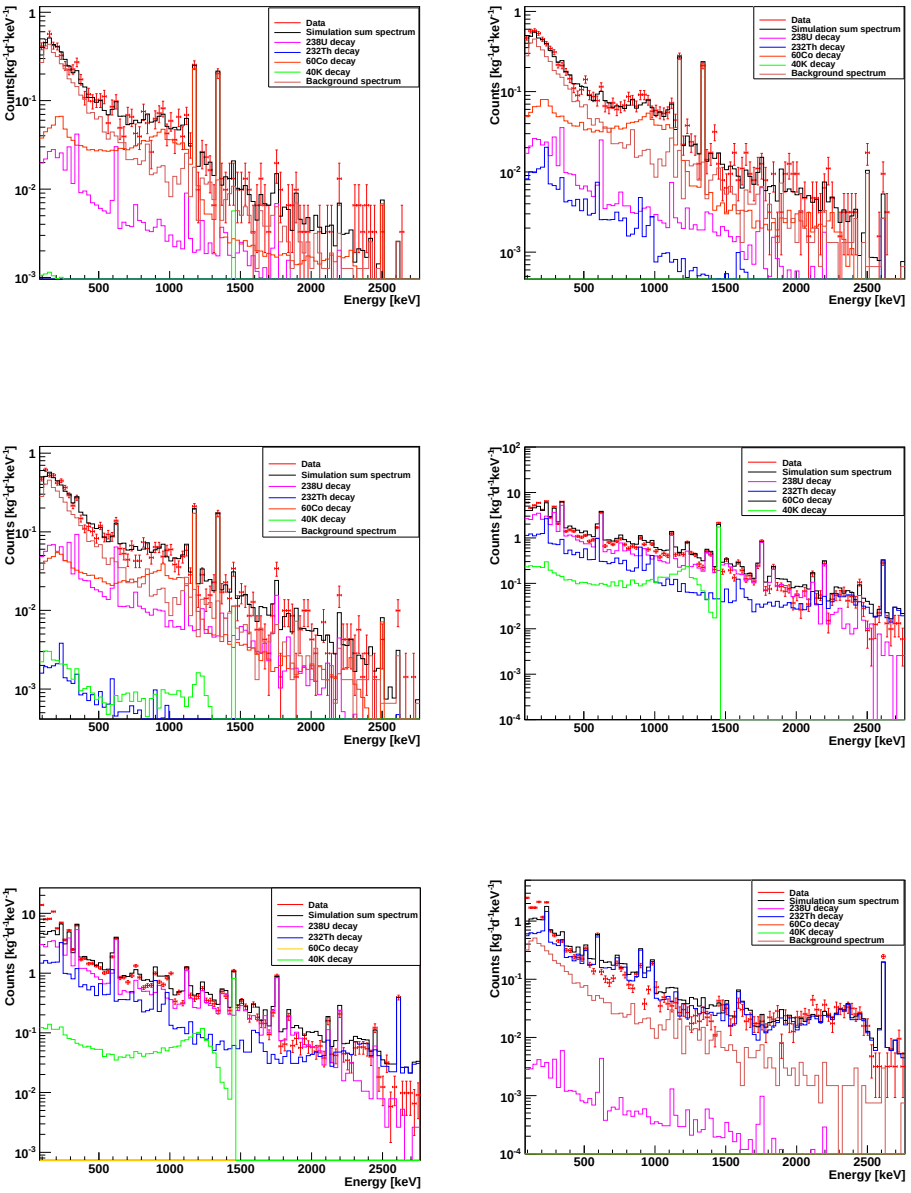

Figure 6.9: Fit spectra obtained for the sample A (top left), sample B (top right), sample C (middle left), sample D (middle right), sample E (bottom left) and sample F (bottom right).

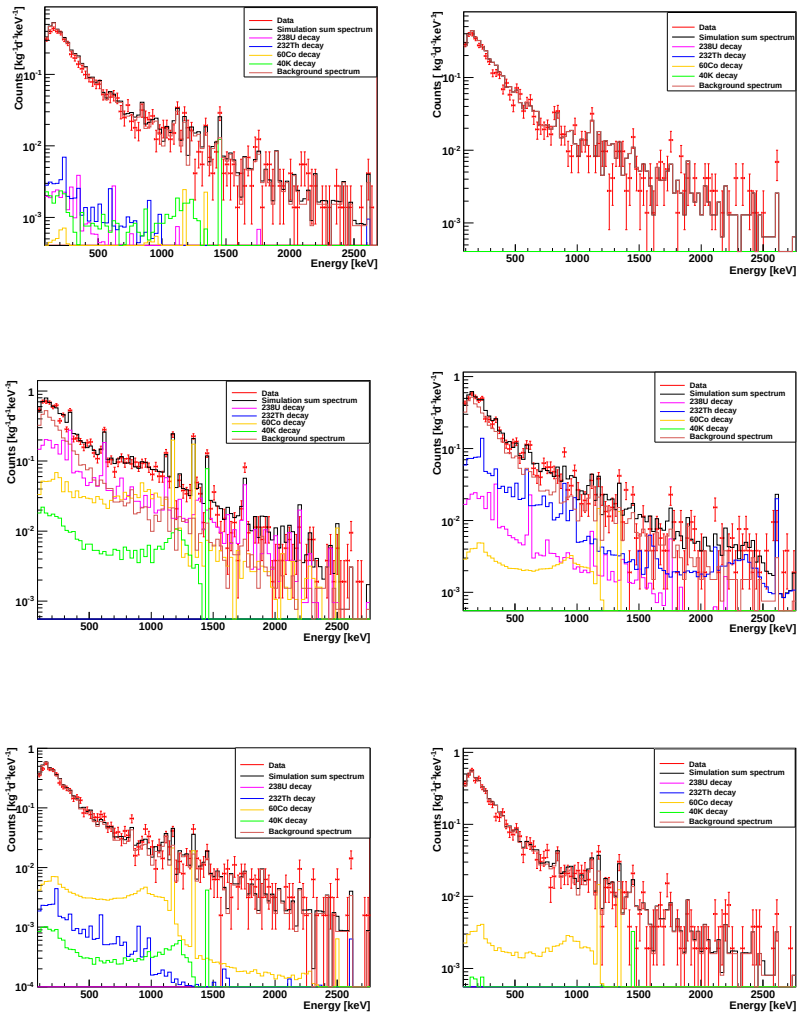

Figure 6.10: Fit spectra obtained for the sample H (top left), sample I (top right), sample J (middle left), sample K (middle right), sample L (bottom left) and sample M (bottom right).

Activity results calculated for all these samples are shown in table 6.11. According to the results given in this table and by taking into account the mass model of a single PMT (table 6.10), the main components responsible for the overall PMT radioactivity were determined. The results indicate that the largest contribution to the activity of a single PMT arises from the main metal package (Sample A), from the borosilicate glass (sample D), from the aluminum (Sample F) and from the electrodes (sample H). These results were also shown as piecharts in figure 6.11.

According to the mass model (table 6.10) the expected activity for a single PMT

Material	^{238}**U** (mBq/kg)	^{232}**Th** (mBq/kg)	^{60}**Co** (mBq/kg)	^{40}**K** (mBq/kg)
Sample A	19.0±7.0	< 14	42.2±5.3	< 90
Sample B	< 11.7	< 8.0	33.3±2.2	<75.4
Sample C	12.2±2.2	< 5.2	17.3±1.5	< 45.4
Sample D	973.0±19.0	343.5±16.3	< 0.56	2310±175
Sample E	776±17	256±20	< 12	903±93
Sample F	17.3±6.8	367±25	<0.3	5.2±1.1
Sample H	18.6±6.5	17.9±7.9	12.3±4.6	149±20
Sample I	< 0.3	< 0.3	< 0.5	< 14.8
Sample J	40±3	< 0.6	22.2±2.2	80±3
Sample K	< 10	13±3	< 6	< 24
Sample L	< 5.9	<5.2	< 5.5	< 58
Sample M	< 0.4	< 0.2	< 7	< 86

Table 6.11: Activities calculated for the single R8520 PMT parts.

calculated and the results shown in table 6.12 (first row). Second row shows the average activity of screened PMTs. The predicted activity for ^{238}U and ^{232}Th is higher than the measured activity of PMTs. ^{60}Co activity is in agreement but with the measured value but ^{40}K is lower than the measured value. Since the PMT parts are not from the batches used in the XENON100, the results found in this study are still acceptable.

	^{238}**U** (mBq/Pmt)	^{232}**Th** (mBq/Pmt)	^{60}**Co** (mBq/Pmt)	^{40}**K** (mBq/Pmt)
Expected activity	1.4±0.2	0.55±0.08	0.63±0.1	3.42±0.33
Average PMT activity	0.26±0.07	0.24±0.09	0.65±0.09	12.1±1.2

Table 6.12: Expected activity of a single PMT from the screening of individual PMT parts (first row) and comparison to the measured PMT activity (second row)

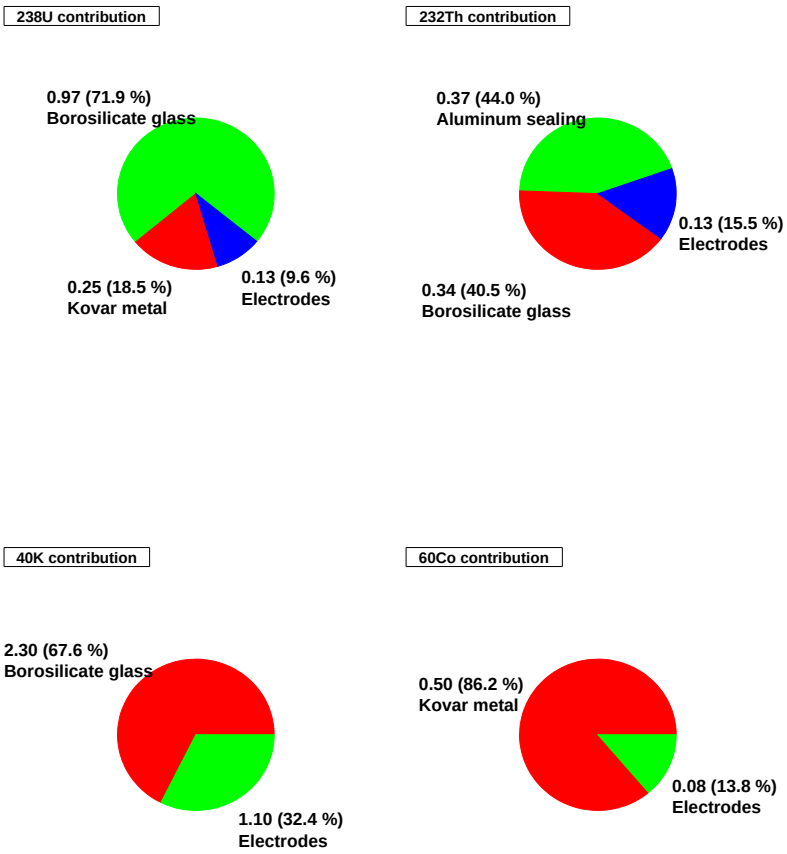

Figure 6.11: Contribution of each PMT part to the overall ^{238}U , ^{232}Th ,^{40}K and ^{60}Co activity of one PMT. The numbers are in units of mBq/PMT, and the numbers in brackets give the percentage of the corresponding material to the total activity (in U, Th, K or Co) of one PMT. The samples with negligible contributions are not shown here.

6.3 Metal Samples

Different type of sheet formed raw metal samples, such as stainless steel and copper, used to construct grid frames and shield of XENON100, respectively. Tianium sample was also screened as a candidate cryostat material for XENON1T. Additionally, we also examined metals, such as screws, with Gator to obtain the activities of those samples.

6.3.1 Stainless Steel

A stainless steel sample bought from Nironit Edelstahlhandel GmbH [79] was screened for 6.76 days. The weight of the sample is 6.6 kg and thus it was placed around the detector within the sample cavity. This sample was used to construct the grid frames of the XENON100. During its ground based transportation to LNGS the sample was activated by cosmic radiation and peaks around 810 keV due to the decay of ^{58}Co and around 840 keV due to the decay of ^{54}Mn are visible. Thus, these cosmogenics were also simulated for this sample and activities calculated as well. Figure 6.12 shows the obtained fit spectrum and table 6.14 shows the calculated results from χ^2 minimization analysis and comparison to the results from γ-line analysis [62].

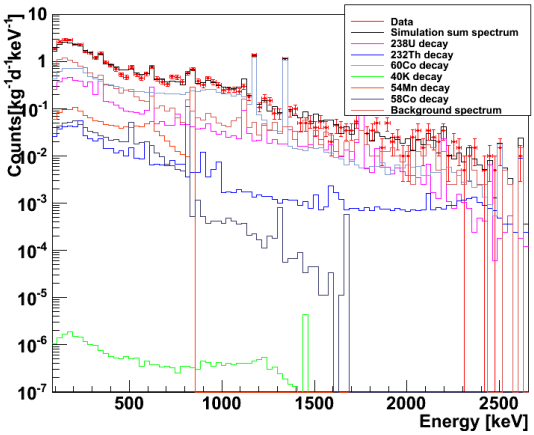

Figure 6.12: Fit of the simulations to the data from the stainless steel screening.

Method	^{238}**U** (mBq/kg)	^{232}**Th** (mBq/kg)	^{60}**Co** (mBq/kg)	^{40}**K** (mBq/kg)	^{54}**Mn** (mBq/kg)	^{58}**Co** (mBq/kg)
χ^2 **method**	4.1±0.6	1.35±0.36	7.4±1.1	<4.6	1.36±0.24	0.44±0.024
γ**-lines**	4.3±0.9	1.8± 0.5	7.2±0.9	<5.7	1.7±0.20	0.5±0.20

Table 6.14: Stainless steel activities obtained with the χ^2 analysis and comparison to the results from γ-line analysis [62]

For XENON100, several other stainless steel samples bought from Nironit Edelstahlhandel GmbH [79] with different sheet thicknesses were screened in the LNGS screening facility and all the results were published in [75]. The results found for ^{238}U

and ^{232}Th in the activity analysis of these stainless steel samples for XENON100 are in agreement with the results obtained for the radioactivity levels of stainless steel used for the cryostat of the Gerda experiment [80]. Radioactivity value for ^{60}Co is less than the values shown in [80] and for now it is the lowest value which has ever been reported.

6.3.2 Screws

0.27 kg of screw samples bought from McMaster [81] were placed on the Gator's endcap and screened for 12.1 days. Those screws were used to fix the PMT bases on the teflon structure above the target volume. Figure 6.13 shows the obtained fit spectrum while table 6.16 shows the calculated results from χ^2 minimization analysis and comparison to the results from γ-line analysis [62].

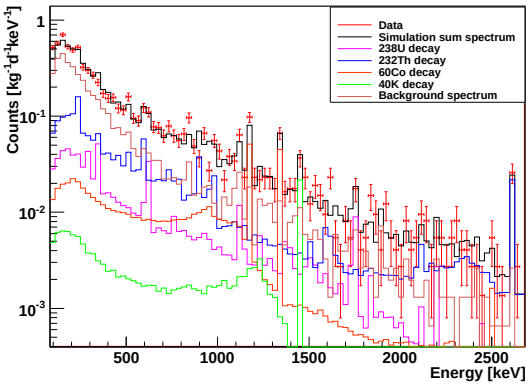

Figure 6.13: Fit of the simulations to the screw data from screening.

Method	^{238}**U** (mBq/kg)	^{232}**Th** (mBq/kg)	^{60}**Co** (mBq/kg)	^{40}**K** (mBq/kg)
χ^2 **method**	6.7±3	13.2±2.8	6.0±1.4	<57
γ**-lines**	<7	11.4± 4	6.0±2	<46.4

Table 6.16: Screw activities obtained with the χ^2 analysis and comparison to the results from γ-line analysis [62]

6.3.3 Copper

Oxygen-free high conductivity copper (OFHC) is one of the cleanest material in terms of its radioactive contamination. Therefore this material is used mainly either for the inner part or the shield of the detectors searching for the rare events. Sheet formed copper sample bought from Norddeutsche affinerie [57] and used to hold PMTs was screened for 20.3 days. This sample is used to construct the TPC of XENON100. The weight of the sample is 18.1 kg and thus placed around the detector within the sample cavity. Figure 6.14 (left) compares the data spectrum from the copper screening to the background spectrum. This spectrum shows that the background spectrum of Gator is higher than the data spectrum up to 300 keV. This might due to a shielding effect of the copper sample. The most distinguishable lines above the background are the lines from the decay of cosmogenic ^{58}Co, ^{54}Mn and ^{60}Co. This sample was stored several months above ground and activated by cosmic rays. Figure 6.14 (right) shows the obtained fit spectrum while table 6.18 represents the calculated results from χ^2 minimization analysis and comparison to the results from γ-line analysis [62].

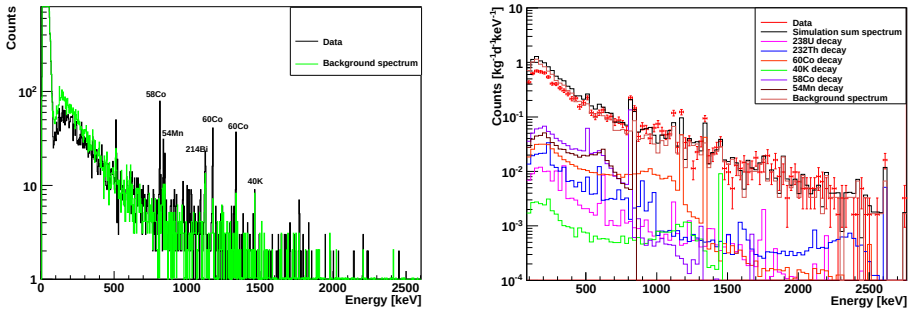

Figure 6.14: Comparison of data spectrum taken from copper measurement to the background spectrum of Gator (left). Fit of the simulations to the copper data(right)

Method	^{238}**U** (mBq/kg)	^{232}**Th** (mBq/kg)	^{60}**Co** (mBq/kg)	^{40}**K** (mBq/kg)	^{54}**Mn** (mBq/kg)	^{58}**Co** (mBq/kg)
χ^2 **method**	<0.69	<0.62	0.24±0.07	<1.1	<0.11	0.27±0.04
γ**-lines**	<0.22	<0.16	0.20±0.08	<1.3	–	–

Table 6.18: Copper activities obtained with the χ^2 analysis and comparison to the results from γ-line analysis [62]

Analysis made for this sample shows that the ^{238}U, ^{232}Th and ^{40}K contaminations are below the sensitivity of Gator and sample. ^{58}Co and ^{54}Mn has a half life less than a year and one year of underground deposition of this sample will significantly reduce the activity of these nuclides. Activity of ^{60}Co is higher but this sample is still a suitable material for the detector construction.

6.3.4 Titanium

Steel is the material which has been widely used in the large scale physics experiments because of its high tensile strength and relatively low costs. In case radioactivity is crucial, copper can be used as an alternative of steel. However, up to now, titanium was not used in any dark matter experiment. Advantages of titanium compared to copper are: the high tensile strength, lower cost and it can be welded. The latter property of titanium is important because of brazing for copper creates micro holes and makes it possible radon diffuse into experiment.

A sheet formed Titanium sample bought from Nironit Edelstahlhandel GmbH [79] was screened for 27.6 days. The weight of the sample is 10.5 kg and thus placed around the detector. Figure 6.15 (left) compares the data spectrum from the titanium screening to the background spectrum. In the data spectrum, the origin of 2 strong peaks located at 889.3 keV and 1120.5 keV was investigated. The result showed that those peaks are arising from the decay of ^{46}Sc which can be produced via cosmogenic activation of titanium. The half life of the 46Sc is only 83.7 days [85] and 1 year of underground deposition of the Titanium will reduce these lines below the background level. The decay of the ^{46}Sc was simulated for this sample as well and simulations were fitted to the data. Figure 6.15 (right) shows the obtained fit spectrum and table 6.20 represents the calculated results from χ^2 minimization analysis.

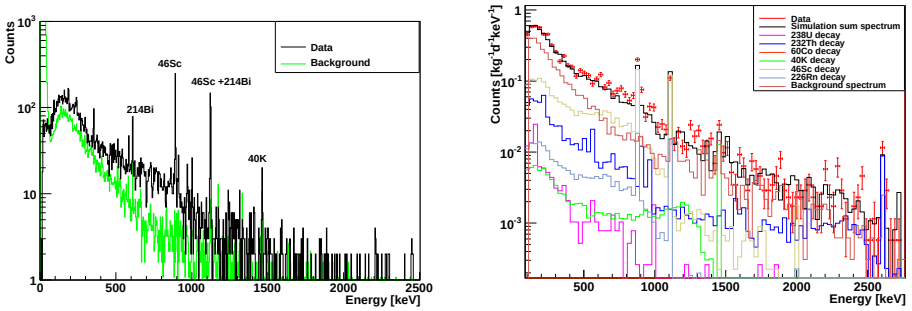

Figure 6.15: Comparison of data spectrum taken from titanium measurement to the background spectrum of Gator (left). Fit of the simulations to the titanium data (right)

Method	^{238}**U** (mBq/kg)	^{226}**Ra** (mBq/kg)	^{232}**Th** (mBq/kg)	^{60}**Co** (mBq/kg)	^{40}**K** (mBq/kg)	^{46}**Sc** (mBq/kg)
χ^2 **method**	< 6.5	< 0.35	0.53±0.09	< 0.24	< 3.0	1.54±0.06

Table 6.20: Activities obtained for titanium sample via the χ^2 analysis

LUX collaboration screened 7 different Ti samples [82]. Their results ranges between < 2.5 and 15 ± 3.8 mBq/kg for ^{238}U, between <0.2 and 8.1± 1.2 mBq/kg for ^{232}Th and between <0.93 and <9.3 mBq/kg for ^{40}K. They did not give any results on ^{60}Co. The results from LUX are consistent with our results. Compared to stainless steel, Ti has less radioactive contamination and it could be used to construct the parts of detectors where high tensile strength and low contamination is needed.

6.4 Plastic Samples

Two different plastic samples were measured with Gator with different amount of sample mass and different measurement times. We measured polyethylene used in the shield of the XENON100 detector as a neutron moderator and PTFE samples used to build the TPC of XENON100. The results obtained are summarized in this section.

6.4.1 Polyethylene from the shield of XENON100

Polyethylene is a common material used in the shield of the rare event experiments to moderate neutrons. Polyethylene was bought from in2plastics [86] and is used in the shield wall and the shield door of XENON100 detector was screened for 5.85 and 3.1 days, respectively. The weight of the samples are: 2.7 kg from the wall and 3.1 kg from the door. The samples were distributed around the Gator. Figure 6.16 (left) shows the obtained fit spectrum for the sample from the wall and right plot shows the fit spectrum for the sample from the door. Table 6.21 shows the calculated results from χ^2 minimization analysis for both samples and compares the results from γ-line analysis [62].

Because of low sample mass and short data taking with Gator, only upper limits can be provided for both samples. 8.44 kg of polyethylene sample from the wall and door of XENON100 was also screened together for 28.9 days in the LNGS facility and activities for ^{238}U (0.23 ± 0.05 mBq/kg) and ^{40}K (0.7±0.04 mBq/kg) are provided [75]. Depending on these results, 5 cm thick OFHC copper was used in the innermost shield layer of XENON100 to block the gammas coming from the polyethylene layer.

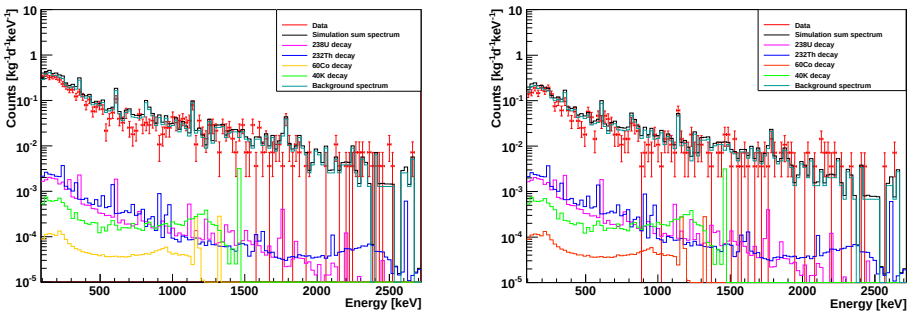

Figure 6.16: Fit of the simulations to the polyethylene data from the shield wall of XENON100 (left) and from the shield door of XENON100 (right).

Material	**Method**	^{238}**U (mBq/kg)**	^{232}**Th (mBq/kg)**	^{60}**Co (mBq/kg)**	^{40}**K (mBq/kg)**
Poly wall	χ^2 method	<0.91	<0.62	<0.64	<2.2
	γ-lines	<3.54	<2.69	<0.89	<5.88
Poly door	χ^2 method	<2.5	<1.9	<1.9	<7
	γ-lines	<6.5	<5.7	<1.7	<12.7

Table 6.21: Activities calculated via 2 different analysis methods for both polyethylene samples taken from the shield of the XENON100.

6.4.2 PTFE sample

Polytetrafluoroethylene (PTFE, Teflon) is another commonly used material for detector construction. Its thermal properties allow this material to use at the liquid xenon temperatures (- 95 ^{o}C). It is a very good insulator and it is a very good UV light reflector at the xenon scintillation wavelength (λ=178 nm) [41]. Because of these properties, Teflon is used to build the TPC of XENON100.

13.5 kg of PTFE sample bought from Maagtechnic [87] was screened for 14.3 days. Another 23.5 Kg sample from the same company was screened seperately for 47.4 days. Figure 6.17 left shows the fit spectrum from 13.5 kg PTFE screening. Right plot shows the fit spectrum from 23.5 kg PTFE screening. Table 6.22 shows the calculated activities from χ^2 minimization analysis and compares the results to the γ-line analysis [62].

As summarized in table 6.22, only upper limits can be provided for the measured radionuclides and the results are convincing about the radiopurity of the sample. In case of PTFE, α particles coming from the decay chain of ^{238}U and ^{232}Th are also important. The molecular structure of PTFE (C_2F_4) includes fluorine ^{19}F which has

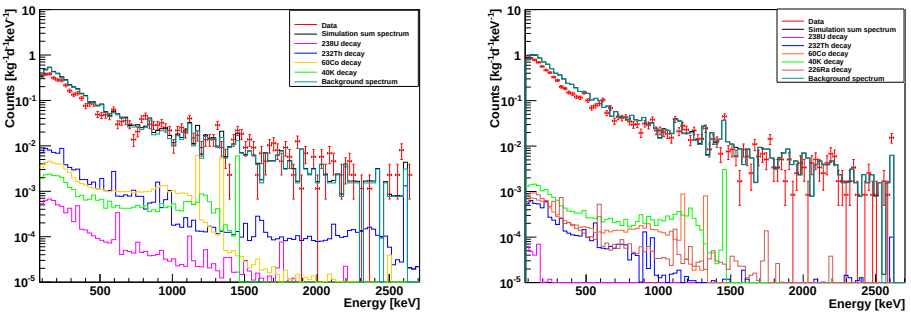

Figure 6.17: Fit of the simulations to the data from 13.5 kg PTFE screening (left) and from 23.5 kg PTFE screening (right).

Material	**Method**	^{238}**U (mBq/kg)**	^{232}**Th (mBq/kg)**	^{60}**Co (mBq/kg)**	^{40}**K (mBq/kg)**
PTFE (13.5 kg)	χ^2 method	<0.14	<0.16	<0.2	<4.5
	γ-lines	<0.31	<0.16	<0.1	<2.25
PTFE (23.5 kg)	χ^2 method	< 0.03	< 0.035	< 0.03	<0. 61
	γ-lines	< 0.06	< 0.10	< 0.03	< 0.75

Table 6.22: Activities calculated via 2 different analysis methods for the PTFE samples.

low atomic number and has a high cross section for (α, n) reactions ($\sim$ 200mb for E_α=5.5 MeV [83]). Measurements performed with Gator (table 6.22) shows that intrinsic contaminations for ^{238}U and ^{232}Th are <0.3 mBq/kg. In addition to these measurements, a 0.23 kg PTFE sample (used in TPC of XENON100) from McMaster [81] and a 6.2 kg PTFE from APT (not used in XENON100) were screened in LNGS screening facility. A third sample (used as veto reflector) from McMaster with very small mass (5.1 g) was measured with Inductively Coupled Plasma-Mass Spectrometry (ICP-MS). All three measurements yield that contaminations are <2 mBq/kg [75].

6.5 Environmental Samples

In addition to the materials used for the detector and shield construction, environmental materials also includes radioactivity. The knowledge of the activity from the environment allow us to determine the the expected neutron flux from (α , n) and spontaneous fission reactions in the material.

Concrete sample taken from the wall and the floor around the XENON100 location

at the LNGS were screened for 0.71 days and 0.22 days, respectively. The weight of the samples are 0.035 kg (from the wall) and 0.033 kg (from the floor). Both samples were placed on top of the detector endcap. Figure 6.18 (left) compares the data spectrum to the background spectrum and right plot shows the obtained fit spectrum for the concrete sample taken from the wall. Figure 6.19 shows the same plots for the concrete sample from the floor. Both samples have very small weight (only around 35 gr) and the both spectra from the screening are significantly higher than background of Gator. The results from the both measurements are given in table 6.23.

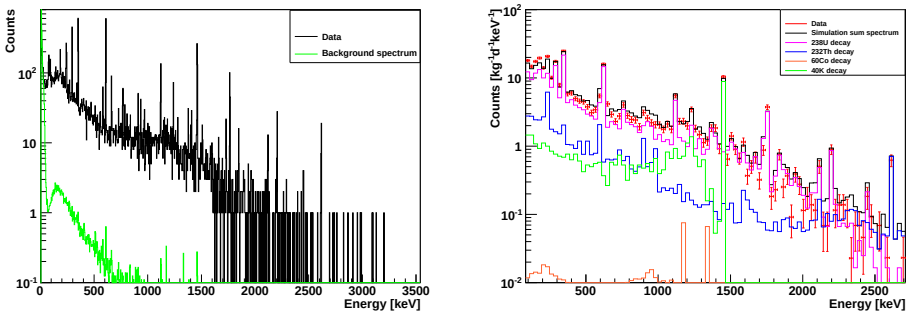

Figure 6.18: Comparison of data spectrum taken from the concrete measurement to the background spectrum of Gator (left). Fit of the simulations to the concrete data from the wall (right).

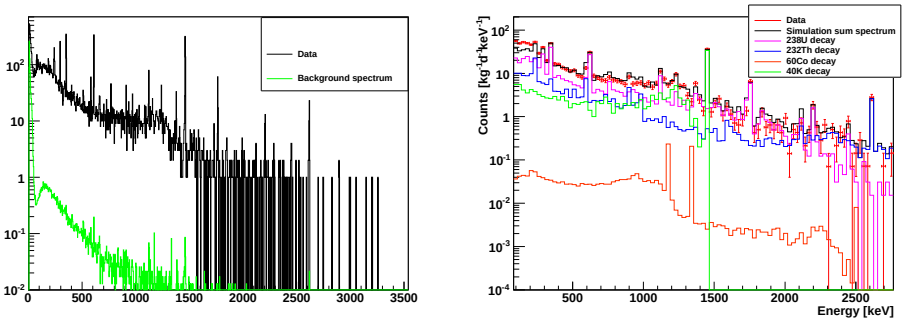

Figure 6.19: Comparison of data spectrum taken from the concrete measurement to the background spectrum of Gator (left). Fit of the simulations to the concrete data from the floor (right)

Activities of the primordial radionuclides in the underground laboratory was measured by using 3" NaI(Tl) detector. Results from this study are in agreement with the Gator results [88].

Material	**Method**	^{238}**U (mBq/kg)**	^{232}**Th (mBq/kg)**	^{60}**Co (mBq/kg)**	^{40}**K (mBq/kg)**
Concrete (wall)	χ^2 method	16.6±1.9	3.1±0.65	<0.6	53.1±3.6
	γ-lines	15.0±2.4	3.8±0.8	<0.7	42.0±6
Concrete (floor)	χ^2 method	32.7±2.5	12.1±2.1	<0.47	183±12
	γ-lines	26.0±5.0	8.0±2.0	<0.58	170.0±30.0

Table 6.23: Concrete activities obtained with the χ^2 analysis and comparison to the results from γ-line analysis [62].

Chapter 7

Summary and Outlook

The Gator detector was operated within the SOLO facility between 2005 and 2007 at the Soudan underground mine to screen the materials for the XENON10 phase [67]. In the XENON100 phase [40], it was aimed to increase the sensitivity of the experiment by increasing the detector mass and at the same time further decreasing the background by a factor of 100 by careful selection of the materials.

In order to screen the materials and to select the radiopure ones for the detector and the shield, the Gator screening facility [61] was moved to LNGS in summer 2007. A 2.2 kg p-type high purity Germanium crystal is the core of the facility. The detector is placed in an ultra-low background passive shield which consists of a 20cm thick lead layer and a 5 cm thick copper layer. The sample cavity of Gator is designed such as big and massive samples can be accommodated easily. The entire system is enclosed in an air-tight aluminum box and continuously purged by nitrogen gas against radon diffusion. As a result of a better shield design and improved radon protection system, the integral count rate of Gator decreased from (0.842±0.005) counts/min at Soudan to (0.157±0.001) counts/min at LNGS between 100 keV and 2700 keV. A slow control which remotely monitors all crucial detector parameters which are important for a long term stable detector operation and the data acquisition was developed and implemented into the facility.

The entire detector and the shield geometry of Gator facility has been coded into Geant4. The Geant4 simulations are required to obtain the efficiencies to determine activities of the screened samples and to study the background of the facility. Background runs were taken in 2007, 2008 and 2010 and the background of the facility was modeled with Monte Carlo simulations. The background analysis shows that the main contribution to the background arises from the decays of ^{238}U, ^{232}Th, ^{40}K within the copper of the cryostat and the shield and from ^{210}Pb decays within the innermost lead layers. The background of the Gator facility is comparable to the background of the world's most sensitive germanium detector located at the LNGS screening facility (GeMPI) [18].

The efficiency determination of Gator was cross-checked by using 2 extended sources and their certified values. A good agreement within the uncertainties between the certified values and Gator measurements was obtained. In addition to a standard data analysis method (analysis of the most prominent lines) an alternative method which relies on the fit of simulated spectra to the experimental data by minimizing the χ^2 value between the simulations and the data was implemented and tested. The results obtained by the 2 different analysis methods are in a good agreement within errors.

Not only the different type of detector and shield construction materials (PMTs, metal samples, plastic samples and environmental samples) but also individual PMT components were screened with Gator. The results from the individual PMT components helped to understand which parts of the PMTs have the higher activity and thus need to be improved to further decrease their radioactivity. For the screening of the samples [75], Gator and the LNGS screening facility [18] was used. Activity results obtained from the screening measurements have been used to estimate the electromagnetic background of XENON100 [84]. Figure 7.1 shows the energy spectra of the background from measured data and Monte Carlo simulations in the 30 kg fiducial volume without veto cut (thick red solid line). The measured energy spectrum of XENON100 was compared to the detailed Monte Carlo analysis. It was seen that the background design goal of $<10^{-2}$ events$\cdot$ keV$^{-1}\cdot$day^{-1} was achieved and currently XENON100 has the lowest electromagnetic background of all running dark matter experiments.

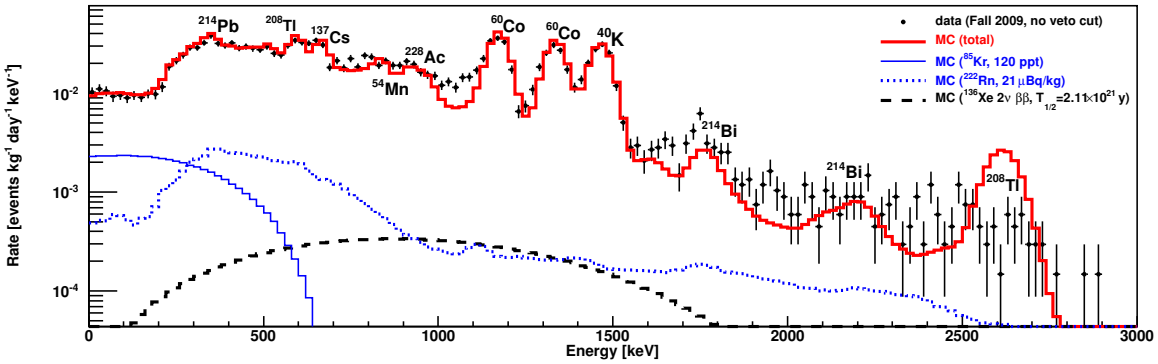

Figure 7.1: Energy spectra of the background from measured data and Monte Carlo simulations in the 30 kg fiducial volume without veto cut (thick red solid line) [84].

The Gator facility is now operated under stable conditions at LNGS to screen materials for the construction of the XENON1T experiment, for the next phase of the GERDA project and for a future noble liquid dark matter search facility, DARWIN.

Bibliography

[1] F. Zwicky, Helv. Phys. Acta 6 (1933) 110-127.

[2] C. Grupen, *Astroparticle Physics*, Springer Verlag Berlin Heidelberg, 2005.

[3] E. Hubble, Proc. Nat. Acad. Sci. (15) (1929) 168.

[4] A. A. Penzias, R. W. Wilson, Ap. J. 142 (1965) 419-421.

[5] K. A. Olive, Preprint astro-ph / 9707212 (1997).

[6] M. Rowan-Robinson, *Cosmology*, Oxford University Press, Oxford,3. Edition, 1993.

[7] D. N. Spergel et al., Ap. J. S. 148 (2003) 175.

[8] R. A. Knop et al., Ap. J. 598 (2003) 102-137.

[9] M Fukugita, C.J. Hogan, P.J.E. Peebles, Ap.J. 503, (1998) 518 - 530.

[10] J. Garcia-Bellido, Phil. Trans. Roy. Soc. Lond. A 357, (1999) 3237-3257.

[11] R. Catena, P. Ullio, JCAP08 (2010) 004.

[12] M. J. Reid et al., ApJ 700 (2009) 137.

[13] G. Jungman, M. Kamionkowski, K. Griest, Phys.Rep. 267 (1996) 195-373.

[14] R. J. Gaitskell, Annu. Rev. Nucl. Part. Sci. 54: (2004) 315-59.

[15] Anne M. Green, JCAP0807:005, (2008).

[16] Joseph A. Formaggio and C.J. Martoff, Annu. Rev. Nucl. Part. Sci. 54: (2004) 361-412.

[17] G. Heusser, T. Kirsten, Nucl. Phys. A 195 (1972) 369-378.

[18] H. Neder, G. Heusser and M. Laubenstein Appl. Rad. Isot., 53 (2000) 191.

[19] G. Heusser, M. Laubenstein, H. Neder Proc. of Intern. Conf. Isotop. Environm. Studies Aquatic Forum (2004).

[20] L.Anchordoqui et.Al., Int.J.Mod.Phys.A18: (2003) 2229-2366

[21] P.P. Povinec, J.-F. Comanducci, I. Levy-Palomo, Appl. Rad. and Isot. 61 (2004) 85-93.

[22] M. Schwaiger, F. Steger, T. Schroettner, C. Schmitzer, Appl. Rad. and Isot. 56 (2002) 375-378.

[23] M. Kohler et al., Appl. Rad. and Isot. 67 (2009) 736-740

[24] Luiz de Viveiros, *Optimization of Signal versus Background in Liquid Xe Detectors Used for Dark Matter Direct Detection Experiments*. Ph.D Thesis, Brown University 2010.

[25] V.E. Guiseppe, (Majorana Collaboration), IEEE Nucl. Sci. Symp. Conf. Rec. 2008:1793-1798.

[26] Z. Ahmed, et al., (CDMS Collaboration), Phys. Rev. Lett. 102, (2009) 011301.

[27] J. Angle et al., (XENON10 Collaboration), Phys. Rev. Lett. 100, (2008) 021303.

[28] S. Fiorucci et al., (LUX Collaboration), arXiv:0912.0482v1.

[29] J. Angle et al. (XENON10 Collaboration), Phys. Rev. Lett. 101, (2008) 091301.

[30] E. Aprile et al. (XENON10 Collaboration), Phys. Rev. Lett. 105, (2010) 131302.

[31] E. Aprile et al. (XENON100 Collaboration), Phys. Rev. Lett. 107, (2011) 131302.

[32] E. Armengaud et al., (EDELWEISS) (2011), arXiv:1103.4070.

[33] Z. Ahmed et al., (CDMS collaboration), Science 327, (2010) 1619.

[34] Z. Ahmed et al., (CDMS collaboration), Phys. Rev. Lett. 106, (2011) 131302.

[35] J. Angle et al., (XENON10 collaboration) (2011), arXiv:1104.3088.

[36] O. Buchmueller et al., (2011), arXiv:1102.4585.

[37] R. Trotta et al., J. High Energy Phys. 12, (2008) 024.

[38] C. E. Aalseth et al., (CoGeNT), Phys. Rev. Lett. 106, (2011) 131301.

[39] C. Savage et al., JCAP 0904, 010 (2009).

[40] E. Aprile et al. (XENON100 Collaboration), arXiv:1107.2155v2.

[41] M. Yamashita et al., Nucl. Instr. Meth. A 535 (2004) 692.

[42] http://www.etap.physik.uni-mainz.de/495_DEU_HTML.php.

[43] M. Schumann, XENON-Results and Prospects, TPC 2010, Paris, December 15^{th} , 2010.

[44] K. Ni, *Development of a liquid Xenon Time Projection Chamber for the XENON Dark Matter Search*. PhD thesis, University of Columbia, 2006.

[45] M. Schumann, XENON100, XENON1T, DARWIN, CHIPP Plenary Meeting 2011, Leysin, September 1, 2011.

[46] Laura Baudis (DARWIN Consortium), arXiv:1012.4764v1.

[47] http://darwin.physik.uzh.ch/.

[48] M.Harańczyk et al., Acta Phys. Polon. B41, (2010) 1441-1446.

[49] R. Brunetti et al, New Astronomy Reviews 49, (2005) 265-269.

[50] J. Angle et al., Phys. Rev. Lett. 101, (2008) 091301.

[51] C. Grupen, B. Shwartz, *Particle Detectors 2nd edition*. Cambridge University Press 1996.

[52] G. Knoll, *Radiation detection and measurements 3rd edition*. John Wiley and Sons, Inc., New York 2000.

[53] http://nsspi-apps.ne.tamu.edu/NSEP/basic_rad_detection/index.php?.

[54] M. Tyagi *Introduction to Semiconductor Materials and Devices*. John Wiley&Sons, Inc. 1991.

[55] R. A. Kroeger, et al. Nucl. Instr. Meth. Phys. Res., A422(1-3) (1999) 206.

[56] Canberra, http://www.canberra.com/.

[57] Aurubis, http://www.aurubis.com/en/home/.

[58] Plombum, http://www.plombum.republika.pl/.

[59] G. Heusser, Annu. Rev. Nucl. Part. Sci. 1995. 45:543-90.

[60] M. G. Pia, Nuclear Physics B (Proc. Suppl.) 125 (2003) 60-68.

[61] L. Baudis et al., JINST 6 P08010 (2011).

[62] A. D. Ferella, University of Zurich, private communications.

[63] C. Hurtgen, S. Jerome, and M. Woods, Applied Radiation and Isotopes 53, 45 (2000), ISSN 0969-8043.

[64] http://wwwasdoc.web.cern.ch/wwwasdoc/minuit/minmain.html.

[65] M. Heisel, F. Kaether, and H. Simgen, Applied Radiation and Isotopes 67, 741 (2009), ISSN 0969-8043.

[66] http://particleastro.brown.edu/SOLO/.

[67] J. Angle, *Gamma background studies for the XENON experiment using a high purity germanium detector*. Ph.D. thesis, University of Florida, Florida (2008).

[68] Gary Steigman, arXiv:hep-ph/0309347v2.

[69] Gentaro Watanabe, Toshiki Maruyama, arXiv:1109.3511v1.

[70] http://www.downtheyellowcakeroad.org.

[71] S. Cebrián et al, Astroparticle Physics 33 (2010) 316-329.

[72] M. Laubenstein et al, Applied Radiation and Isotopes 61 (2004) 167-172.

[73] M. Laubenstein, G.Heusser, Applied Radiation and Isotopes 67 (2009) 750-754.

[74] Borexino Collaboration: G. Alimonti, et al., Nucl. Instr. Meth A 600 (2009) 568-593..

[75] E. Aprile et al., Astropart. Phys. 35:43-49, 2011 .

[76] http://www.hamamatsu-news.eu/issues/hamamatsu_news_02_2011/files/assets/seo/page20.html.

[77] A. Teymourian et al, Nucl. Instr. Meth. A 654 (2011) 184.

[78] M. Suyama, et al., Nucl. Instr. Meth. A 523 (2004) 147-157.

[79] Nironit, http://www.nironit.de.

[80] W. Maneschg et al., Nucl. Inst. Meth. A 593 (2008) 448.

[81] McMaster, http://www.mcmaster.com.

[82] D. S. Akerib et al, arXiv:1112.1376v2.

[83] E.B. Norman et al. Phys. Rev. C 30 (1984) 1339.

[84] E. Aprile et al., Phys. Rev. D 83 (2011) 082001.

[85] http://www.nucleide.org/DDEP_WG/Nuclides/Sc-46_tables.pdf.

[86] in2plastics, http://www.in2plastics.com.

[87] Maagtechnic, http://www.maagtechnic.ch.

[88] M. Hafke et al., Nucl. Instr. Meth. A 643 (2011) 36.